Measurement and analysis of flow in 3D preforms for aerospace composites

by

Andrew Lawrence Stewart

Thesis submitted to the
Faculty of Graduate and Postdoctoral Studies
In partial fulfillment of the requirements
For the M.A.Sc. degree in
Mechanical Engineering

Ottawa-Carleton Institute for Mechanical and Aerospace Engineering
Faculty of Engineering
University of Ottawa

©Andrew Lawrence Stewart, Ottawa, Canada, 2012

Abstract

Composite materials have become viable alternatives to traditional engineering materials for many different product categories. Liquid transfer moulding (LTM) processes, specifically resin transfer moulding (RTM), is a cost-effective manufacturing technique for creating high performance composite parts. These parts can be tailor-made to their specific application by optimizing the properties of the textile preform. Preforms which require little or no further assembly work and are close to the shape of the final part are critical to obtaining high quality parts while simultaneously reducing labour and costs associated with other composite manufacturing techniques. One type of fabric which is well suited for near-net-shape preforms is stitched non-crimp fabrics. These fabrics offer very high in-plane strength and stiffness while also having increased resistance to delamination. Manufacturing parts from these dry preforms typically involves long-scale fluid flow through both open channels and porous fibre bundles.

This thesis documents and analyzes the flow of fluid through preforms manufactured from non-crimp fabrics featuring through-thickness stitches. The objective of this research is to determine the effect of this type of stitch on the RTM injection process. All of the tests used preforms with fibre volume fractions representative of primary and secondary structural parts. A series of trials was conducted using different fibre materials, flow rates, fibre volumes fractions, and degrees of fibre consolidation. All of the trials were conducted for cases similar to RTM. Consolidation of the fibres showed improvements to both the thoroughness of the filling and to the fibre volume fraction. Experimentally determined permeability data was shown to trend well with simple models and precision of the permeability data was comparable to values presented by other authors who studied fabrics which did not feature the through-thickness stitches.

Acknowledgements

I would like to express my sincere gratitude to Dr. François Robitaille for all of his insights and suggestions towards things not limited to solely the contents of this thesis. His support and patience, as well as good humour, made this time a definite highlight of my time spent at the University of Ottawa.

I would also like to thank my friends and colleagues Hesam Akbarnejad, for making the countless hours spent in Site rather enjoyable; and to Scott Audette and Aymen Sakka, for their aid and collaboration in the early days of this research.

Finally, I would like to deeply thank all of my family for inspiring me to pursue knowledge while also providing the opportunity and support to be able to follow through on these aspirations.

Contents

Abstract ii

Acknowledgements iii

List of Figures vi

List of Tables ix

Nomenclature x

1 Introduction 1
- 1.1 Composite materials . . . 1
- 1.2 Manufacturing processes and preforms . . . 6
  - 1.2.1 Manufacturing processes . . . 6
  - 1.2.2 Preforms . . . 10
- 1.3 Thesis overview . . . 16

2 Literature Review 17
- 2.1 Permeability . . . 17
- 2.2 Effects related to stitching . . . 28
- 2.3 Compaction effects . . . 31

3 Experimental setup and procedure 37
- 3.1 Experimental setup . . . 38
  - 3.1.1 Instruments common to all rigs . . . 38
  - 3.1.2 Instruments specific to each rig . . . 44
    - 3.1.2.1 Rig 1: Mould with aluminium base . . . 44
    - 3.1.2.2 Rig 2: Mould with polycarbonate base . . . 48
  - 3.1.3 Preform materials . . . 49

3.1.4 Fluids and dyes . . . 50
3.2 Procedure . . . 53
3.2.1 Experimental procedure . . . 53
3.2.2 Data analysis . . . 59
3.2.2.1 Preform data analysis . . . 59
3.2.2.2 Compaction related data analysis . . . 61
3.2.2.3 Video data analysis . . . 63
3.2.2.4 Isotropic case . . . 67
3.2.2.5 Orthotropic case . . . 67

4 Results **73**
4.1 Trial 01: Carbon fibre, 16 layers, 4.00 mm preform thickness, volumetric flow rate of 1.57 $\frac{cm^3}{s}$ . . . 79
4.2 Trial 02: Glass fibre, 5 layers, 4.00 mm preform thickness, volumetric flow rate of 1.00 $\frac{cm^3}{s}$ . . . 81
4.3 Trial 03: Glass fibre, 4 layers, 4.00 mm preform thickness, volumetric flow rate of 1.00 $\frac{cm^3}{s}$ . . . 85
4.4 Trial 04: Glass fibre, 4 layers, 4.00 mm preform thickness, volumetric flow rate of 1.00 $\frac{cm^3}{s}$ . . . 87
4.5 Trial 05: Glass fibre, 4 layers, 2.43 mm preform thickness, 35 compaction cycles, volumetric flow rate of 0.500 $\frac{cm^3}{s}$ . . . 89
4.6 Trial 06: Glass fibre, 6 layers, 4.00 mm preform thickness, 35 compaction cycles, volumetric flow rate of 0.250 $\frac{cm^3}{s}$ . . . 92
4.7 Trial 07: Glass fibre, 6 layers, 4.00 mm preform thickness, 35 compaction cycles, volumetric flow rate of 0.100 $\frac{cm^3}{s}$ . . . 95
4.8 Trial 08: Glass fibre, 7 layers, 4.00 mm preform thickness, 35 compaction cycles, volumetric flow rate of 0.100 $\frac{cm^3}{s}$ . . . 98
4.9 Trial 09: Glass fibre, 6 layers, 4.00 mm preform thickness, 35 compaction cycles, volumetric flow rate of 0.100 $\frac{cm^3}{s}$ . . . 103
4.10 Trial 10: Carbon fibre, 12 layers, 2.43 mm preform thickness, volumetric flow rate of 0.100 $\frac{cm^3}{s}$ . . . 106
4.11 Comparison of trials . . . 109

5 Conclusion and Recommendations **118**

Bibliography **120**

Appendicies **126**

List of Figures

1.1 Stiffness as a function of angle between fibre and loading axes 5
1.2 Typical RTM setup [13] 8
1.3 Typical VARTM setup [14] 9
1.4 Typical RFI setup [11] 10
1.5 Two types of preforms [15] 11
1.6 Crimp of fibres caused by weaving [16] 12
1.7 Sewing process 13
1.8 Common stitch types [17] 13
1.9 NCF preform composed of 6 layers of glass fibre 15

2.1 Different flow regimes 19
2.2 Different flow patterns derived from Darcy's law 20
2.3 Flow scenarios near injection port [25] 22
2.4 Permeability variation as a function of fibre volume fraction [21] 23
2.5 Measured permeability of a single fabric type [30] 23
2.6 Experimentally and theoretically derived Kozeny constants 26
2.7 Zones surrounding a stitch in NCF [41] 30
2.8 Representative fibre element [48] 33
2.9 Pressure as a function of fibre volume fraction with different variables 34
2.10 Effect of compaction on fibre reorganization for NCFs, 20x [51] 35
2.11 Effect of compaction on fibre reorganization for NCFs, 50x [51] 35

3.1 Diagram of the common elements 38
3.2 Brass cross with connections 41
3.3 Different pressure transducers used 42
3.4 Diagram of the mould with aluminium base 44
3.5 Aluminium base 45
3.6 Top view of the mould with spacing elements highlighted 46
3.7 Diagram of the 2D mould with polycarbonate base 48

3.8 Images of Trial 09 from both cameras, Rig 2 49
3.9 Pure silicone oil 51
3.10 Different dyes used 52
3.11 Experimental setup with Rig 1 53
3.12 Vacuum pump readout at steady state 56
3.13 Filling of the hydraulic cylinder 57
3.14 Pre-compaction preform area, Trial 08 60
3.15 v_f as a function of P_p, Trial 08 63
3.16 Image size with reference ruler highlighted, Trial 08 64
3.17 Measurement of the maximum flow front distance along major axes, Trial 08 66
3.18 Flow front position along the principal axes, Trial 08 69
3.19 Inlet gauge pressure as a function of the natural logarithm of EIS radius, Trial 08 71

4.1 Magnified zone close to the injection port, Trial 01 80
4.2 Inlet gauge pressure as a function of elapsed time, Trial 02 82
4.3 Dry spots present in the preform, Trial 02 83
4.4 End of test, Trial 03 86
4.5 End of test, Trial 04 88
4.6 End of test, Trial 05 91
4.7 Glass preform, Trial 06 92
4.8 Magnification of the glass preform, Trial 06 93
4.9 End of test, Trial 06 94
4.10 Post-compaction preform, Trial 07 95
4.11 End of test, Trial 07 97
4.12 Selected cycles of preform compaction, Trial 08 99
4.13 Glass preform, Trial 08 100
4.14 Magnification of the glass preform, Trial 08 100
4.15 End of test, Trial 08 102
4.16 Glass preform, Trial 09 103
4.17 Magnification of the glass preform, Trial 09 104
4.18 End of test, Trial 09 105
4.19 Fluid travelling along stitch line, Trial 10 107
4.20 Fluid at time $t_3 > t_2$, Trial 10 108
4.21 Maximum permeability as a function of fibre volume fraction for selected trials 110
4.22 Maximum permeability as a function of fibre volume fraction for preforms featuring 6 layers of glass 111

4.23 Maximum permeability as a function of fibre volume fraction for preforms featuring 6 layers of glass with $r_{f,\text{effective}} \approx 3 \cdot r_f$ 112
4.24 Yarn rearrangement near injection port 114
4.25 Compaction data for preforms manufactured using different numbers of layers 116
4.26 Compaction data for preforms manufactured using 6 layers 117

List of Tables

1.1 Typical values of selected physical properties for common engineering materials 3

2.1 Typical value of the numerical constant c in Equation 2.12 [38] 27

3.1 Sample data set with radii determined from injection side camera, Trial 08 . 68
3.2 Flow front radius and corresponding EIS radius 70
3.3 Natural logarithm of the EIS radius and corresponding inlet gauge pressure . 70

4.1 Parameters of trials conducted with Rig 1 75
4.2 Raw results obtained with Rig 1 76
4.3 Parameters of trials conducted with Rig 2 77
4.4 Raw results obtained with Rig 2 78

Nomenclature

ϵ	Preform porosity	
ϵ_B	Bulk strain	
μ	Dynamic viscosity	$[Pa \cdot s]$
ρ	Density of the fluid	$\left[\frac{kg}{m^3}\right]$
ρ_c	Density of the final composite part	$\left[\frac{kg}{m^3}\right]$
ρ_f	Density of the fibre	$\left[\frac{kg}{m^3}\right]$
ρ_r	Density of the resin	$\left[\frac{kg}{m^3}\right]$
θ	Angle between laboratory axis and major axis of the flow front	$[rad]$
A	Fibre volume fraction for a compaction pressure of 1 Pa	
a	Height of a curved fibre element	$[m]$
A_f	Cross sectional area of the fibre	$\left[m^2\right]$
A_{marker}	Area of the reference marker	$\left[m^2\right]$
$A_{preform}$	Preform top view area	$\left[m^2\right]$
B	Compaction stiffening index	

C	Pressure decay after 1 s	$\left[s^{-\frac{1}{D}}\right]$
c	Shape factor	
C_1	Gebart constant	
C_i	Instantaneous correction value related to the compaction testing apparatus strain	$[m]$
D	Relaxation index	
d_r	Relative difference in preform area due to compaction	
$D_{cylinder}$	Internal diameter of the hydraulic cylinder	$[m]$
E_f	Tensile modulus of the fibres	$[Pa]$
E_r	Tensile modulus of the resin	$[Pa]$
$E_{l,c}$	Longitudinal tensile modulus of a unidirectional composite	$[Pa]$
E_{rate}	Compressive displacement rate	$\left[\frac{m}{s}\right]$
$F_{Instron}$	Force recording from the Instron testing apparatus	$[N]$
g	Gravitational acceleration	$\left[\frac{m}{s^2}\right]$
h	Thickness of preform	$[m]$
$H_{cylinder}$	Stroke of the hydraulic cylinder	$[m]$
$h_{cylinder}$	Travel of the piston in the hydraulic cylinder	$[m]$
h_i	Instantaneous corrected thickness of the preform	$[m]$
H_o	Instantaneous spacing between the compaction plates as output by the compaction testing apparatus	$[m]$

K K_x K_y K_{xx} K_{yy} K_{xy} K_{yx}	Permeability values	$\left[m^2\right]$
k k_{xx} k_{yy} k_{xy} k_{yx}	Kozeny's constants	
$[\mathbf{K}]$	Permeability tensor	$\left[m^2\right]$
$\overline{K}$	Averaged permeability	$\left[m^2\right]$
K_e	Permeability in an equivalent isotropic system (EIS)	$\left[m^2\right]$
K_i	Instantaneous permeability	$\left[m^2\right]$
K_{Wyk}	Experimental constant	
K_{SS}	Permeability value generated using pressure data from the Setra Systems pressure transducer	$\left[m^2\right]$
K_{WT}	Permeability value generated using pressure data from the Wika Tronic pressure transducer	$\left[m^2\right]$

$[\mathbf{K}]_{SS}$	Permeability tensor generated using pressure data from the Setra Systems pressure transducer	$\left[m^2\right]$
$[\mathbf{K}]_{WT}$	Permeability tensor generated using pressure data from the Wika Tronic pressure transducer	$\left[m^2\right]$
L	Length of a volume element containing a representative fibre	$[m]$
m_f	Mass of fibres	$[kg]$
N	Number of data points over which the permeability values are averaged	
N_L	Number of layers in a preform	
$N_{\substack{marker \\ pixels}}$	Number of pixels in the reference marker selection	
$N_{\substack{preform \\ pixels}}$	Number of pixels in the preform selection	
$N_{K_{SS}}$	Number of data points over which the permeability was averaged using data from the Setra Systems pressure transducer	
$N_{K_{WT}}$	Number of data points over which the permeability was averaged using data from the Wika Tronic pressure transducer	
P_o	Inlet gauge pressure	$[Pa]$
$P_{p,o}$	Compaction pressure applied initially on the preform	$[Pa]$
P_p	Compaction pressure applied on the preform	$[Pa]$
q	Flow rate	$\left[\frac{m^3}{s}\right]$
R_f	Fibre radius	$[m]$
r_f	Flow front radius	$[m]$
r_o	Inlet radius	$[m]$
r_x	Minor radius	$[m]$
r_y	Major radius	$[m]$

r_{xe}	Radius in an equivalent isotropic system (EIS)	$[m]$
s	Sample standard deviation	
S_0	Specific surface	$\left[\frac{1}{m}\right]$
s_y	Yarn width	$[m]$
SA	Surface area of particles	$\left[m^2\right]$
$SE_{K_{SS}}$	Standard error of the mean for the permeability generated using data from the Setra Systems pressure transducer	$\left[m^2\right]$
$SE_{K_{WT}}$	Standard error of the mean for the permeability generated using data from the Wika Tronic pressure transducer	$\left[m^2\right]$
t	Time	$[s]$
$\overrightarrow{\boldsymbol{v}}$	Velocity	$\left[\frac{m}{s}\right]$
v_f	Fibre volume fraction	
v_o	Initial fibre volume fraction for an unstressed bundle, fibres touching	
v_r	Resin volume fraction	
v'_a	Fibre volume fraction for which all flow is stopped	
$v_{f,max}$	Maximum available fibre volume fraction	
~~V_c~~	Volume of final part	$\left[m^3\right]$
~~V_f~~	Volume of fibres	$\left[m^3\right]$
~~V_o~~	Initial volume of the fibres under no applied pressure	$\left[m^3\right]$
~~$V_{cylinder}$~~	Volume of the hydraulic cylinder	$\left[m^3\right]$
~~V~~	Volume of particles	$\left[m^3\right]$

Chapter 1

Introduction

1.1 Composite materials

Composite materials are a subset of engineering materials which are composed of two or more unique constituents. These individual constituents remain distinguishable in the finalized composite part, and the final macroscopic properties of the composite part are a result from the combination of the constituent properties. In the case of composites featuring two main constituents, these are often termed the reinforcement and the surrounding matrix.

Reinforcements studied in this thesis take the form of long fibres assembled into dry preforms made of glass or carbon fibres which are then infused by a liquid matrix that eventually cures into a solid polymer network. Epoxy is a subset of the polymer class of materials, hence, composite materials of this type are often termed polymer-matrix composites (PMC). The reinforcements typically feature high values of tensile modulus and strength; however, due to their small diameter, dry fibres can be subject to buckling under low compressive loads. The surrounding matrix is introduced to restrict fibre motion, transfer load to the fibres, and enable the construction of parts featuring fibres oriented in different directions. It also plays an important role in protecting fibres from the environment. The reinforcement fibres are manufactured such that their diameters are kept as small as possible, on the order of 10 μm to 20 μm. However, smaller fibre diameters introduce health issues; the main health concern being fibres with a very small diameter penetrating deeper into the lungs

when fibres are cut during manufacturing. Advantages to smaller diameter fibres are an increase in fibre-matrix interface area per fibre mass, resulting in an increase in load transfer between the matrix to the fibres; reduction in bend radius, resulting in less fibre breakage during handling; and longer fibres per fibre mass, resulting in less susceptibility to defects and cracks in fibres.

These small diameters result in very small interfibre gaps which must be filled by the matrix. Emphasis is placed on filling these small gaps because composite parts with poorly bonded fibres have decreased mechanical properties in comparison with composite parts which are fully wetted.

Advantages of PMCs arise from the combination of the most favourable properties from each of the constituent materials, mainly the low density of the matrix and the high stiffness and tensile strength of the fibres. Table 1.1 outlines typical values for important properties of common structural engineering materials as well as for constituent materials of the composite materials studied throughout this thesis.

Table 1.1: Typical values of selected physical properties for common engineering materials

Material	Density $\left[\frac{g}{cm^3}\right]$	Tensile modulus $[GPa]$	Ultimate tensile strength $[MPa]$	Specific tensile modulus $[GPa] \cdot \left[\frac{cm^3}{g}\right]$
1018-Steel CD[1]	7.9	205	475	26.0
6061-Aluminium[2]	2.7	68.9	310	25.5
Ti-6Al-4V Titanium[3]	4.4	114	950	25.7
Glass fibre[4]	2.6	80	2600	30.8
Carbon fibre[5]	1.7	239	4275	140.6
Epoxy[6]	1.1	3	70	2.7

Values for the selected properties given for the fibres themselves must be taken in context, as these values do not translate directly into properties for the final composite part using those fibres as reinforcement. In the most straightforward case of a composite part manufactured using unidirectional fibres, the longitudinal specific tensile modulus prior to fibre or matrix failure can be calculated accurately by applying the law of mixtures, Equation 1.1:

$$\frac{E_{l,c}}{\rho_c} = \frac{E_f \cdot v_f + E_r \cdot (1 - v_f)}{\rho_f \cdot v_f + \rho_r \cdot (1 - v_f)} \tag{1.1}$$

where $E_{l,c}$ is the longitudinal tensile modulus of the resultant composite part, E_f is the tensile modulus of the continuous reinforcement, E_r is the tensile modulus of the matrix, ρ_c is the density of the resultant composite part, ρ_f is the density of the reinforcement, and ρ_r is the density of the matrix. The physical properties for the constituent materials are

constants, hence the fibre volume fraction of the resultant composite part v_f is what can be modified between parts made of the same materials to yield different properties. The fibre volume fraction can be calculated using Equation 1.2. The resin volume fraction of the resultant composite part v_r is sometimes used and can be determined from Equation 1.3:

$$v_f = \frac{\cancel{V}_f}{\cancel{V}_c} = \frac{m_f}{\rho_f \cdot \cancel{V}_c} \tag{1.2}$$

$$v_r = 1 - v_f \tag{1.3}$$

where $\cancel{V}_f$ is the volume of fibres in the resultant composite part, $\cancel{V}_c$ is the volume of the resultant composite part, and m_f is the total mass of fibres in the resultant composite part.

A reasonable fibre volume fraction of 55% results in a specific tensile modulus of approximately 132.8 $GPa \cdot \frac{cm^3}{g}$ for the carbon fibre and epoxy values presented in Table 1.1. While this value represents a best case scenario where all fibres are laid parallel to the load, it is indicative of the performance in stiffness and weight reduction which can be achieved through the use of composites. Furthermore, the suitability of composites for applications requiring high stiffness and low mass may be extended to situations where applied loads are not well known. Figure 1.1 displays the correlation between stiffness and fibre orientation of a specific carbon fibre prepreg; in Figure 1.1a all fibres are laid in the same direction, whilst in Figure 1.1b half of the fibres are perpendicular, in the plane of the part, to the other half.

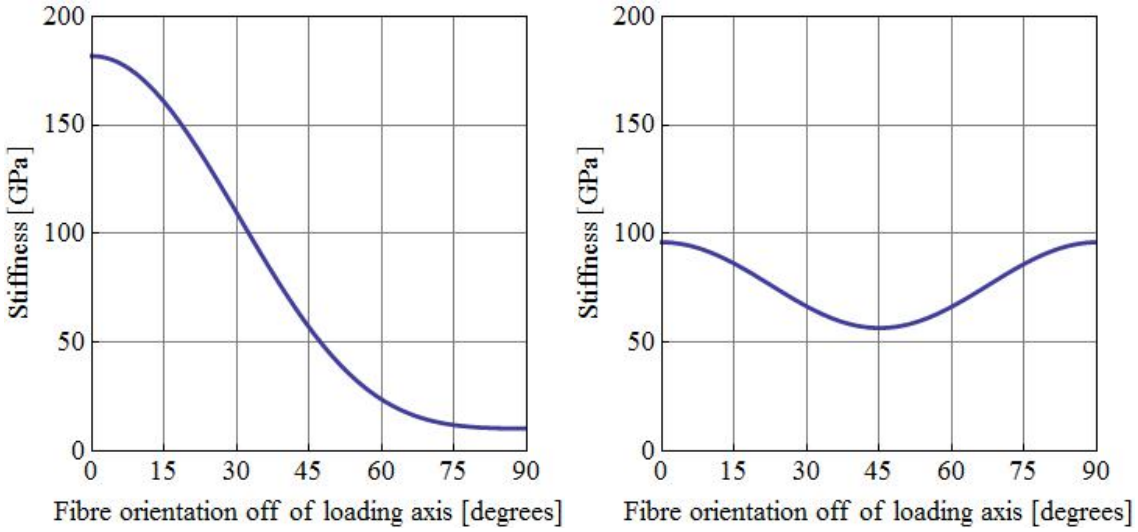

(a) Unidirectional prepreg (b) $[0, 90]_s$

Figure 1.1: Stiffness as a function of angle between fibre and loading axes

As a result of their high specific stiffness and strength, along with relative ease of processing and the ability to tailor part properties to their final application, adoption of PMCs in performance industry where mass reduction is second only to safety, has been high. A major example of applications of composites are commercial airplanes such as the Boeing 787 Dreamliner and Airbus A350 which are composed of 50% [7, 8] and 53% [9] composite materials by structural mass, respectively.

Other advantages over common engineering materials are the greater ease of assembly through part integration and the associated reduction in required parts [8], relatively low equipment and tooling costs, shorter cycle times, excellent design flexibility [10], corrosion resistance, virtually unlimited lifecycle under fatigue loading [11], and excellent resistance to thermal deterioration [12].

1.2 Manufacturing processes and preforms

1.2.1 Manufacturing processes

Manufacturing of composites can be done through mainly two different approaches. Essentially, what is required is the combination of the fibrous reinforcement and polymeric matrix, and the forming of combined materials into a final shape; either operation may be done first.

Manufacturing where combining is done first uses a semi-product called prepreg, shorthand for pre-impregnated, indicating that the fibres are impregnated with resin prior to forming.

If a thermosetting polymer is used, a relatively thin reinforcement layer is impregnated with the polymer in a continuous process which provides a uniform, continuous semi-product. The thin reinforcement layer is typically a very light array of collimated fibres or a light woven fabric. The uniform, continuous semi-product is rolled and delivered. Cure of the thermosetting polymer is slowed, but not stopped, by cooling the semi-product until it is to be used for manufacturing PMC parts. Since the curing process cannot be completely stopped, these prepregs have a finite shelf life. The process of manufacturing PMC parts using thermosetting prepreg begins by receiving the rolled semi-product, thawing it, cutting it into numerous pieces of appropriate shape, and painstakingly stacking the pieces of semi-product on a mould to take the shape of the final part. This stacking is done layer by layer where a great amount of effort is imparted in maintaining the designed fibre orientation. The stack is then bagged, vacuumed, and typically cured under a hot pressurized gas in an autoclave.

If a thermoplastic is used instead of the thermosetting polymer, then the roll of semi-product needs not to be kept cool because thermoplastic resins are essentially solid at room temperature. Therefore, forming must be done at elevated temperatures, limiting the thickness of the rolled product and the amount of deformation that the prepregs may withstand. Deformability of prepreg is an important factor because the prepreg must completely conform to the mould shape.

Structural PMC airframe parts are most often made from autoclave-cured prepreg because of the close tolerances and high specific properties which can be achieved. However,

recently airframe manufacturers have begun looking for alternative manufacturing methods such as liquid transfer moulding (LTM) processes for making primary and secondary load-bearing airborne structures and parts [12]. The main types of infusion-based moulding processes include resin transfer moulding (RTM), vacuum assisted resin transfer moulding (VARTM), and resin film infusion (RFI). These processes offer strong advantages in terms of cost of equipment and operation, as well as for the formulation and handling of resins.

In this group of manufacturing processes the forming of a dry reinforcement to the final shape of the PMC part is done first, and then a liquid resin is injected and combined with the fibrous reinforcement. Injecting a molten thermoplastic is typically much more difficult, due to the higher temperatures required for eventually getting somewhat closer to the low viscosities needed for injecting; as a result thermosetting resins remain prevalent.

There are several advantages to liquid transfer moulding over prepreg manufacturing and they are as follows: dry reinforcements are much easier to handle and to deform to the desired shape of the final PMC part when compared to prepreg. This is especially true in structural cases where high v_f and specific strength values must be achieved throughout the part using oriented fibres. Also, resin is only prepared upon manufacturing of the part, instead of manufacturing of the prepreg, which removes all aspects related to storing and using a semi-product such as cooling and thawing as well as protection from environmental factors such as humidity and condensation. Another advantage is that the fibre and resin may be selected independently, removing the prepreg supplier's limitations and costs.

Resin transfer moulding (RTM) is a manufacturing process where a mould cavity having the shape of the final PMC part to be produced, is carefully filled with dry fibres. Then, a resin is forced under an imposed pressure difference, most often generated through positive pressure and sometimes assisted with vacuum at the outlet, through the assembly of fibres which forms a porous media. Ideally the resin fills all the voids and once it is cured, the final composite part can be removed from the mould. In RTM the mould is stiff and made of minimally two parts, both using materials such as carbon fibre PMCs, aluminium, or Inconel. A typical RTM setup with additional vacuum support is displayed in Figure 1.2.

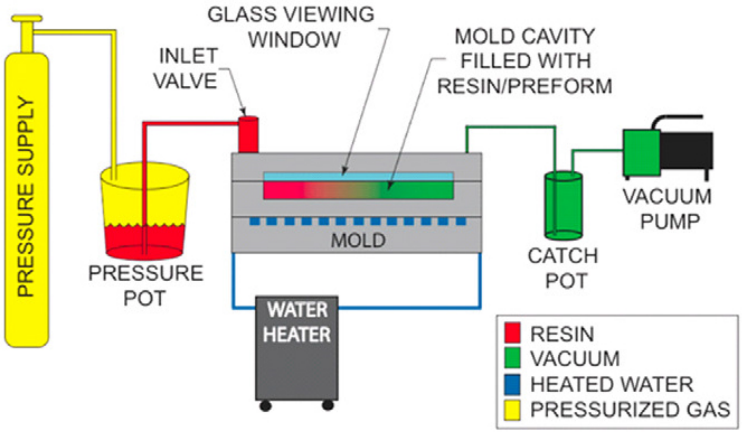

Figure 1.2: Typical RTM setup [13]

Vacuum assisted resin transfer moulding (VARTM) is similar to RTM. However, only one side of the mould needs to be stiff, while the other side of the reinforcement is enclosed in a sealed vacuum bag. Resin is drawn through the porous media by applying vacuum at the outlet with resin at the inlet is typically exposed to atmosphere, hence impregnation happens under a maximum pressure differential of one atmosphere. A typical VARTM setup is displayed in Figure 1.3.

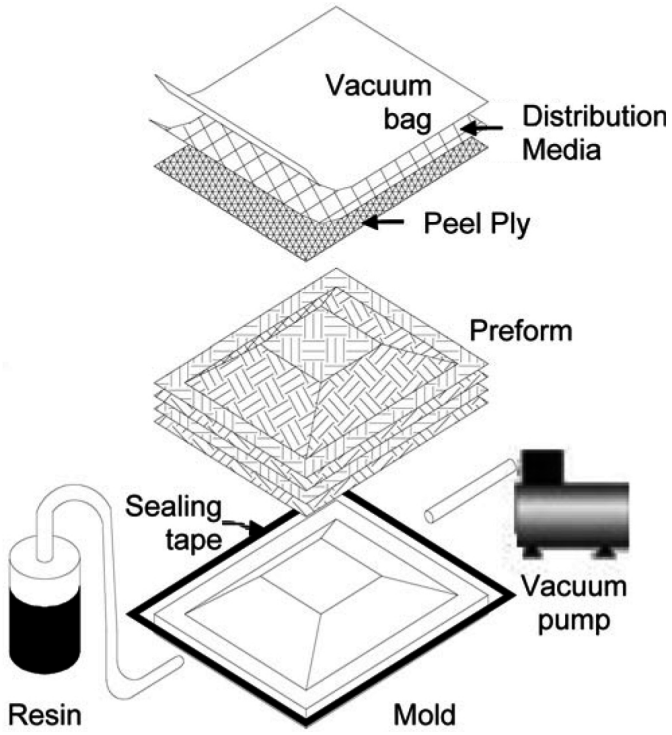

Figure 1.3: Typical VARTM setup [14]

Advantages of RTM over VARTM include the ability to operate at much higher pressures than atmospheric. This enables flow through a fibre bed with higher consolidation of the dry fibres, in turn allowing higher fibre volume fractions and thus higher specific stiffness and strength in the PMC part. Also, thickness and surface finish can be controlled to a much higher degree using two smooth, stiff mould halves; better surface finishes reduce stress concentrations on the surface and in turn increase performance. More importantly, they allow higher dimensional tolerances overall in assembled structures. From a manufacturing viewpoint, RTM also allows for higher production rates through easier automation once the preform has been placed into the mould. Furthermore, use of disposables such as pipes, infusion media, breathers, etc., can be eliminated making the process far more acceptable sustainability grounds.

Resin film infusion (RFI) is a process where a film of partially cured thermosetting resin is laid over a formed dry fibrous reinforcement. As with prepreg manufacturing there is a

requirement for bagging, vacuuming, and ideally autoclave curing of the stacked assembly, displayed in Figure 1.4. RFI offers some of the advantages associated with prepreg and liquid transfer moulding, but it is also plagued with the limitations of both processes. This process will not be discussed further as this thesis work applies to the manufacturing route whereby a dry, formed reinforcement is impregnated with a liquid thermosetting resin.

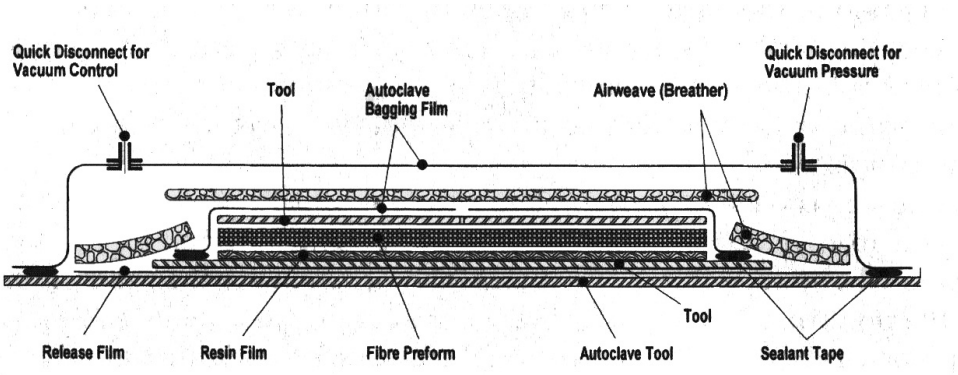

Figure 1.4: Typical RFI setup [11]

PMC part manufacturing using prepreg or RFI typically only features small scale resin flow; essentially flow only fills the gaps between successive layers of stacked prepreg, ensuring continuity of the cured part. Flow in RTM and VARTM liquid transfer moulding is significantly different because the resin must travel from the inlet and inwards, ultimately towards the outlet, a distance typically orders of magnitude larger than interlayer gaps. Also, for manufacturing to be successful, flow in this scenario must fully impregnate the numerous and very small interfibre gaps upon manufacturing. This results in a much larger scale flow when compared to prepreg manufacturing. The long scale flow coupled with complete impregnation remains a significant challenge to this day.

1.2.2 Preforms

The dry sheet of fibres which is placed into the mould is often called a preform. Realistic structural parts typically feature thick sections, integral flanges and/or assemblies of intersecting shells or other similar features. For these parts to be produced using RTM a

preform must be created through 3D and/or near-net-shape textiles; 3D and near-net-shape are characteristics of preforms which require little or no further assembly work, that are close to final shape, and require little or no further trimming. To realize the advantages of RTM, the production of thick, near-net-shape preforms with an ability to drape and bend well much be consistent. This can be achieved through 3D weaving, 3D braiding, knitting, and thick directional stitched preforms. The potential for automated production of net-shape preforms with controlled yarn orientations makes directionally stitched preforms suitable for RTM applications.

Preforms must have a certain stiffness to maintain shape as they are handled in the transfer from manufacturing to moulding; laying fibre directly in a 3D mould would be very difficult and lead to unacceptable mould downtime, hence is virtually never done. Preform stiffness can be generated through the use of tightly woven fabric, or by sewing layers of non-crimp fabrics (NCF). Both of these preforming techniques are illustrated in Figure 1.5.

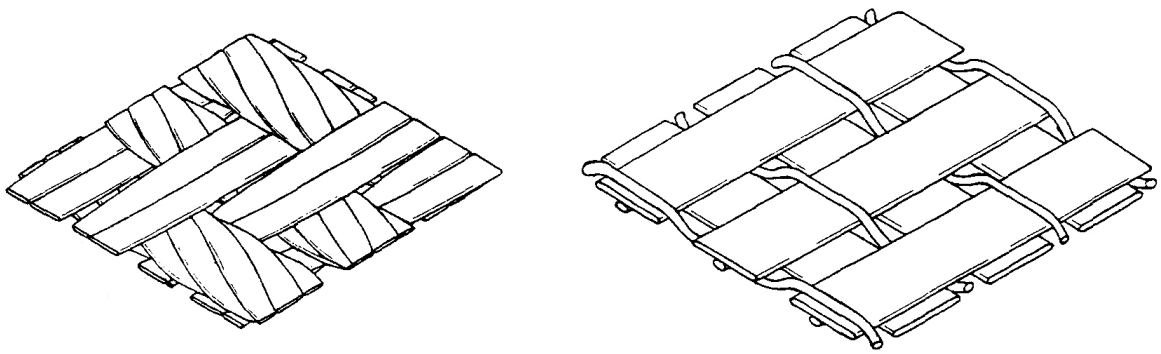

(a) Double twill woven roving (b) Stitched NCF

Figure 1.5: Two types of preforms [15]

Bends in fibres and yarns as they pass over or under another yarn within a fabric, which are introduced when weaving yarns to form the fabric, are termed ‘crimp’; an unloaded woven fabric is displayed in Figure 1.6 which displays crimp. Crimp introduces bending stresses in the fibres even in scenarios where the composite part is loaded in the same directions as the original fibre orientation. By constructing the preform out of successive layers of parallel dry fibres then stitching the stack together, crimp in the load-bearing yarn is reduced. The

reduction in crimp leads to a reduction in bending stresses in the fibres and can improve the overall in-plane stiffness and strength of the composite in comparison to woven fabrics. However, penetration of the needles through the yarns in the sewing process can create gaps, reducing v_f, or even damage the fibres, reducing stiffness and strength.

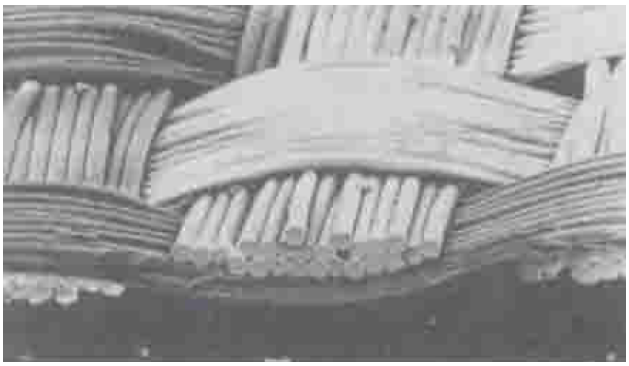

Figure 1.6: Crimp of fibres caused by weaving [16]

While stitching has occasionally been used for reinforcing prepreg laminates, the tackiness of the uncured resin makes the sewing process difficult and also leads to fibre damage. Stitching is mostly used to sew dry fabric preforms [12]. The stitching process often limits the size of the preform, especially in thickness because of the requirement of the needle to pass completely through the preform. Different stitching techniques are possible, however the most common technique is single-needle machines which require access to both sides of the preform.

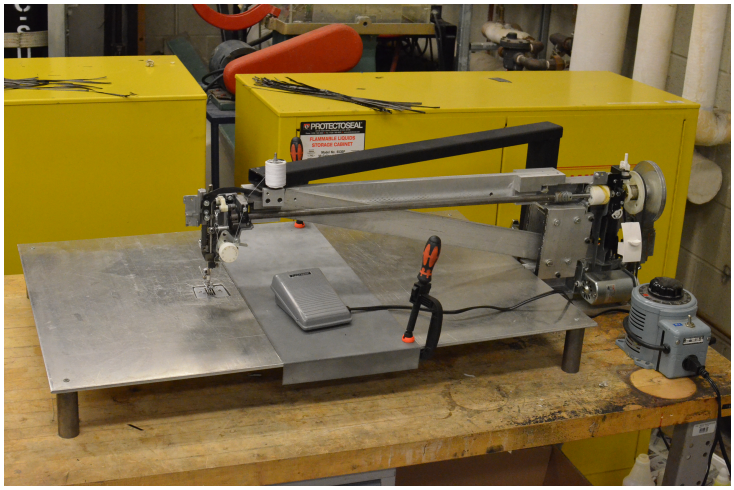

(a) Sewing machine used

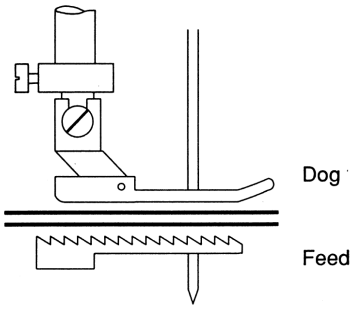

(b) Schematic diagram of stitching head [17]

Figure 1.7: Sewing process

Furthermore, different stitch types are possible, the most common type being the lock-stitch displayed in Figure 1.8a. This type of stitch causes more resin rich zones than the modified lock stitch [18], Figure 1.8b, hence the modified lock stitch type is used in the preforming done for this thesis. Resin rich zones will be discussed at length in Section 2.2.

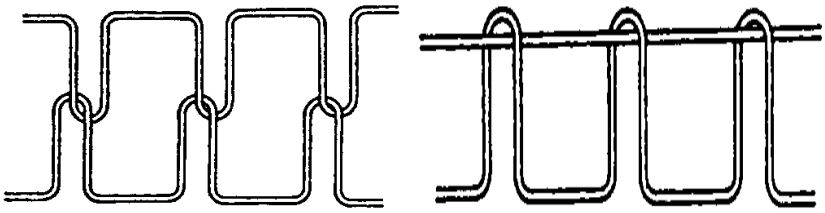

(a) Lock stitch (b) Modified lock stitch

Figure 1.8: Common stitch types [17]

The final properties of the composite part are strongly correlated to the properties of the preform. Two critical aspects of the final part, fibre orientation and much of the yarn spacing, are mostly determined upon preform manufacturing. Imperfections, such as inconsistent fibre spacing which can arise from local stitch tension or mishandling of tows,

cause macroscopic variance in the final part leading to resin-rich zones which are widely acknowledged as points of structural weakness.

Throughout this thesis, preforms were made through manual laying of tows. Individual yarns measuring approximately 4 mm in width were laid onto a pin board until a base layer had been formed. The pin board was rotated to the next desired fibre orientation whereupon another layer was laid. This process was repeated until the desired amount of layers was completed. The amount of layers was dependant on the desired thickness of the preform, the desired fibre volume fraction, and the yarn properties. The required number of layers based on these criteria can be calculated using Equation 1.4 [11]:

$$N_L = \frac{s_y \cdot v_f \cdot h}{A_f} \tag{1.4}$$

where N_L is the number of layers in the preform, s_y is the spacing between subsequent yarns on the same layer of a preform, A_f is the cross sectional area of the yarn, and h is the desired thickness of the preform.

Equation 1.4 does not typically yield an integer value for the number of layers in the preform so adjustments to the fibre volume fraction or the preform thickness must be made to suit the final application of the composite part. Furthermore, practical limits to the fibre volume fraction exist; these limits will be discussed in Section 2.3.

Attention to detail was of high importance. However, due to the nature of manual processes, defects were observed. An example of this can be viewed in Figure 1.9b, in that the stitches locally squeezed yarns by varying amounts. At a local level this causes resin rich zones, decreasing the fibre volume fraction and therefore potentially reducing the strength. More to the point, the presence of open channels for the preferential flow of resin had very strong effects on the dynamics of impregnation; this will be discussed in detail in Section 2.2. Whilst this may ultimately be used as an enabling feature, changes to impregnation progress are profound, and major issues were observed and documented. These aspects constitute the core of the results and contribution of this thesis.

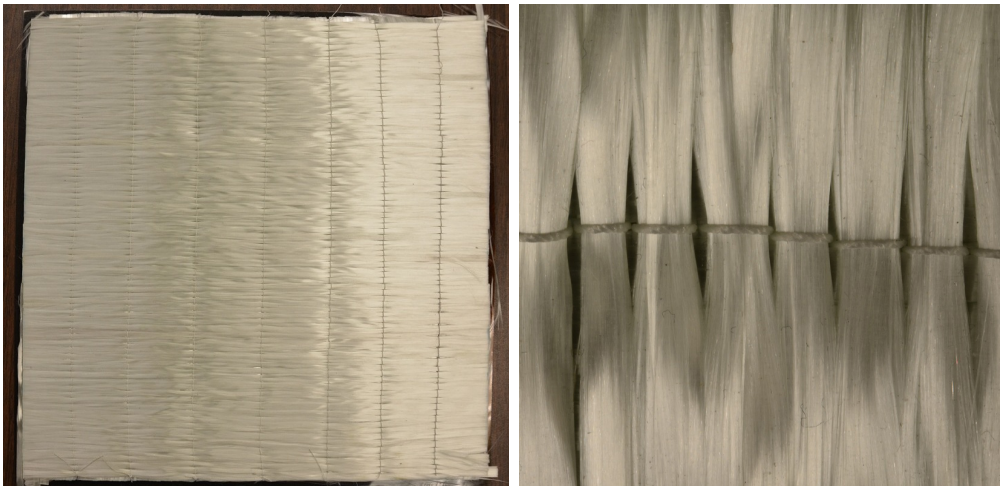

(a) Full preform, approximately 320 mm by 320 mm

(b) Zoomed in section of the glass preform displaying the stitches

Figure 1.9: NCF preform composed of 6 layers of glass fibre

1.3 Thesis overview

Knowledge of how fluids flow through porous media is critical in the manufacturing of composite materials, and especially so for optimizing the LTM manufacturing process where uncured epoxy must completely saturate a dry preform and fill the cavity of a mould. A new concept of net-shape, final thickness preforms featuring directional yarns stitched through-thickness is introduced as a development to studies on fluid transport through composite materials. The work performed in this thesis is required to better understand the effect of these stitches. This through-thickness stitch is a requirement of the preform manufacturing process as previously discussed. Specifically the objective of this work is to determine the effect of this type of stitching on the LTM injection process. Other parameters were altered in an attempt to improve the uniformity of the flow front throughout the injection process; these parameters include fibre volume fraction, imposed flow rate, as well as different degrees of fibre consolidation.

This work involved performing numerous experimental trials on different preforms to study the effects of those different parameters on the flow progression through the preforms. The results from the experiments will ultimately be able to inform preform design and modelling software on how preform properties will affect the pressure distribution on a mould surface as well as the fluid flow velocity.

Chapter 2

Literature Review

2.1 Permeability

Permeability is the ability of a porous material to allow fluids of known viscosity to flow through its internal structure under an imposed pressure gradient. In the context of composite manufacturing, permeability is the measure of the ability of a preform to allow a fluid, typically resin, to flow from an inlet port to an outlet, or vent. The importance of this parameter is paramount as it dictates the pattern of resin flow upon mould filling and can be used for modelling and predicting resin flow during that phase. Since the preform is not homogeneous nor composed of perfectly parallel fibres the permeability of the material will vary locally within the preform. Mesoscopic heterogeneities in the preform include inter-yarn spacing and stitching related defects. The variable local permeability coupled with an imposed pressure will result in a velocity profile at the flow front and throughout the wetted part of the preform which will not be constant. This field of velocity vectors will most commonly result in an orthotropic permeability, most readily viewed in Figure 2.2.

The most basic equation used for studying the flow field is the continuity equation:

$$\frac{\partial \rho}{\partial t} + \nabla \cdot \left(\rho \overrightarrow{\boldsymbol{v}}\right) = 0 \tag{2.1}$$

where $\frac{\partial \rho}{\partial t}$ is the partial derivative of the fluid density ρ with respect to time t. The expression $\nabla \cdot \left(\rho \overrightarrow{\boldsymbol{v}}\right)$ is the divergence of the fluid density multiplied by the velocity vector $\overrightarrow{\boldsymbol{v}}$.

In the scenarios studied experimentally in this thesis, the fluid is either epoxy resin or silicone oil, both of which can be assumed incompressible. This reduces the continuity equations to a simpler form:

$$\nabla \cdot \overrightarrow{\boldsymbol{v}} = 0 \tag{2.2}$$

Darcy's law can be applied to relate fluid flow rate and imposed pressure gradient through physical constants:

$$\overrightarrow{\boldsymbol{v}} = \frac{-[\mathbf{K}] \cdot \nabla \mathbf{P}}{\mu} \tag{2.3}$$

where μ is the dynamic viscosity of the fluid and $[\mathbf{K}]$ is the permeability tensor. The $\cdot$ used in Equation 2.2 is the only instance of a dot product used in this thesis. All succeeding instances of the $\cdot$ are notations of multiplication. This notation is included to make the variables and constants used in equations easier to distinguish.

Darcy's law, originally proposed in 1856 [19], has more recently been derived theoretically with the assumptions of fully saturated Newtonian flow through a semi-infinite, uniformly porous media [20]. Flow through a medium which is fully saturated by the travelling fluid is referred to as saturated flow, whereas unsaturated flow is flow through a medium which contains voids composed of different fluids such as air. Diagrams of saturated and unsaturated flow are displayed in Figures 2.1a and 2.1b. While permeability values can be determined using saturated flow, the liquid transfer moulding manufacturing processes previously described usually involve unsaturated flow through finite heterogeneous media. As a note, unsaturated permeability values are typically higher than saturated permeability values [21] and are also variable with flow rate [22]; hence, proper understanding of the derivation assumptions or experimental process must be had to apply the values to liquid transfer moulding. Current simulation models rely extensively on Darcy's law and practical measures of permeability based mostly on unsaturated flow are used [21]. Furthermore, the assumption of uniformly porous media for which Darcy's has been derived remains applicable for most liquid transfer moulding applications [23].

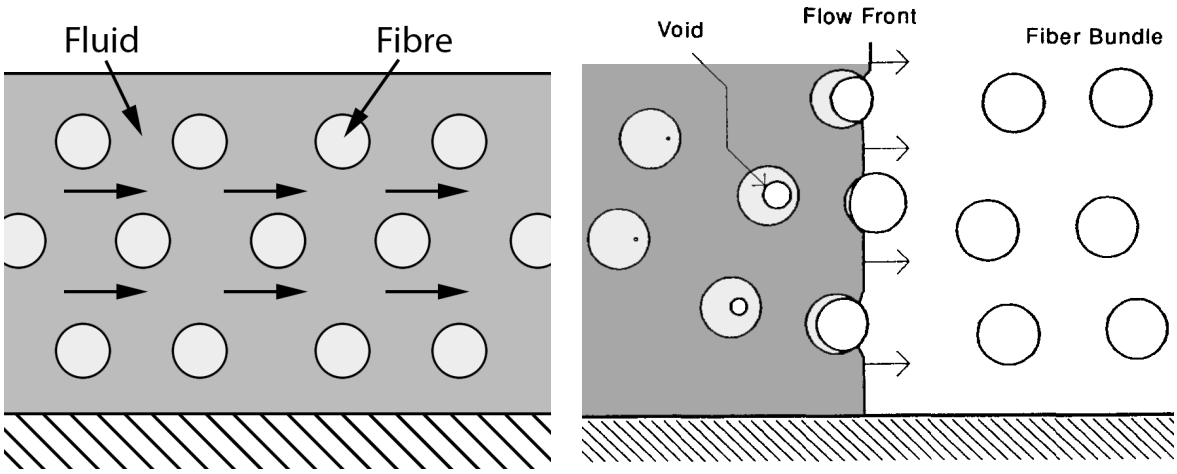

(a) Saturated flow (b) Unsaturated flow [24]

Figure 2.1: Different flow regimes

If the permeability tensor can be identified by applying Darcy's law the relationship between velocity and pressure can be determined. This is critical to manufacturing because a balance must be reached between maximum pressure, dependent on manufacturing mould deflection, and velocity, dependent on gel time of the epoxy. The maximum pressure must not cause the mould to deflect to any significant degree, or separate.

In-plane, 'pseudo' two dimensional flow also known as plug flow corresponds well to the reality of resin flow upon manufacturing of a typical thin shell-like part using RTM. For such a flow where the flow front is assumed to be uniform across any cross-section normal to the mould surfaces, the form in which the permeability tensor can be expressed most generally is:

$$[\mathbf{K}] = \begin{pmatrix} K_{xx} & K_{xy} \\ K_{yx} & K_{yy} \end{pmatrix} \tag{2.4}$$

The through-thickness permeability K_{zz} is typically much lower than in-plane permeability terms [25]; ratios on the order of 6 to 8 times have been recorded [21]. The effects of this on in-plane flow will be discussed in Section 4.

Several distinctly different simplifications of this system may arise, specifically isotropic and general orthotropic cases. Furthermore, the general orthotropic case can often be sim-

plified to an orthotropic case through a change in coordinates. These three flow scenarios are outlined in Figure 2.2.

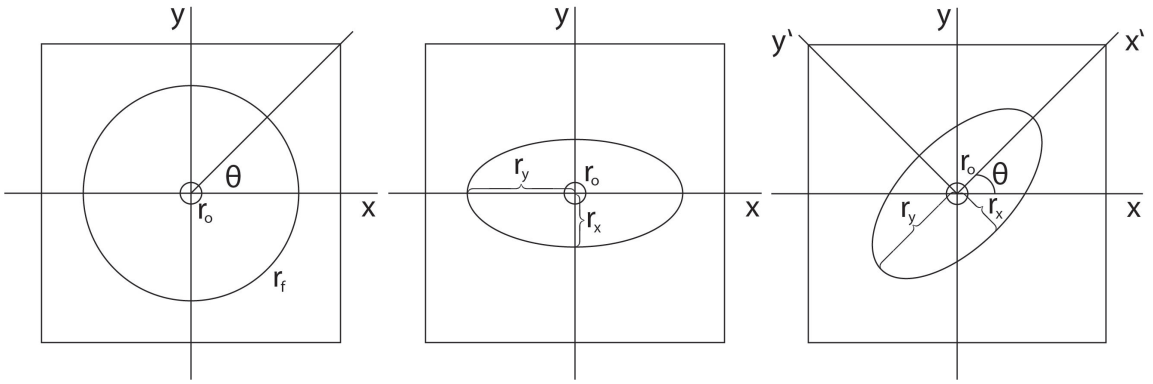

(a) Isotropic (b) Orthotropic (c) General orthotropic

Figure 2.2: Different flow patterns derived from Darcy's law

The most simple case of 2D in-plane flow described using Darcy's law is isotropic flow. This case arises when the flow front progression from a central resin inlet is independent of orientation as displayed in Figure 2.2a; the radius of the flow front varies with time only. In this case the permeability tensor simplifies to:

$$[\mathbf{K}] = K \begin{pmatrix} 1 & 0 \\ 0 & 1 \end{pmatrix} \tag{2.5}$$

In the case of flow front progression which does vary with orientation, the permeability tensor cannot be simplified to the same extent. If, however, the principal axes of the elliptical flow front coincide with reference axes, then the flow and resulting permeability tensor fall under the orthotropic case. It should be noted that tensor theory can be used in demonstrating that in the orthotropic case the directions of highest and lowest permeability are necessarily orthogonal; however, the term "elliptical" is used in a general sense and the flow front is not rigorously an ellipse. An example of the resulting flow pattern appears in Figure 2.2b. The permeability tensor is a constant with regards to both position and time, but the values of its components in each direction vary; they may be best expressed by the

principal permeabilities corresponding to directions of smallest and largest resistance to flow along the major and minor axes, respectively. This tensor is defined in Equation 2.6:

$$[\mathbf{K}] = \begin{pmatrix} K_x & 0 \\ 0 & K_y \end{pmatrix} \tag{2.6}$$

The final case which may occur according to Darcy's law is where the principal axes of the flow front do not coincide with the reference axes system. This final case is the general orthotropic flow condition and it is displayed in Figure 2.2c. This is the most general form of the 2D permeability tensor discussed in this thesis:

$$[\mathbf{K}] = \begin{pmatrix} K_{xx} & K_{xy} \\ K_{yx} & K_{yy} \end{pmatrix} \tag{2.7}$$

All of these permeability values have been derived such that they are assumed constant for a given preform, regardless of position. A more accurate model would be to use microscopic analysis to account for any variability of the fibre geometry; however, this type of analysis is currently far too laborious and makes it unfeasible for any industrial application. Hence, this constant permeability model is widely used in industrial applications [21] and is the model which is applied throughout this thesis.

From work done by Chan, *et al.* [26, 27] and Adams, *et al.* [28], these permeability values can be determined from experimentally obtainable data. Relevant equations will be applied in the data analysis Section 3.2.2 and also in Appendix 5.

While the method for determining permeability described above is widely used, accurately determining permeability values can lead to numerous difficulties with some preforms. One difficulty which has previously been mentioned is mould deflections which can cause errors of 50% [21]. While this can be mitigated by proper mould design, other issues, such as flow induced mat-compression can be more difficult to correct. Flow induced mat-compression is caused by the pressure of the viscous fluid causing the preform to compress locally under the inlet, where the pressure differential is highest, creating flow around the preform rather than through it [25]. These two flow fronts can be viewed in Figure 2.3.

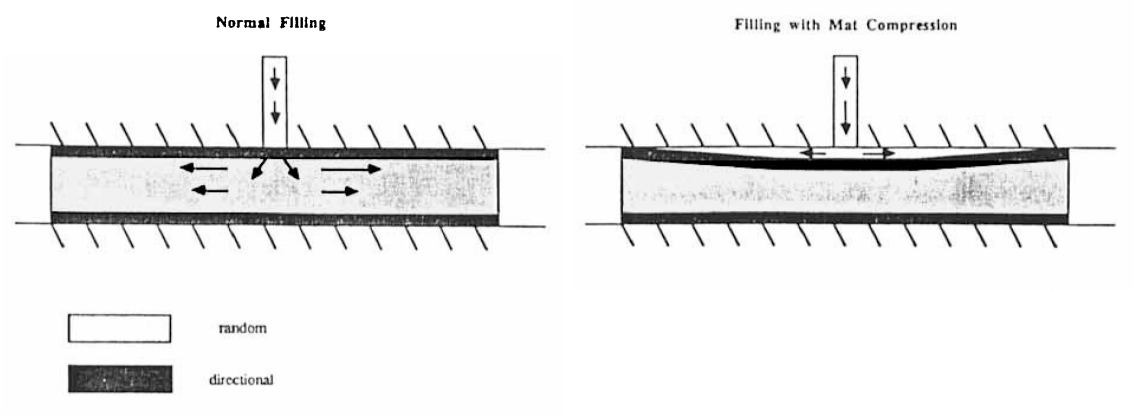

(a) Normal flow through the porous media (b) Flow induced mat-compression

Figure 2.3: Flow scenarios near injection port [25]

The prevalence of this type of flow can be reduced by designing the preform such that the closing pressure of the mould is well into the exponential region of the compaction pressure. This will be explained further in Section 2.3.

Even with well-designed moulds and preforms, the microstructure of the preform plays a crucial role in defining the flow field, and thus the permeability [10, 29, 21, 23]. A uniform surface density was used in the derivation of Equation 1.4. This was acceptable for calculating the number of layers; however, it directly correlates the fibre volume fraction to the surface density. Non-uniform surface densities are typical, even for a single roll of woven fabric, thus the local v_f is non uniform. Variation in surface density for stitched non-crimp fabrics is also typical. Determining, or even measuring, any property at arbitrary points in the preform is very difficult.

Permeability is also very sensitive to fibre misalignment when preforms have high fibre volume fractions. As can be seen in Figure 2.4, permeability values can vary by more than an order of magnitude depending on the type of reinforcement, and/or the way in which the preform is assembled, stitched or woven. Also, even for the the same fibre type and assembly process large variations of permeability can be seen, in Figure 2.4 as well as in Figure 2.5.

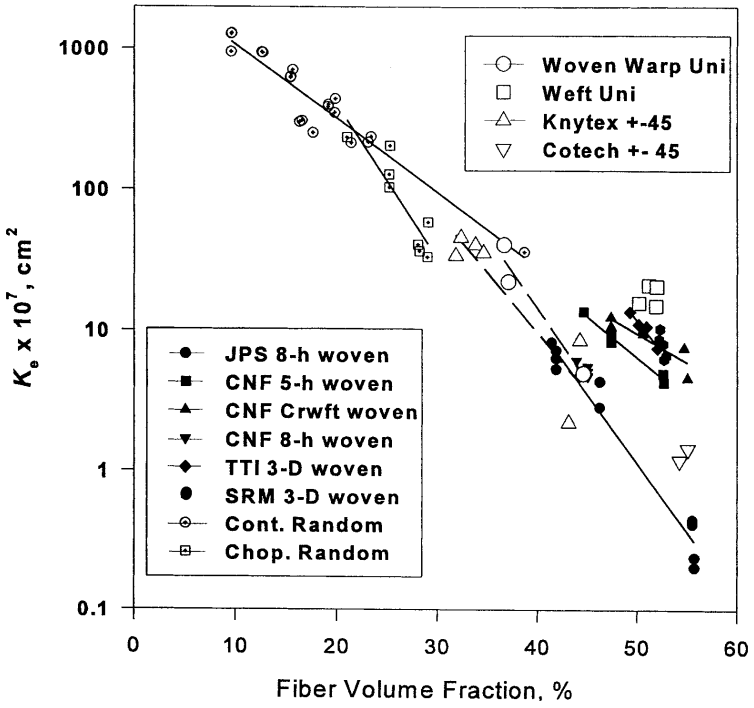

Figure 2.4: Permeability variation as a function of fibre volume fraction [21]

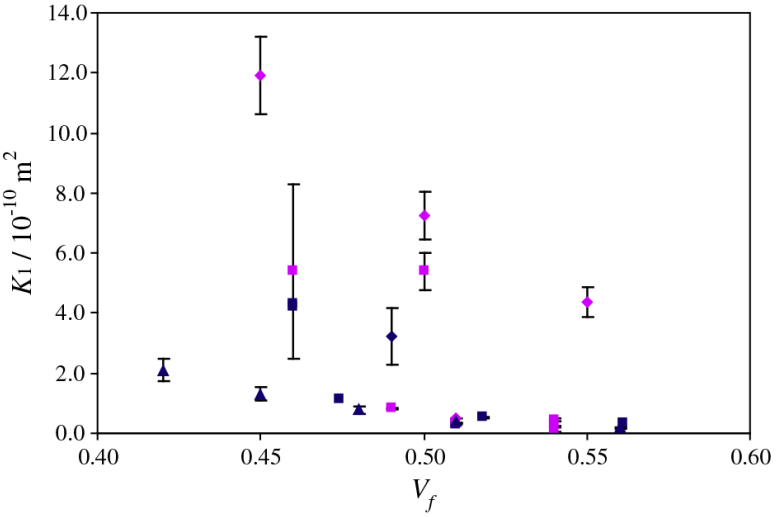

Figure 2.5: Measured permeability of a single fabric type [30]

As a result of these issues attempts to accurately determine permeability values, even through well controlled one-dimensional and two-dimensional experiments, still yield large variations [10, 30].

A permeability database with results from carefully controlled measurements for both saturated and unsaturated flows was created by the National Institute of Standards and Technology [21], however it has since been discontinued [31].

Predicting permeability accurately for aligned fibres is also difficult. One of the most famous models for predicting permeability is for a rigid bed of particles with uniform size and shape [32]. This model was initially developed for a packed bed of uniform spheres and results in an isotropic flow field such that the permeability can be calculated from Equation 2.8. This equation is referred to as the Kozeny-Carman equation:

$$K = \frac{g}{k \cdot S_0^2} \cdot \frac{\epsilon^3}{(1-\epsilon)^2} \tag{2.8}$$

where g is gravitational acceleration; k is the Kozeny constant, 5.0; and S_0 is the specific surface, defined in Equation 2.9:

$$S_0 = \frac{SA}{\not{V}} \tag{2.9}$$

where SA is the surface area of the particles making up the rigid bed and $\not{V}$ is the volume of those particles.

While this equation works well for packed beds with spherical particles it must be altered to predict more accurately the permeability across collimated fibres. Gutowski *et al.* proposed Equation 2.10 as an altered form of the Kozeny-Carman equation for predicting permeability in transverse flows [33, 34]. Equation 2.11 is a rearrangement of Equation 2.8

for the purpose of displaying similarities between Equation 2.11 and 2.10.

$$K_{ii} = \frac{R_f^2}{4 \cdot k'_{ii}} \cdot \frac{\left(\sqrt{\frac{v'_a}{v_f}} - 1\right)^3}{\left(\frac{v'_a}{v_f} - 1\right)} \tag{2.10}$$

$$K_{\parallel} = \frac{R_f^2}{4 \cdot k_{\parallel}} \cdot \frac{(1 - v_f)^3}{v_f^2} \tag{2.11}$$

where R_f is the fibre radius, $k_{\parallel}$ is the Kozeny constant for fluid travelling parallel to the fibres, k'_{ii} is the Kozeny constant in the transverse directions of the fibres, and v'_a is the volume fraction for which all flow is essentially cut off [33].

Note that for unidirectional fibres aligned in a given x-direction, $K_{yy} = K_{zz}$ [35].

Kozeny constants were determined experimentally to be 0.7 in the direction parallel to the fibres and 0.2 in the transverse direction, for a v'_a of approximately 76%. Even under well-controlled conditions, variations of ±35% were observed. The spread of Kozeny constants derived by Gutowski *et al.* can be viewed in Figure 2.6a while Figure 2.6b displays both experimentally derived and theoretical models of the Kozeny constant from different authors.

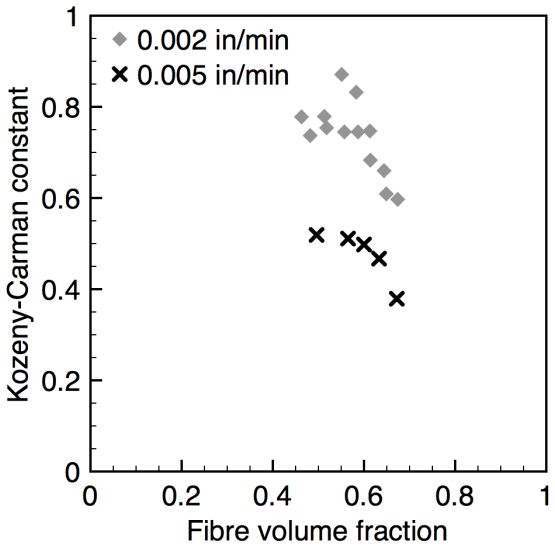

(a) Gutowski *et al.* experiment as a function of fibre volume fraction and flow rate [35]

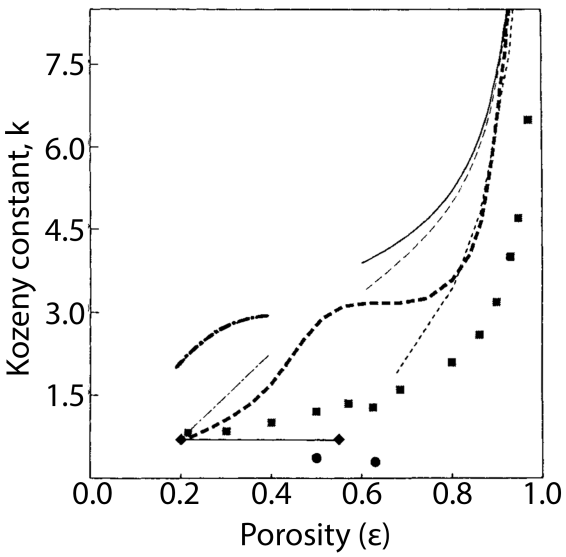

(b) Various experiments and models as a function of porosity [36]

Figure 2.6: Experimentally and theoretically derived Kozeny constants

Skartsis *et al.* suggest that due to the large variations in the Kozeny constant displayed in Figure 2.6b, the Kozeny-Carman relation cannot predict the permeability accurately, either in-plane or transverse [36, 37].

However, after Gutowski, Gebart derived a relationship between Kozeny constant for flow parallel to the fibres and geometric properties, for Newtonian creeping flows, $Re_{D_h} \ll 1$ [38]:

$$k_{\parallel} = \frac{c}{32} \tag{2.12}$$

where c is a shape factor corresponding to the flow cross section shape. Typical values of c appear in Table 2.1.

Table 2.1: Typical value of the numerical constant c in Equation 2.12 [38]

Cross Section Shape	Value of c
Right-angle isosceles triangle	52
Equilateral triangle	53
Square	57
Circle	64
Rectangle (3.1 : 1)	71
Annulus (d1/d2 $\rightarrow$ 1)	96

Gebart suggested using a cross-section shape of quadratic or hexagonal fibre packing, which results in equivalent Kozeny constants of 1.78 and 1.66, respectively.

Gebart also derived models for permeability perpendicular to the fibres:

$$K_{\perp} = C_1 \cdot \left(\sqrt{\frac{v_{f,max}}{v_f}} - 1 \right)^{5/2} \cdot R_f^2 \tag{2.13}$$

where C_1 is a parameter which changes based on the fibre arrangement; C_1 varies between $\frac{16}{9\pi\sqrt{2}}$ and $\frac{16}{9\pi\sqrt{6}}$ for square packing and hexagonal packing, respectively. Also, the maximum available fibre volume fraction $v_{f,max}$ typically varies between $\frac{\pi}{4}$ for square packing to a maximum of $\frac{\sqrt{3} \cdot \pi}{6}$ for hexagonal packing of cylindrical fibres.

These permeability predictions are based on a stacked layers of parallel fibres all oriented in the same direction. In most cases the PMC is a combination of several layers of parallel fibres aligned in different orientations, hence a weighted averaging of permeability with percentage thickness is sometimes applied [39]:

$$\overline{K}_{uv} = \frac{1}{h} \cdot \sum_{j=1}^{n} h^{(j)} K_{uv}^{(j)} \tag{2.14}$$

where j is an individual layer of yarns, $h^{(j)}$ is the individual layer's thickness, $K^{(j)}$ is the individual layer's in-plane permeability, and h is the total thickness of the stacked layers.

This type of averaging does not include traverse flow between subsequent layers and is only applied due to its simplicity.

Work has been done to model the effective permeability of multi-layered preforms, including transverse flow between layers [29, 40]. The resultant equations for permeability take on the form of a summation of weighted permeabilities of individual layers, Equation 2.15. The weighting is a relationship between the length of the flow front in an individual layer to the arithmetic average length of the flow front.

$$\overline{K}_{TF} = \frac{1}{h} \cdot \sum_{j=1}^{n} w_j \cdot K_j \cdot h_j \tag{2.15}$$

where;

$$\overline{r}_f = \frac{1}{h} \cdot \sum_{j=1}^{n} \frac{r_{f,j} \cdot h_j}{N_L} \qquad\qquad w_j = \frac{\overline{r}_f}{r_{f,j}}$$

Numerical solutions are required for calculating $r_{f,j}$ and $\overline{r}_f$ for preforms fabricated with more than two layers [39].

These methods essentially aim to correlate inlet pressure and elapsed time to the flow front positions. While these are important parameters to determine prior to injection; the reproducibility, robustness, and uniformity of the flow front are of greater significance. For a manufacturing process to be adopted the manufactured parts must have consistently reproducible properties between subsequent cycles. For properties of PMC parts to exceed typical engineering materials and compare with the theoretical properties attainable, the fibres must be fully wetted by the matrix.

2.2 Effects related to stitching

With the marked shift towards non-crimp fabrics (NFCs), increased attention has also been devoted to the effects of stitching. Classic NCFs are formed from stacks of individually knitted fabrics. As previously stated in the introduction, the NCFs studied here are stacked and then stitched through-thickness to form a preform which may be handled with less

difficulty. Knitted NCFs have limited fibre volume fractions and low structural properties which make them unsuitable as reinforcements for structural parts. The stitched NCFs studied here do not suffer from these disadvantages. The stitching results in variations in the microstructure of the preform. These changes in microstructure will affect not only the permeability, as previously mentioned, but also the in-plane and interlaminar strength.

In the stitching process, the needle punctures the surface of the preform, spreads the fibres and leaves a thread in its place as it is removed. The needle does displace and can damage the fibres locally; however, the effect is typically controlled for dry preforms with less than 0.5% of fibres broken [18, 41]. The majority of the change in in-plane mechanical properties arises from the spreading of the fibres. The spreading of fibres has a twofold effect on the mechanical properties. First, locally around the stitch a fibre-free zone is created. Second, the fibres are no longer parallel throughout a layer.

As previously mentioned, increasing the fibre free zones or resin rich zones is commonly regarded as having a detrimental effect on the mechanical properties of the final composite part, primarily strength. Different stitch tensions and different stitch densities cause different amounts and sizes of these resin rich zones; in either case the volume created has significant effects on the flow pattern and mechanical properties. Higher stitch tensions cause the fibres to compact locally to higher levels, leaving high volumes of resin rich zones. For a composite with a nominal v_f of 50% the v_f can increase to up to 70% [41, 42]. Models have been proposed for determining the size of these resin rich zones around stitches based on the compressed stitch diameter [41, 42] but they require detailed micrographs of the finalized part as input to the model. The proposed models reflect the deformation zones displayed in Figure 2.7. The four zones described by Wei *et al.* are I) undistorted region, II) fibre distorted region, III) resin rich pocket, and IV) the through-thickness reinforcement region [41].

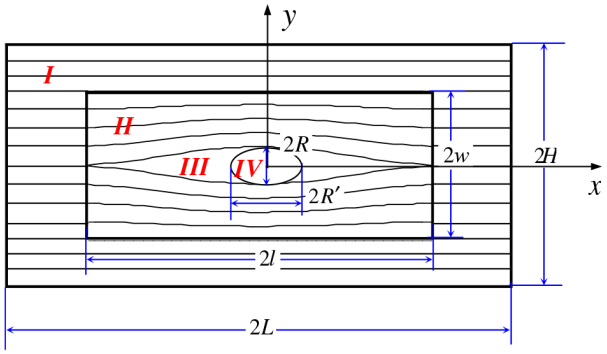

Figure 2.7: Zones surrounding a stitch in NCF [41]

From experimental and analytical data, the local change in orientation of fibres can vary by up to 20°; however, variations of 4.0° to 5.5° are more typical [41, 43]. Such changes in fibre orientation can reduce the strength drastically. Furthermore, structural threads are more prone to displacing fibres because they typically have larger diameters, the main contributor to fibre misalignment.

Stitching is a cost-effective method for improving through-thickness mechanical properties. Stitching increases the interlaminar fracture toughness as well as the resistance to low velocity impact damage. This increased resistance to low velocity impact damage is significant as a common cause for delamination is dropped tools. Stitches close to a free edge also reduce the occurrence of free edge delamination, these sites being where the surrounding environment can damage the core of a PMC part resulting in significantly reduced mechanical properties [17]. So while stitching is mainly introduced for improving the ability to handle a preform, it can offer other significant benefits.

Permeability along the direction of the stitch, or production direction, is also changed drastically. In-plane permeability in the direction of the stitch has been shown to increase by a factor of two to three [29] from the in-plane permeability in the direction perpendicular to the stitch; again, variability is typically quite large and difficult to predict [18]. This increase in permeability is caused by the fibre-free zones close to the stitch creating preferential fluid pathways. The size of these pathways is difficult to predict and is a function of stitch tension, stitch density, and other preform variables. Similarly to the change in fibre orientation, the permeability is affected by lower stitch densities, lower stitch tension, and lower thread

density. In a worst case scenario these open channels can become sufficiently long to form continuous channels where fluid can travel with much less resistance [43]. This is considered a worst case scenario because if the fluid travels preferentially along these channels to the exit ports instead of penetrating the tows then the preform will not be completely filled. Preforms which are not completely filled have significantly reduced mechanical properties and are not appropriate for load bearing parts.

Through-thickness permeability is typically significantly lower than in-plane permeability and is subject to additional difficulties in measurement, mostly related to the short flow distance available for forming a flow front, and to the large size of this flow front. Repeatability of measurements for through-thickness permeability is also a challenge [44]. For NCFs, the through-thickness permeability is independent of stacking sequence and stitching pattern. For the same stitch density and preform type, the permeability is a dependent on only the diameter of the stitch and can be determined by the relationship;

$$k_{33}^{d1} = k_{33}^{d2} \cdot \frac{d1}{d2}$$

where k_{33}^{d1} is the transverse permeability for a preform with stitch diameter $d1$ and k_{33}^{d2} is the permeability of a preform with the same stitch density but a different stitch diameter $d2$ [44]. k_{33}^{d1} is determined experimentally.

When modelling the flow through stitched NCFs the interbundle channels contribute nearly 100% to the flow, while flow through the bundle can be neglected [29, 44, 45]. This is especially true for transverse permeability where fluid is observed to flow mainly through the stitch holes while flow across tows is very limited.

2.3 Compaction effects

To obtain the relatively high fibre volume fractions required for structural PMC parts, typically between 50% to 70%, reinforcements must be compacted.

Study of the compaction behaviour of reinforcements ultimately dates back to 1946 with van Wyk, who proposed a method for determining the pressure required to compact wool to

a desired volume, a function of v_f. This early model only considered bending of the fibres; contacts between different fibres corresponded to reaction forces on an equivalent fibre 'rod'. This model also assumed that the fibres were oriented at random, uniformly packed, and neglected friction or slippage [46]. This early relationship, at high degrees of compression, is stated as Equation 2.16:

$$P_p = \frac{K_{\text{Wyk}} \cdot E_f \cdot m_f^3}{\rho_f^3} \cdot \left(\frac{1}{\not{V}_c^3} - \frac{1}{\not{V}_o^3} \right) \tag{2.16}$$

where K_{Wyk} is an undetermined dimensionless constant and $\not{V}_o$ is the initial volume of the fibres under no applied pressure.

For high fibre volume fractions, the fibres must be aligned with very small interfibre spacing. In 1985, Gutowski proposed a compaction model for lubricated, imperfectly aligned fibre stacks based on the deflection of fibre beams, creating an ever-increasing number of arches throughout the compaction cycle [47]. The number of arches grows exponentially, thus the resistance to compaction also increases exponentially. Later, Gutowski *et al.* proposed a model for the compaction of fibres in various states of applied stress [33, 48]. Equation 2.17 relates the applied compaction pressure to the fibre volume fraction for fibres which are not restricted in elongation:

$$P_p = \frac{3 \cdot \pi \cdot E_f}{\beta^4} \cdot \frac{\sqrt{\frac{v_o}{v_f}} - 1}{\left(\sqrt{\frac{v_{f,max}}{v_f}} - 1 \right)^4} \tag{2.17}$$

where P_p is the applied pressure from compaction platens, v_o is the initial fibre volume fraction for an unstressed bundle with the fibres touching, $v_{f,max}$ is the maximum available fibre volume fraction, and;

$$\beta = \frac{L}{a}$$

where L is the length of a volume element containing a representative fibre and a is the height of the curved fibre element contained the same volume element as defined through L. These are highlighted with a representative fibre diameter d_f in Figure 2.8.

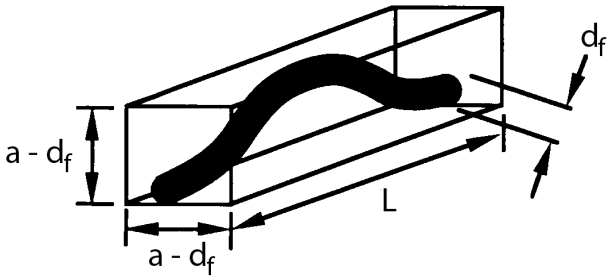

Figure 2.8: Representative fibre element [48]

Šimáček *et al.* formally derived the compaction pressure for bulk compression as Equation 2.18:

$$P_p = \frac{3 \cdot \pi \cdot E}{2 \cdot \beta^4} \cdot \frac{-\epsilon_B}{\left(\sqrt{\frac{v_{f,max}}{v_o \cdot (1 - \epsilon_B)^2}} - 1 \right)^4} \tag{2.18}$$

where ϵ_B is the bulk strain as defined in Equation 2.19:

$$\epsilon_B = \frac{1 - \frac{v_f}{v_o}}{2} \tag{2.19}$$

$$\epsilon_B = 1 - \sqrt{\frac{v_f}{v_o}} \tag{2.20}$$

Equation 2.20 is the infinitesimal strain used by Gutowski *et al.* to derive Equation 2.17; however, Šimáček *et al.* applied non-linear strain, Equation 2.19, due to the possibility of exceeding the limits for linear theory. Both expressions are similar and for typical compaction problems are "close enough from an engineering point of view" [49].

Typical experimental curves of pressure as a function of fibre volume fraction are displayed in Figure 2.9.

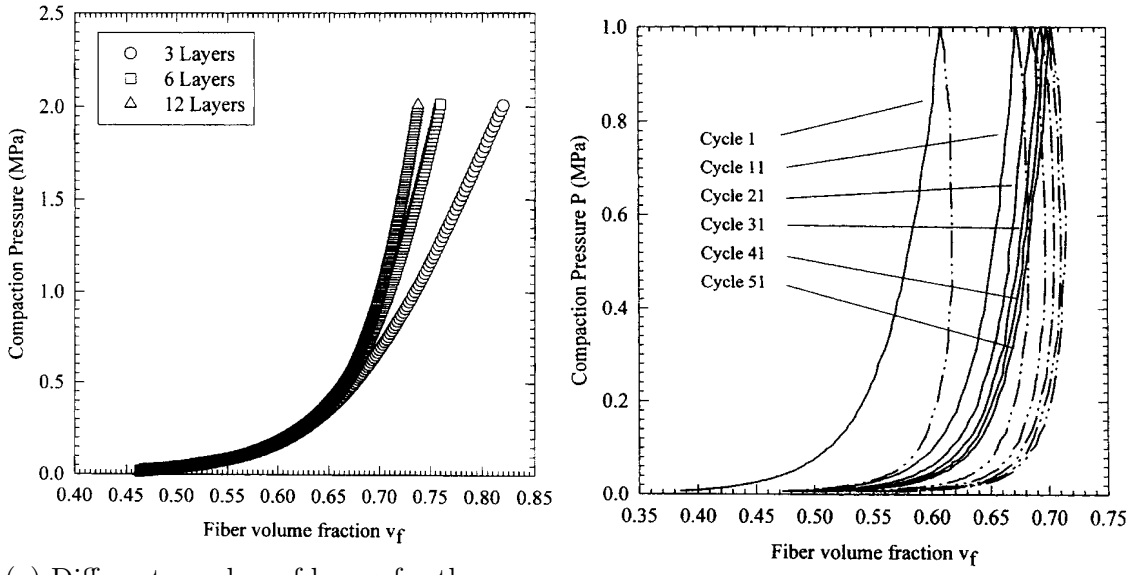

(a) Different number of layers for the same material [50]

(b) Repeated compaction cycles [51]

Figure 2.9: Pressure as a function of fibre volume fraction with different variables

As can be seen in the figures above, the pressure required for reaching a target fibre volume fraction depends on more parameters than those required for solving either Equation 2.16 or 2.17. Currently, empirical expressions are applied for modelling the compaction of reinforcements [51]. One of these sets of equations with widespread utilization correlates the fibre volume fraction to compaction pressure and the other correlates the current compaction pressure to the initially applied compaction pressure and elapsed time. Both Equations 2.21 and 2.22 require experimentally obtained constants [52],

$$v_f = A \cdot P_p^B \tag{2.21}$$

$$\frac{P_p}{P_{p,o}} = 1 - C \cdot t^{\left(\frac{1}{D}\right)} \tag{2.22}$$

where A is the fibre volume fraction for a compaction pressure P_p equal to 1 Pa, B is the compaction stiffening index, C is the pressure decay after 1 s, D is the relaxation index, and $P_{p,o}$ is the initially applied compaction pressure.

Compaction causes the fibre networks to reorganize in such a way that the uniformity of a given layer in a preform may improve significantly. This can be seen qualitatively in Figures 2.10 and 2.11. The figures are from an experiment conducted with 51 cycles of compaction at a constant maximum pressure of 1.0 MPa. The preform is a no-crimp roving with a 56.0% fibre volume fraction [51].

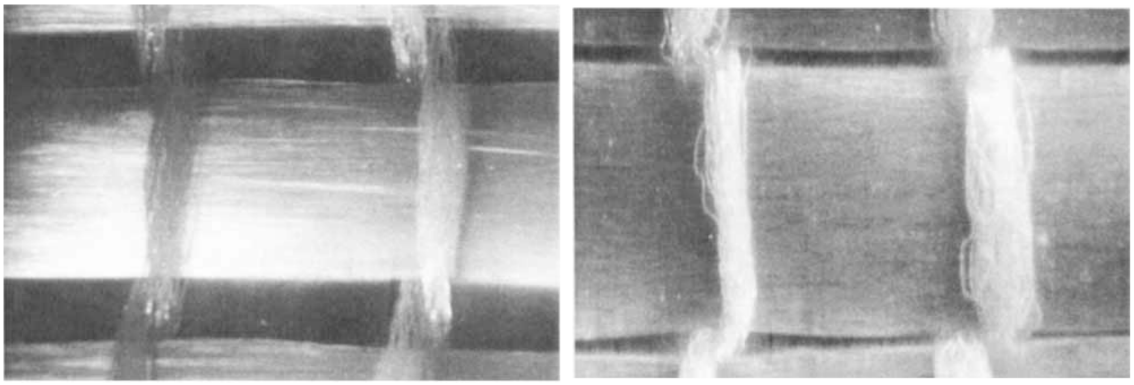

(a) Initial state (b) After 51 cycles of compaction

Figure 2.10: Effect of compaction on fibre reorganization for NCFs, 20x [51]

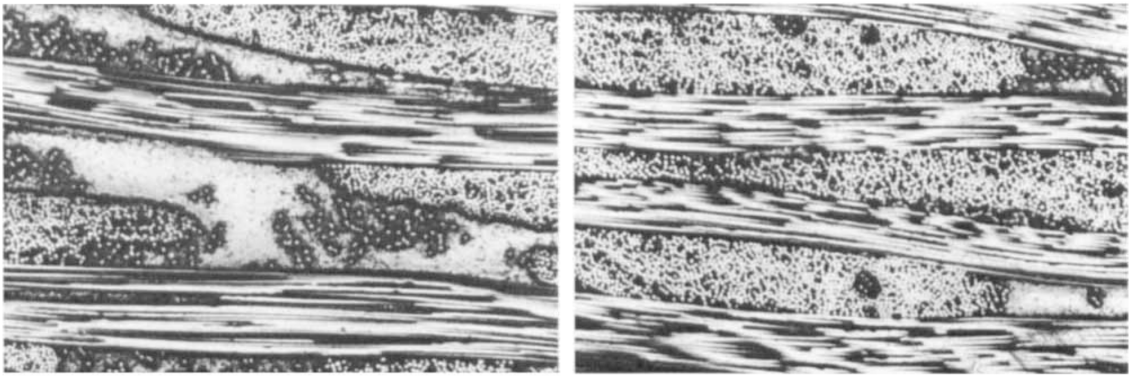

(a) Initial state (b) After 51 cycles of compaction

Figure 2.11: Effect of compaction on fibre reorganization for NCFs, 50x [51]

Figure 2.10 shows the fibres spreading to fill the interbundle spacing while appearing to simultaneously increase the uniformity of the yarn itself. Figure 2.11 shows a large reduction in resin rich zones, the white regions, resulting in a more uniform in-plane cross-section.

Chapter 3

Experimental setup and procedure

The experimental data required for solving for permeability using Darcy's law are time t, inlet gauge pressure P_o, flow rate q, and flow front position $r_f(x, y)$. Other data required for determining permeability values are preform and fluid specific, and such values remain constant throughout individual trials. These constants include the fibre volume fraction v_f, preform thickness h, and the dynamic viscosity of the permeating fluid μ.

Two different experimental apparatuses were used for recording these datum in different cases.

Rig 1: Mould with aluminium base, discussed in Section 3.1.2.1

Rig 2: Mould with polycarbonate base, discussed in Section 3.1.2.2

A brief overview of all experimental apparatuses and procedures conducted throughout all of this thesis' experiments is as follows. A closed cavity containing a preform was filled with oil under a constant flow rate. The fluid was initially contained in a hydraulic cylinder which was contracted at a constant speed using a screw driven Instron universal testing frame. Flow rate and pressure were recorded and correlated. The dynamics of impregnation were also observed. A more detailed description of the setup and procedure is provided in respective sections as follows.

Specifically, Section 3.1.1 provides information regarding specifications of the experimental apparatus which were common to all experiments. Section 3.1.2 details the individual

rig specifications; this section is subdivided into two subsections, one for each of the rigs. Section 3.1.3 details the materials which were used in the fabrication of preforms. Section 3.1.4 details the fluids and dyes used. Section 3.2.1 details the procedure for starting the experiment and obtaining data. Section 3.2.2 details the analysis of the raw data; this section is subdivided into five subsections, one subsection for preform, compaction, video, isotropic, and orthotropic related data analysis.

3.1 Experimental setup

3.1.1 Instruments common to all rigs

Elements of the experimental apparatus which were common to the majority or all trials are outlined in Figure 3.1.

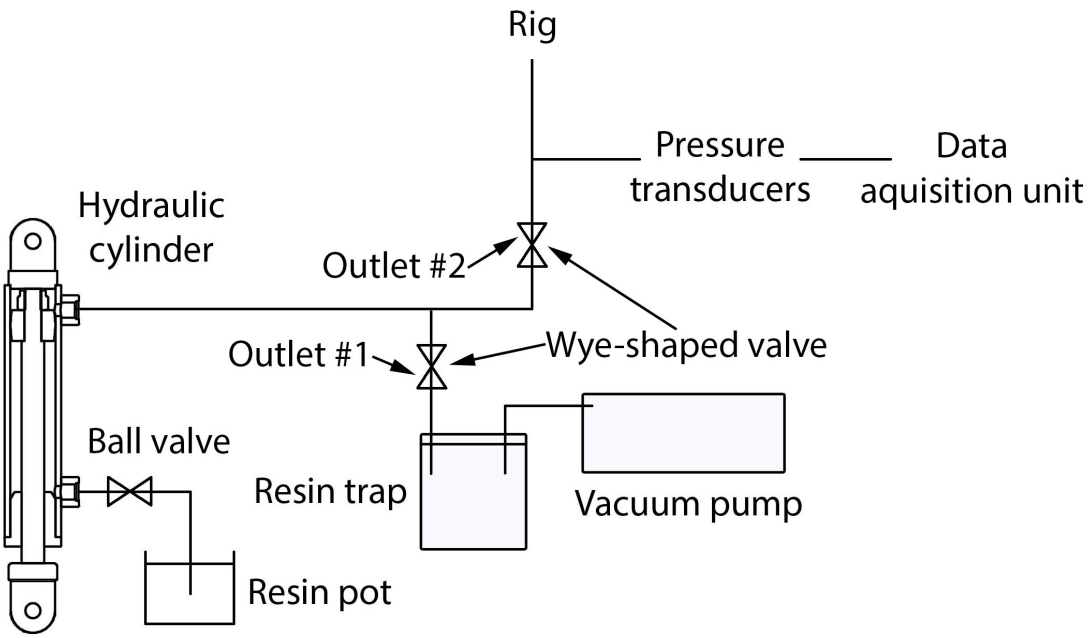

Figure 3.1: Diagram of the common elements

Fluid rested in a resin pot laid at the lowest point of the apparatus. The resin pot was open to atmosphere. With the resin pot filled with silicone oil or resin, the inlet of a piece of tubing was submerged. This tubing was high-pressure PVC tubing with a polyester braid embedded into its walls. The tubing had a maximum rated pressure of 1.9 MPa (275 psi) at 21°C (70°F). It had an internal diameter of 9.5 mm (3/8") and an outer diameter of 15.9 mm (5/8"). This type of tubing was used throughout the common apparatus.

The exit to this piece of tubing was a brass ball valve with a maximum rated pressure of 4.1 MPa (600 psi) at 38°C (100°F). The ball valve had two 1/2" NPT (national pipe thread) female connectors which were reduced to 1/4" NPT female connectors using a precision high-pressure brass male to female hex reducing bushing. These bushings were rated to a maximum 26.9 MPa (3900 psi) at 22°C (72°F).

To connect physically the tubing to the inlet of the valve a female and male quick disconnect tube coupling was used. The coupling size was 1/4" and the individual couplings were rated to a maximum pressure of 1.7 MPa (250 psi). The female quick disconnect had a barbed fitting designed to be used with 3/8" inner diameter tubing on the opposite end. With the hose fitted over the barb of the female quick disconnect, a worm-drive hose clamp with nonslip screw was tightened. The male quick disconnect had a 1/4" NPT thread on its opposite end. This NPT thread, and all threads in this system, were wrapped with pipe thread sealant tape. This tape had a thickness of 0.071 mm (0.0028") and was appropriate for the temperature range experienced in the laboratory. Typically three revolutions of the tape were made around the threads to ensure a tight seal. The male quick disconnect was fitted into the brass ball valve through the bushing and tightened by hand.

The exit to the ball valve was also connected to tubing using the same coupling system. The exit of this tubing was attached to the inlet of the hydraulic cylinder, again using the same coupling system. This Kinecor 30AGU08-ASAE hydraulic cylinder had an internal diameter of 76.2 mm (3.0") and a stroke length of 203.2 mm (8.0"). The maximum safe operating pressure of the cylinder was 17.2 MPa (2500 psi), well beyond the range of pressures in all testing performed [53]. The hydraulic cylinder had 3 ports, each of which had a 1/2" NPT female connector. One port was on the side of the piston opposite to the other two ports. This lone port was open to ambient conditions. The other two ports were reduced

from the 1/2" NPT female connector to a 1/4" NPT female connector using identical reducing bushing as the ball valve. The hydraulic cylinder was set into a 4482 screw driven Instron universal testing frame with a 100kN frame and 100kN load cell.

Tubing which exited the hydraulic cylinder was connected to a wye-shaped 3-port brass ball valve. The inlet of the valve had a 1" NPT female connection which was reduced to 1/4" NPT through a high-pressure stainless steel male to female hex reducing bushing which had a maximum pressure rating of 20.7 MPa (3000 psi) at 22°C (72°F). The outlets of the valve were two 3/4" NPT male connectors which were reduced to 1/4" NPT through a medium-pressure stainless steel female to female reducing coupling with a maximum pressure rating of 1.0 MPa (150 psi) at 22°C (72°F). The wye-shaped valve had a maximum pressure rating of 1.7 MPa (250 psi) at 93.3°C (200°F). This valve also had safety exhaust such that whenever a valve was closed, the outlet would be open to ambient conditions. Each outlet of the wye-shaped valve could be opened and closed independently using separate handles. With the female 1/4" NPT connections in place tubing could be connected using the coupling system previously described.

Outlet #1 of the wye-shaped valve was connected through tubing to a resin trap, as indicated in Figure 3.1. This resin trap had an inlet with a barbed fitting designed for use with 3/8" inner diameter tubing. Tubing placed over this barbed fitting was tightened using an identical hose clamp as used on the tubing attached to the barbed female quick disconnects. The resin trap had a bucket inside with a capacity of 3/4 L. The resin trap had two outlets, one of which had a safety ball valve which, when opened, allowed ambient air to enter. The other outlet was connected through vacuum rated tubing to a GAST Manufacturing DAA-V715A-EB vacuum pump capable of drawing a maximum vacuum of 0.97 atm (29.0" Hg). This pump had a continuous duty cycle and a 1/4 hp motor.

Outlet #2 of the wye-shaped valve was connected through tubing to a precision high-pressure brass cross, as indicated in Figure 3.1. The cross had a maximum pressure rating of 20.7 MPa (3000 psi) at 22°C (72°F). The cross had four 1/4" NPT female connectors. One of which connected the union through tubing to the outlet on the wye-shaped valve, one which connected the union through tubing to the specific rig, and two which connected the union to pressure transducers. The female NPT connectors which connected the union to

tubing were fitted with the same quick disconnect couplings as before while the pressure transducers were connected to the union directly from the pressure transducers 1/4" NPT male connectors. All of the tubing, connectors, couplings, and valves were sourced from McMaster-Carr.

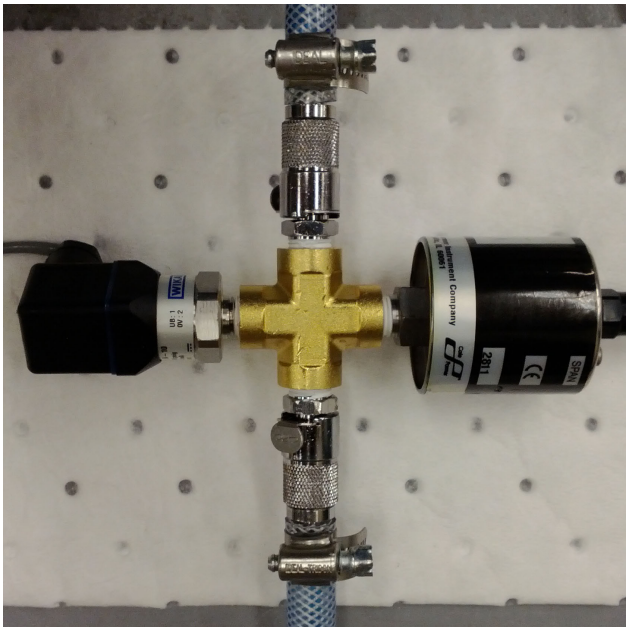

Figure 3.2: Brass cross with connections

One of the pressure transducers was a Setra Systems Model DPT 209 sourced from Cole-Parmer. It was accurate from 0 kPag to 689 kPag (0 psig to 100 psig). The other transducer was a Wika Tronic Industrial Pressure Transducer sourced from McMaster-Carr. It was accurate from 0 MPag to 2.07 MPag (0 psig to 300 psig). Both transducers were 2-wire systems outputting 4-20 mA current which was linearly correlated to their given pressure ranges. Both units were powered by a 12V power supply. They were calibrated by the manufacturers and the Wika transducer was supplied with a correction range to be applied to the linear curve. Using two transducers allowed higher accuracy in the 0-689 kPag range and continued recording in the rare instances when the pressures exceeded 689 kPag. Error as read from these transducers were ±0.13% full scale and ±0.5% full scale for the 689 kPag

and 2.07 MPag transducers, respectively. This results in overall errors of approximately 1.79 kPa (0.26 psi) and 20.7 kPa (3.0 psi), respectively.



(a) Setra 100psig (b) Wika 300psig

Figure 3.3: Different pressure transducers used

These pressure transducers were connected to a data acquisition unit (DAQ). The DAQ consisted of a computer equipped with LabView software version 8.2 and a National Instruments unshielded 68-pin I/O connector block (NI CB-68LPR). The circuit for both 2-wire systems required a resistor to be placed in between the positive and negative of the load monitor; a 100 ohm resistor was used for both transducers.

The other devices which recorded data were two different cameras. These two cameras were common to all of the rigs; however, the required usage of camera(s) were rig-dependent. Usage of the cameras will be discussed in the rig-specific sections. One of the cameras was a Canon Powershot S2 IS which had a maximum resolution of 2560 pixels by 1920 pixels in photography mode and a maximum resolution of 640 pixels by 480 pixels in movie mode. The movie mode captured images at 30 frames per second continuously for approximately 9 minutes. As a result of this limit, experiments which continued past the 9 minute interval had short time gaps in between subsequent video files. This was corrected using a digital

stopwatch with a maximum accuracy of 10 ms; procedure for the time correction between videos will be covered in Section 3.2.2. The other camera was a Nikon D7000 which had a maximum resolution of 4928 pixels by 3264 pixels in photography mode and a maximum resolution of 1920 pixels by 1080 pixels in movie mode. The D7000's movie mode captured images at a rate of 24 frames per second continuously for 20 minute intervals; a correction similar to the one mentioned before had to be made for experiments which continued past the 20 minute interval.

For trials where the preform was manufactured from carbon fibre, ultraviolet lights were used as the main light source. The ultraviolet lights used were two 15 watt Stanpro BLB compact fluorescent light bulbs which output light at wavelengths between 300 nm and 400 nm. The requirement for ultraviolet light use is explained in Section 3.1.4.

3.1.2 Instruments specific to each rig

3.1.2.1 Rig 1: Mould with aluminium base

The mould with aluminium base (Rig 1) consisted of an aluminium base, a translucent polycarbonate cover, steel plugs, spacers, steel braces, and one video camera. Briefly, the preform was centred on the aluminium base and surrounded by spacers corresponding to the desired final thickness of the preform. A polycarbonate cover was placed on top of the preform and spacers. Four steel braces were placed on top of the polycarbonate cover and the whole assembly was sandwiched together using grade 5 bolts. This assembly is displayed in Figure 3.4. Figure 3.5a shows a drawing of the aluminium base with dimensions outlined, whilst Figure 3.5 shows a photograph of the actual aluminium base.

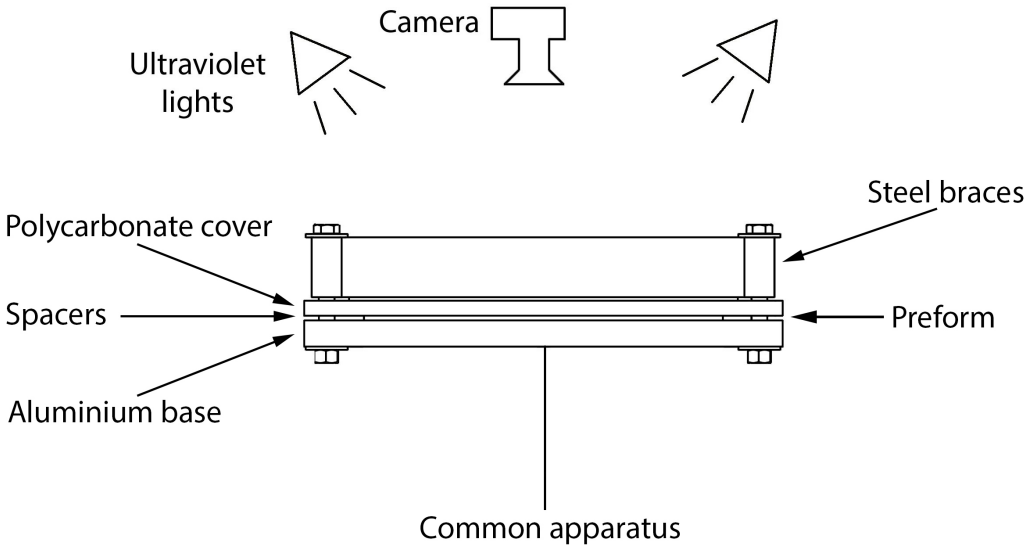

Figure 3.4: Diagram of the mould with aluminium base

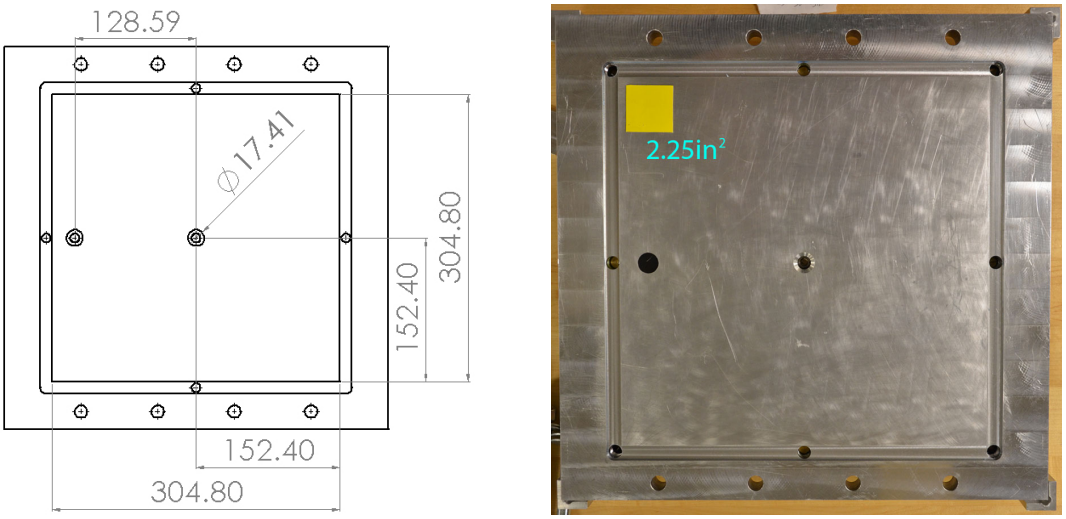

(a) Drawing with dimensions in mm

(b) Top view with an added paper size marker of 2.25 in^2

Figure 3.5: Aluminium base

The aluminium base measured 406.4 mm by 406.4 mm and had a thickness of 25.4 mm. The aluminium base had two inlet ports, one located in the centre and one located in the centre with respect to one axis while offset from the centre by 128.6 mm. The diameter of these ports was 11.1 mm, chamfered at a 45° angle which resulted in an inlet diameter of 17.4 mm in the platform surface. On the underside of the inlet ports was a ¼" NPT connector which was fitted with an identical male quick disconnect as previously described. This quick disconnect is the connection point between Rig 1 and the outlet of the common apparatus. Back on the top side of the aluminium base, two steel plugs had dimensions such that they created a flush surface to the platform when placed into the chamfered inlet ports. These steel plugs were used for closing one inlet port while the other was in use. Each inlet port had a unique plug. These plugs had undergone black oxide coating to prevent corrosion. A circumferential groove 3.3 mm deep and 12.7 mm wide was cut such that a 304.8 mm by 304.8 mm platform was created centred on the aluminium base. The groove served to collect fluid for easier removal. Four outlet ports with diameter 9.5 mm were centred along the perimeter of the groove. An additional four outlet ports with diameter 9.5 mm were created in the corners of the groove. Four holes with a diameter of 13.3 mm

and a centre to centre distance of 81.3 mm were cut on an axis parallel to, but offset by 19.1 mm, the aluminium base sides. A second line of holes was created on the opposite side of the aluminium base. These holes accommodated bolts used for sandwiching everything between the aluminium base and the steel braces.

Figure 3.6 displays a glass preform contained by the spacing elements along the periphery of the mould.

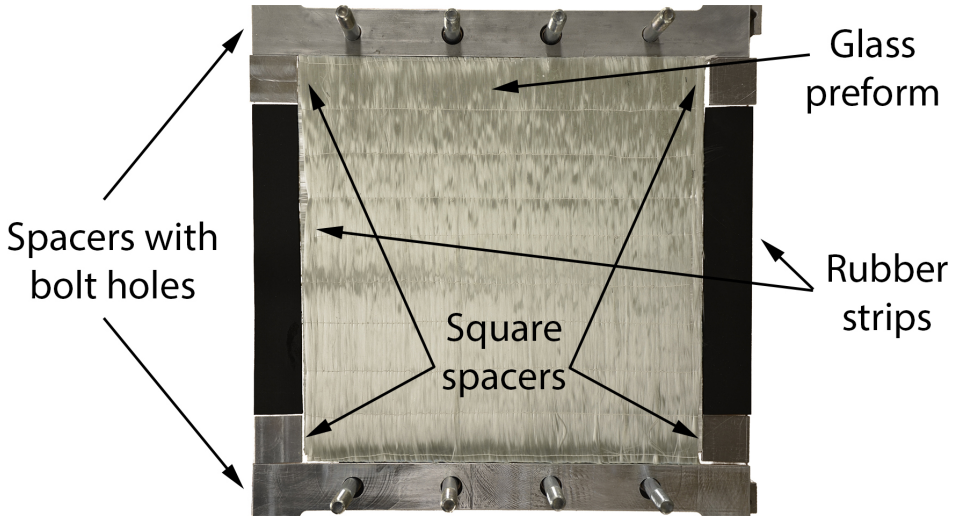

Figure 3.6: Top view of the mould with spacing elements highlighted

Pairs of spacers made from aluminium were placed atop the aluminium base in between the outer perimeter of the base and groove. These spacers had a width of 38.1 mm, a length of 406.4 mm, and ranged in thickness from 2.43 mm to 4.00 mm. They had holes with diameter 17.7 mm cut to match the bolt holes of the aluminium base. Two other aluminium spacers measuring 38.1 mm by 38.1 mm and two rubber strips measuring 254 mm by 38.1 mm, each ranging in thickness from 2.43 mm to 4.00 mm, were place along the sides of the aluminium base devoid of bolt holes. The rubber strips were used for reducing bending of the polycarbonate cover and minimize stress concentrations created between contact of the aluminium spacers and the polycarbonate cover. Appropriate spacers were chosen depending on the desired thickness of the preform in a given trial.

The polycarbonate cover placed on top of the spacers created a cavity. The polycarbonate cover had the same outer dimensions as the aluminium base other than the thickness which was reduced to 12.7 mm. The cover also had bolt holes matching those in the aluminium base and spacers. To reduce bending of the polycarbonate cover, 4 steel braces were used for sandwiching everything between the braces and aluminium base. These steel braces were 12.7 mm wide, 50.8 mm tall, and 406.4 mm long, and had also undergone black oxide coating. In between the four braces and the polycarbonate cover four corresponding rubber strips were laid to protect the surface of the cover from scratches. These strips were 12.7 mm wide, 3.2 mm thick, and 330.2 mm long.

Rig 1 was used for Trials 01 through 07. The Canon Powershot was used in Trials 01 through 05 while Trials 06 and 07 used the Nikon D7000 for recording video.

3.1.2.2 Rig 2: Mould with polycarbonate base

The mould with polycarbonate base (Rig 2) consisted of a translucent polycarbonate base, a translucent polycarbonate cover, spacers, steel braces, and two video cameras.

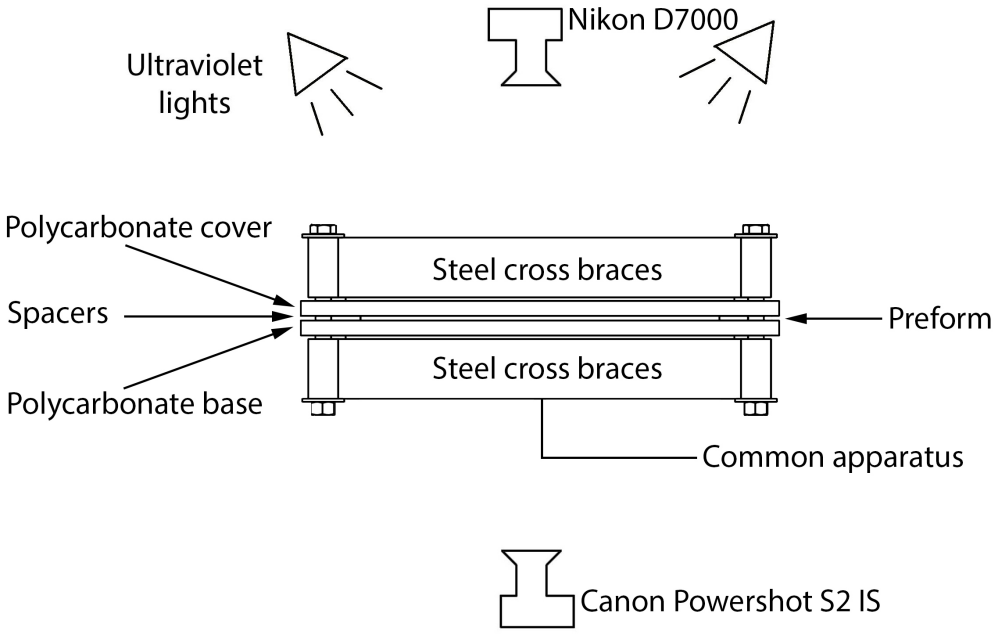

Figure 3.7: Diagram of the 2D mould with polycarbonate base

The polycarbonate base measured 406.4 mm by 406.4 mm and had a thickness of 12.7 mm. The polycarbonate base had one inlet port, located in the centre, with a diameter of 11.1 mm. On the underside of the inlet ports was a 1/4" NPT connector which was fitted with a male quick disconnect identical to those previously described. This quick disconnect is the connection point between Rig 2 and the common apparatus. This base had the same arrangement of bolt holes as the aluminium base of Rig 1.

Rig 2 used the same spacers, rubber strips and steel braces as Rig 1. A second set of steel braces and rubber strips were used for accommodating the polycarbonate base. The only difference between the two sets of steel braces was that the second set was 12.7 mm taller. The rubber spacers were also thicker at 6.4 mm.

Both cameras were required for recording video from the top and bottom of the injection. The Nikon D7000 was used for recording video on the injection port side of Trials 08 and 09 while the Canon Powershot was used for recording the opposite side. Trial 10 used the Nikon D7000 directed towards the polycarbonate plate with injection port. Still images taken from the video of Trial 08 are displayed in Figure 3.8.

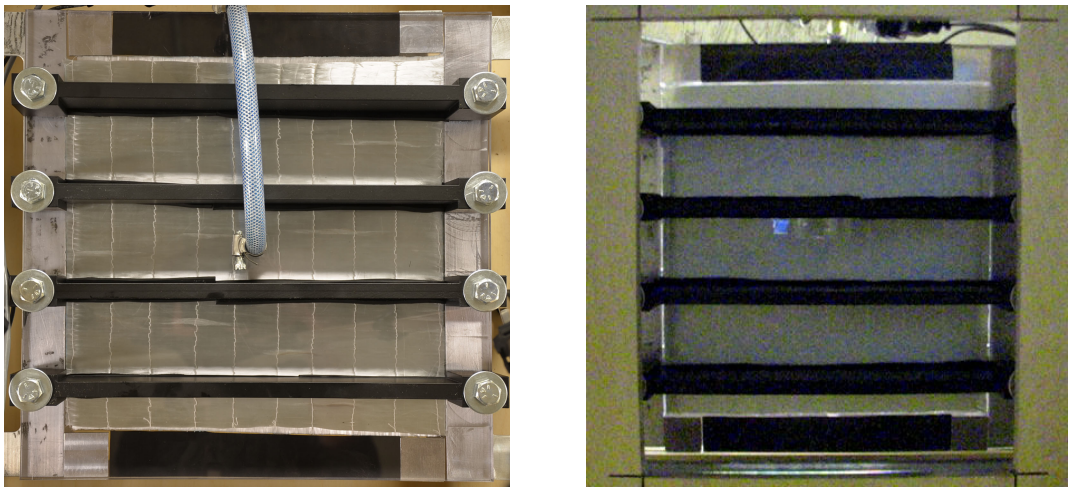

(a) Nikon D7000 directed at the polycarbonate plate with injection port

(b) Canon Powershot directed at the polycarbonate plate without injection port

Figure 3.8: Images of Trial 09 from both cameras, Rig 2

3.1.3 Preform materials

Two different types of fibres were used for manufacturing preforms used in all trials.

The first fibre was Owens Corning SE 1200 Type 30, 4400 Tex or 113 yield glass fibre. 4400 Tex implies that the linear density of the yarn is 4.4 $\frac{g}{m}$. The yarn also had a cross-sectional area of 1.676 mm^2 [4]. The number of layers depended on the desired preform thickness and fibre volume fraction. The number of layers in glass fibre preforms ranged from 4 to 7.

The second fibre used was Tenax-J grade HTS40 E13 12K, 800 Tex carbon fibre. This yarn had a linear density of 0.8 $\frac{g}{m}$. The yarn also had a cross sectional area of 0.462 mm^2. The number of layers of this carbon fibre in preforms also varied dependent on the desired

thickness and fibre volume fraction. The number of layers of carbon fibre in preforms ranged from 12 to 18.

The thread used to stitch the successive layers of fibre was standard commercial grade 100% polyester thread.

3.1.4 Fluids and dyes

Polydimethylsiloxane, or silicone oil, provided by Clearco Products Co., Inc., was used in place of epoxy in all of the trials. This substitution was done because silicone oil replicates the viscosity typical of epoxy resins while the silicone oil is much easier to handle, store, and clean. One parameter which was likely not constant between the two fluids was the surface tension. This difference would alter the effect of capillary action on the flow; however, this effect is small for flow under the imposed pressure gradients used for all of the trials. This oil had a dynamic viscosity of 500 cSt and a density of 971 $\frac{kg}{m^3}$ at room temperature, resulting in a dynamic viscosity of 485.5 $mPa \cdot s$. Another advantage of silicone oil is that its viscosity does not change significantly over a wide range of temperatures [54]. The epoxy which the silicone oil mimicked was Tri-Tex L-1911. This epoxy was designed to properly wet fibreglass, carbon fibre, and other similar fabrics. When properly mixed this epoxy had a typical uncured viscosity of between 200-300 $mPa \cdot s$ [6].



(a) 5 gallon container

(b) Properties sheet

Figure 3.9: Pure silicone oil

Different dying agents were mixed with the silicone oil depending on the preform material. For the trials which used preforms manufactured using glass fibre, Pylam Products Company, Inc. LX 6258 Pylakrome Bright Blue was used at a ratio of 0.5% by mass. For trials which used preforms manufactured using carbon fibre a different dying agent was required. This is because carbon fibre is black and opaque which results in typical dyeing agents being ineffective when trying to follow the flow front optically. Hence Stuers Epodye was used to better view the flow progression in the carbon fibre preforms. To activate the fluorescence, ultraviolet light was applied to the apparatus throughout the relevant trials. The EpoDye product is intended for use with epoxy; however, it did readily dissolve into the silicone oil and worked as intended. The amount of EpoDye added to one litre of silicone oil was approximately 5 grams as recommended in the preparation instructions. Both of these dyes

were added to the silicone oil at room temperature and mixed manually. These dyes were designed to have little effect on the properties of the fluid to which they are added.



(a) Pylam Dye (b) EpoDye

Figure 3.10: Different dyes used

3.2 Procedure

3.2.1 Experimental procedure

All of the hoses, fittings, and other common equipment were assembled as described in Section 3.1.1 and displayed in Figure 3.11. The hydraulic cylinder was securely attached to the Instron testing apparatus such that translation was limited to only the axis common with the stroke length of the cylinder.

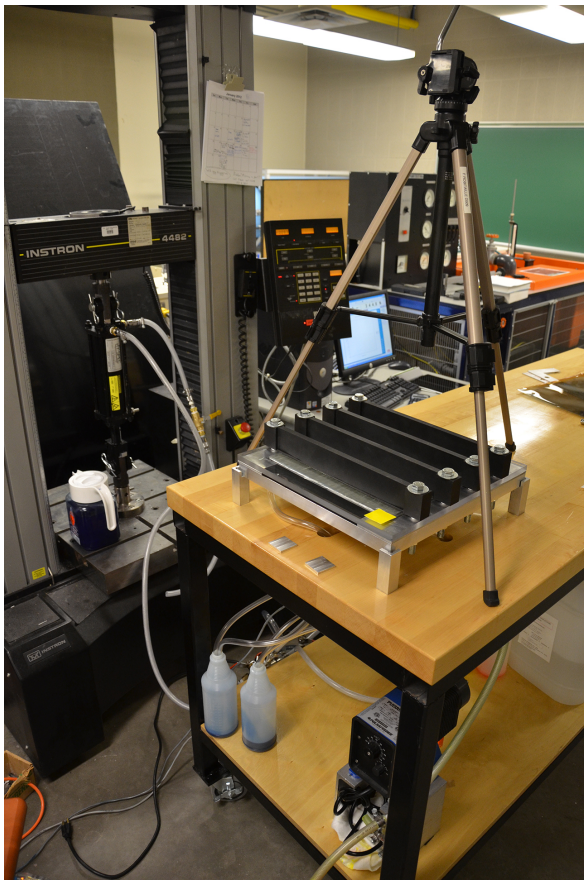

Figure 3.11: Experimental setup with Rig 1

A computer was used for controlling the Instron testing apparatus, specifically the Bluehill 2 software was used. The settings for the software included a compressive testing envi-

ronment with a maximum compressive load of 5.5 kN corresponding to a maximum operating pressure of approximately 1 MPa (145 PSI) and a constant compressive displacement rate satisfying the desired flow rate. This compressive displacement rate was calculated from the desired flow rate using the following equations:

$$\not{V}_{cylinder} = \frac{\pi}{4} \cdot D_{cylinder}^2 \cdot (H_{cylinder} - h_{cylinder}) \tag{3.1}$$

$$E_{rate} = \frac{dh_{cylinder}}{dt} \tag{3.2}$$

$$q = -\frac{d\not{V}_{cylinder}}{dt} = -\frac{d\not{V}_{cylinder}}{dh_{cylinder}} \cdot \frac{dh_{cylinder}}{dt} \tag{3.3}$$

$$q = \frac{\pi}{4} \cdot D_{cylinder}^2 \cdot E_{rate} \tag{3.4}$$

where $\not{V}_{cylinder}$ is the internal volume of the hydraulic cylinder, $D_{cylinder}$ is the internal diameter of the hydraulic cylinder, $H_{cylinder}$ is the stroke of the hydraulic cylinder, $h_{cylinder}$ is the amount by which the cylinder has been closed by the piston, and E_{rate} is the compressive displacement rate.

The same hydraulic cylinder was used for all of the trials, and the dimensions have been described previously in Section 3.1.1.

Many of the trials were conducted with a desired flow rate of either 0.100 $\frac{cm^3}{s}$ or 1.00 $\frac{cm^3}{s}$. Applying Equation 3.4 results in compressive displacement rates of 1.32 $\frac{mm}{min}$ and 13.2 $\frac{mm}{min}$, respectively.

For $q = 0.100\ \frac{cm^3}{s} = 6.00 \cdot 10^3\ \frac{mm^3}{min}$

$$E_{rate} = \frac{4 \cdot q}{\pi \cdot D_{cylinder}^2}$$

$$E_{rate} = \frac{4 \cdot 6.00 \cdot 10^3\ \frac{mm^3}{min}}{\pi \cdot (76.2\ mm)^2}$$

$$E_{rate} = 1.31568\ \frac{mm}{min}$$

$$E_{rate} = 1.32\ \frac{mm}{min}$$

For $q = 1.00\ \frac{cm^3}{s} = 6.00 \cdot 10^4\ \frac{mm^3}{min}$

$$E_{rate} = \frac{4 \cdot q}{\pi \cdot D_{cylinder}^2}$$

$$E_{rate} = \frac{4 \cdot 6.00 \cdot 10^4\ \frac{mm^3}{min}}{\pi \cdot (76.2\ mm)^2}$$

$$E_{rate} = 13.1568\ \frac{mm}{min}$$

$$E_{rate} = 13.2\ \frac{mm}{min}$$

For Rig 1 the steel plug was inserted into the chamfered injection port which was not used in the trials. Otherwise, the following procedure applies for both Rig 1 and Rig 2.

The preform was then placed into the rig cavity; attempts were made at keeping the injection port in between two stitch lines so that the effects of stitching would be reduced. The rig was then bolted securely with enough preload on the bolts to compensate for fluid pressure. Without any preload the cavity thickness would be more prone to increasing due to fluid pressure, changing the fibre volume fraction or creating channels above or below the preform for the fluid to travel preferentially.

With the preform and all physical connections between the common apparatus and rig-specific apparatus in place, the actual trial could begin. With all of the valves open, the Instron testing apparatus was used for extending fully the hydraulic cylinder. Safety sensors were adjusted such that the Instron testing apparatus would stop should travel reach the stroke of the hydraulic cylinder.

The safety exhaust on the resin trap, the ball valve, and outlet #2 of the wye-shaped valve were then closed. Outlet #1 of the wye-shaped valve was left open and the vacuum pump was turned on. Then the pump was allowed to reach steady state at its maximum pressure differential of 0.97 atm, Figure 3.12 displays the readout of the vacuum pump after it had reached steady state. This vacuum was typically drawn in less than a minute. Fitting

seals were tested by turning the vacuum pump off and reading the pressure gauge; if the pressure reading did not change significantly then the trial would proceed, but if the reading changed quickly then the fittings were removed and resealed.

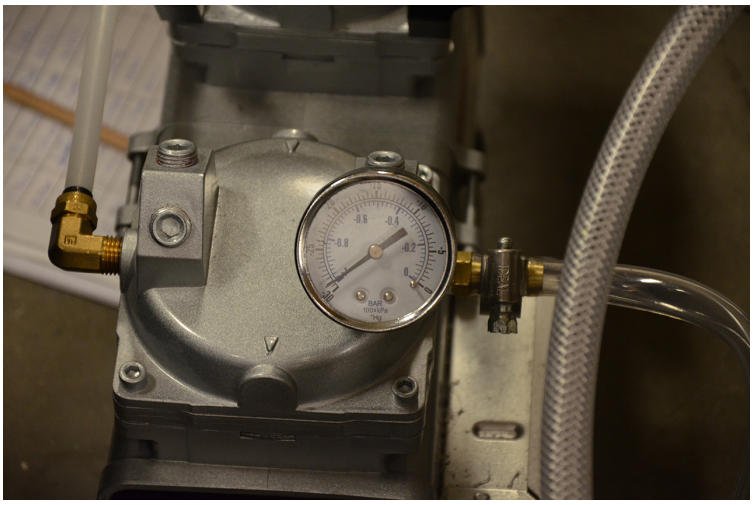

Figure 3.12: Vacuum pump readout at steady state

If the fittings were airtight then the vacuum pump was turned on again and the ball valve was opened to allow fluid to fill the tubing completely. This was done until fluid reached the hydraulic cylinder. The ball valve was then closed allowing the vacuum pump to stabilize. Care was taken in making sure that the tubing in the resin pot was always completely submerged so that no air could enter the system. When the vacuum pump had stabilized the ball valve was opened again, this time allowing fluid to fill the hydraulic cylinder and all tubing completely, up to the wye-shaped valve. Filling of the cylinder is displayed in Figure 3.13. Once fluid had begun accumulating in the resin trap the ball valve was closed. The vacuum pump was typically left on for a short while until very little fluid was seen entering the resin trap. At this point outlet #2 of the wye-shaped valve was closed and the vacuum pump was turned off. The safety exhaust attached to the resin trap was opened for removing the vacuum in the tubing downstream of outlet #2.



Figure 3.13: Filling of the hydraulic cylinder

With the system primed with fluid, the DAQ computer was turned on and the LabView software initialized such that pressure data collection was continuous. Video recording was turned on for rigs where video information was required. The time as indicated by the DAQ was recorded with the camera so that a correlation between time in the video and data collected by the DAQ could be established. The delay lapsed between turning on the video recording and the next step was kept as short as possible to minimize the likelihood of the video time limits having an adverse effect.

Outlet #2 was opened and the Bluehill 2 software used for quickly launching the Instron's compressive routine. The delay lapsed between the opening of the outlet and start of the program was kept small to minimize any ingress of air into the cylinder. The outlet was opened prior to the Bluehill 2 program being run to avoid pressurizing the fluid in the system, which could cause unnecessary stops due to the safety pressure limit being reached. Again, video recording was used for capturing either the time or the extension of the Bluehill 2 software to make a correlation between time in the video and data collected by the Bluehill 2 software.

The cameras were then placed in their respective positions when required. While the length tubing between the common apparatus and the specific rigs was kept as short as possible, the small flow rate allowed ample time to position the cameras properly and view

the entire filling process. The digital stopwatch was turned on and placed on the periphery of the mould as to be recorded by the video camera but not obstruct its view of the filling. The digital stop watch was was used for either correlating time between successive video files and/or correlating time between two different cameras.

Once the fluid had reached the edge of the groove closest to the injection port the trial was concluded because of a change in boundary conditions. The Bluehill 2 software was stopped and data exported; the same was done for the LabView software. The outlet #1 was opened to return fluid pressure in the lines back to atmospheric.

3.2.2 Data analysis

3.2.2.1 Preform data analysis

The area of the preform was measured for determining if there was any change in geometry at the scale of the full preform. Preform area was measured pre-compaction and post-compaction using Adobe Photoshop CS6. This was done by comparing the preform selected using software functions, to a selected reference marker, in the majority of cases a yellow square with an area of $1.45 \cdot 10^{-3}$ m^2 (2.25 $inch^2$), Figures 3.14a and 3.14b.

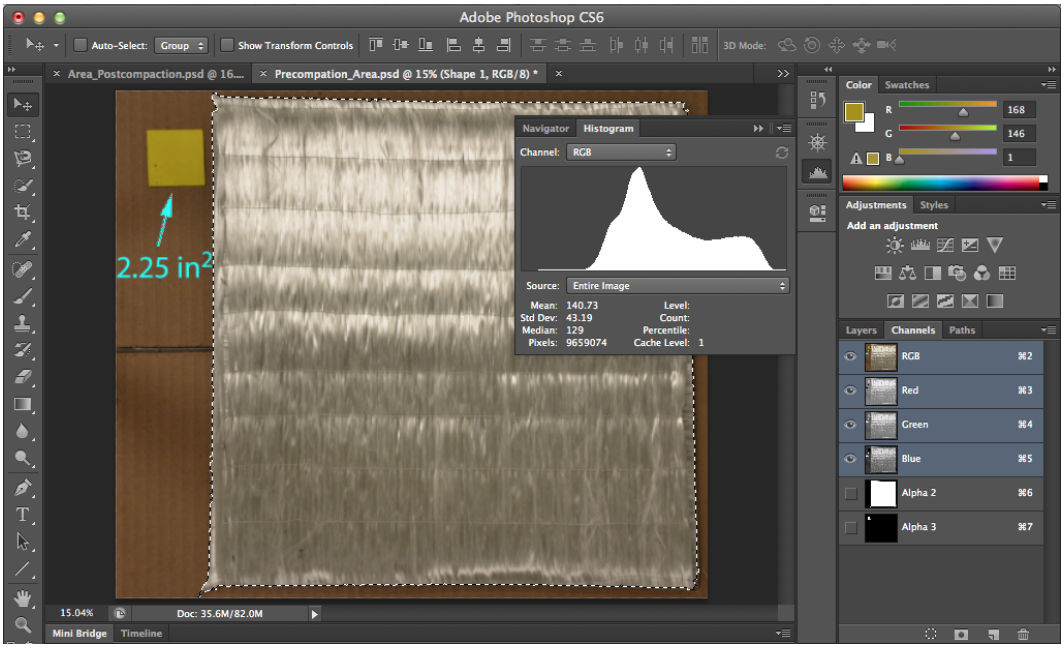

(a) Preform and marker with preform selected and associated pixel count

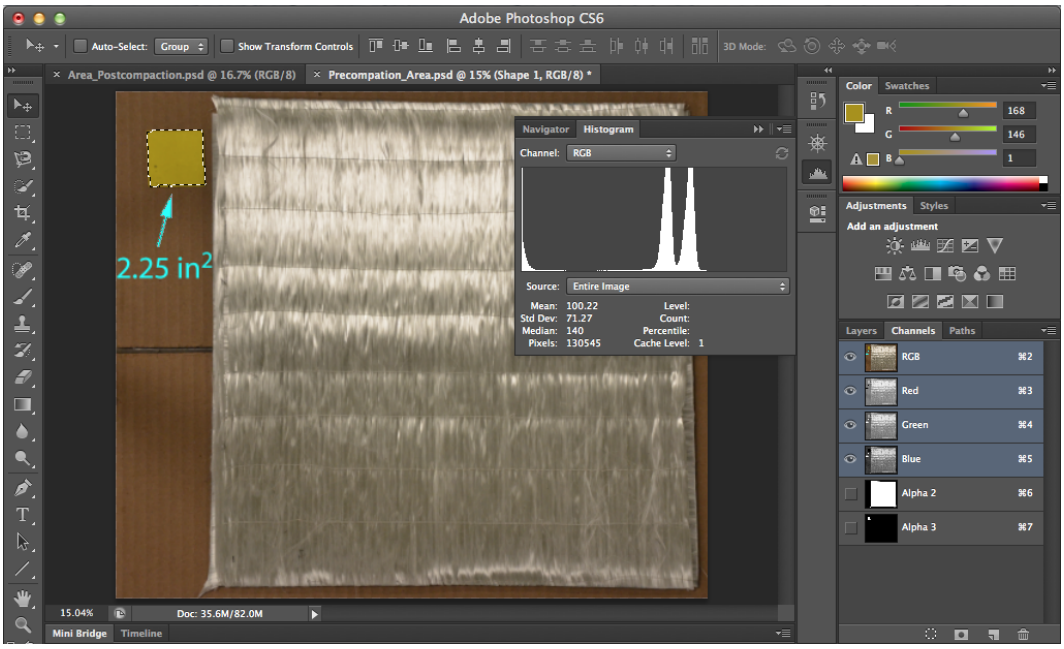

(b) Preform and marker with marker selected and associated pixel count

Figure 3.14: Pre-compaction preform area, Trial 08

Preform area could be determined from the area of the reference marker and Equation 3.5:

$$A_{preform} = \frac{N_{\substack{preform \\ pixels}}}{N_{\substack{marker \\ pixels}}} \cdot A_{marker} \tag{3.5}$$

where $A_{preform}$ is the preform area, $N_{\substack{preform \\ pixels}}$ is the number of pixels in the preform selection, $N_{\substack{marker \\ pixels}}$ is the number of pixels in the reference marker selection, and A_{marker} is the area of the reference marker.

For the example shown in Figure 3.14 Equation 3.5 becomes:

$$A_{preform} = \frac{9659074}{130545} \cdot 1.45 \cdot 10^{-3}\ m^2$$

$$A_{preform} = 0.107\ m^2$$

These values were not critical in the calculation of permeability and some trials did not have any accurate preform area data. This parameter was calculated solely to determine if there was any significant change which would have ramifications on the preform.

This process was done for both the pre-compaction and post-compaction areas; these could be compared using the relative difference equation:

$$d_r = \frac{|A_{preform}^{post-compaction} - A_{preform}^{pre-compaction}|}{\left(\frac{|A_{preform}^{post-compaction} + A_{preform}^{pre-compaction}|}{2}\right)} \tag{3.6}$$

where d_r is the relative difference in area.

3.2.2.2 Compaction related data analysis

Fibre volume fraction as a function of compaction pressure was used for comparing different trials. The data for determining fibre volume fraction and compaction pressure were displacement and load which the Instron testing apparatus output.

A correction to the displacement data which the compaction testing apparatus output was required due to strain in the compaction testing apparatus. This was done by performing

a single cycle of the compaction test without a preform being present between the compaction plates. The instantaneous corrected thickness of the preform can be determined from the data by applying Equation 3.7:

$$h_i = H_o - C_i \tag{3.7}$$

where h_i is the instantaneous corrected thickness of the preform, H_o is the instantaneous spacing between the compaction platens and C_i is the instantaneous correction to the displacement.

Rearranging Equation 1.4 and applying the instantaneous corrected thickness of the preform results in:

$$v_f\left(h_i\right) = \frac{A_f \cdot N_L}{s_y \cdot h_i} \tag{3.8}$$

The compaction pressure applied on the preform can be calculated from Equation 3.9:

$$P_p = \frac{F_{Instron}}{A_{preform}} \tag{3.9}$$

where $F_{Instron}$ is the force recording from the Instron testing apparatus.

As previously shown in literature, the amount by which the fibre volume fraction increases after successive cycles decreases significantly after many repeated cycles. 35 cycles of compaction were performed on all of the preforms which were compacted. Also, the compressive displacement rate was kept constant for all of the trials at 0.5 $\frac{mm}{min}$. An example of the corrected compaction data from Trial 08 is shown in Figure 3.15:

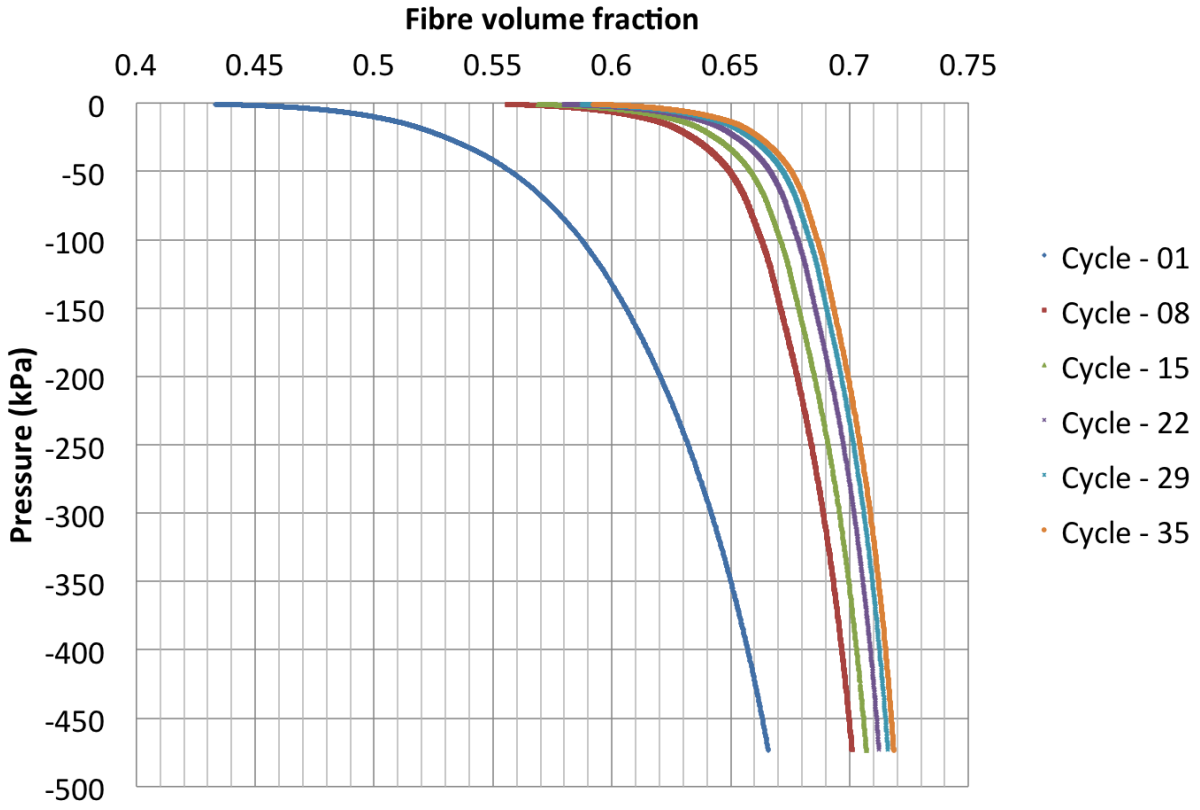

Figure 3.15: v_f as a function of P_p, Trial 08

3.2.2.3 Video data analysis

A process comparable to the analysis of area described in Section 3.2.2.1 was performed for analyzing the flow front. In this case Adobe Photoshop CS6 was used for comparing the maximum progression of the flow fronts, in both principal directions, to a reference length. The maximum length of the flow front from the injection port was taken as the maximum length along one principal direction, regardless of position on the other principal direction. The reference length changed from trial to trial; however, it was typically the distance from outlet groove edge to opposing outlet groove edge, approximately 330.2 mm (13.0").

First, video recording was launched using BS.Player software and several image stills from the video were saved with a file name corresponding to their respective video time

signature. Attempts were made at ensuring that the flow front progression had clear maxima; for example, images where the maximum flow front progression was obscured by the steel braces were not saved. All of these images were opened using Adobe Photoshop CS6 into a single file with a unique layer per still image. The file size was adjusted to correspond with the reference length such that the ruler tool could be used without any further corrections. The corrected ruler and image are displayed in Figure 3.16:

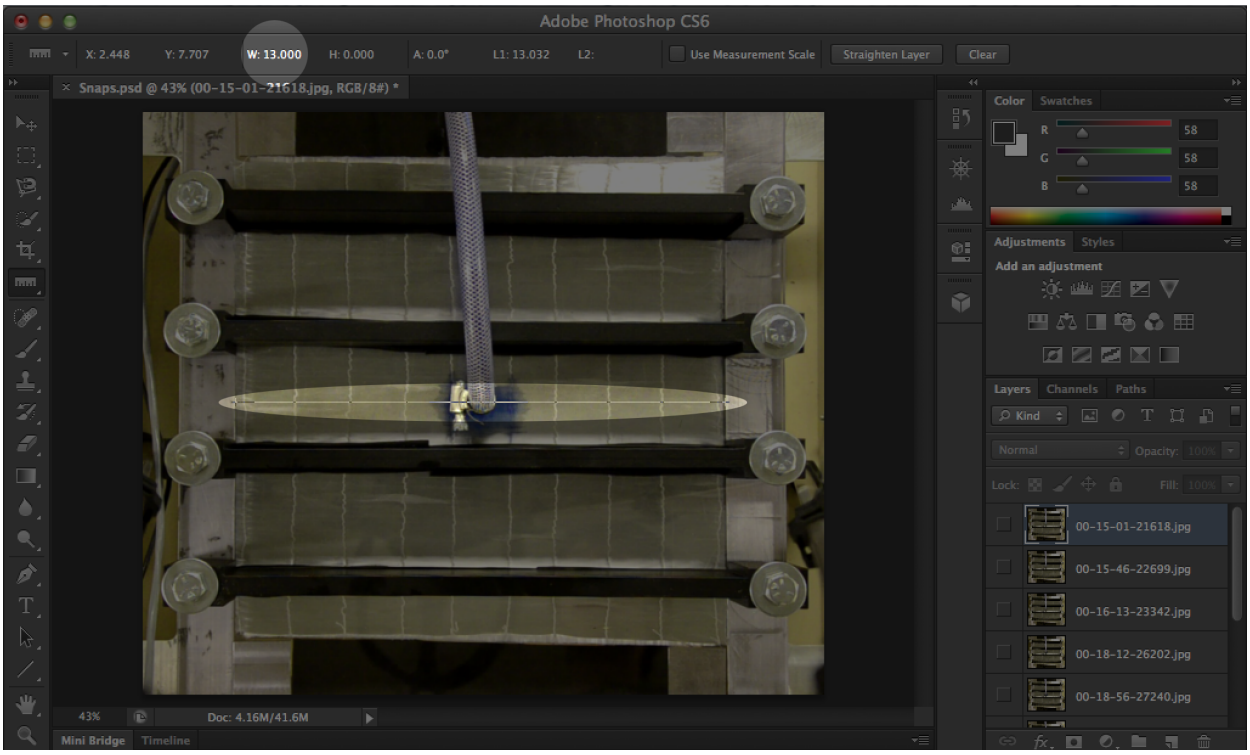

Figure 3.16: Image size with reference ruler highlighted, Trial 08

Using the ruler tool, measurements in both major axes were made, recorded in Excel, and correlated with their respective times. For most measurements the maximum flow front diameter was recorded then divided by two to obtain the maximum flow front radius. This was done to average the values between the two flow fronts if they progressed at slightly different rates. Furthermore, some trials had an axis partially obscured by the injection line hence a clear maxima was not distinguishable which made measuring the flow front diameter

inaccurate. In this situation radius measurements were taken from the centre of the injection port to the maximum distance of the visible flow front. The error which is introduced for this measurement is difficult to quantify because the exact position of the flow front is not always extremely evident. Examples of these two cases are displayed in Figures 3.17a and 3.17b.

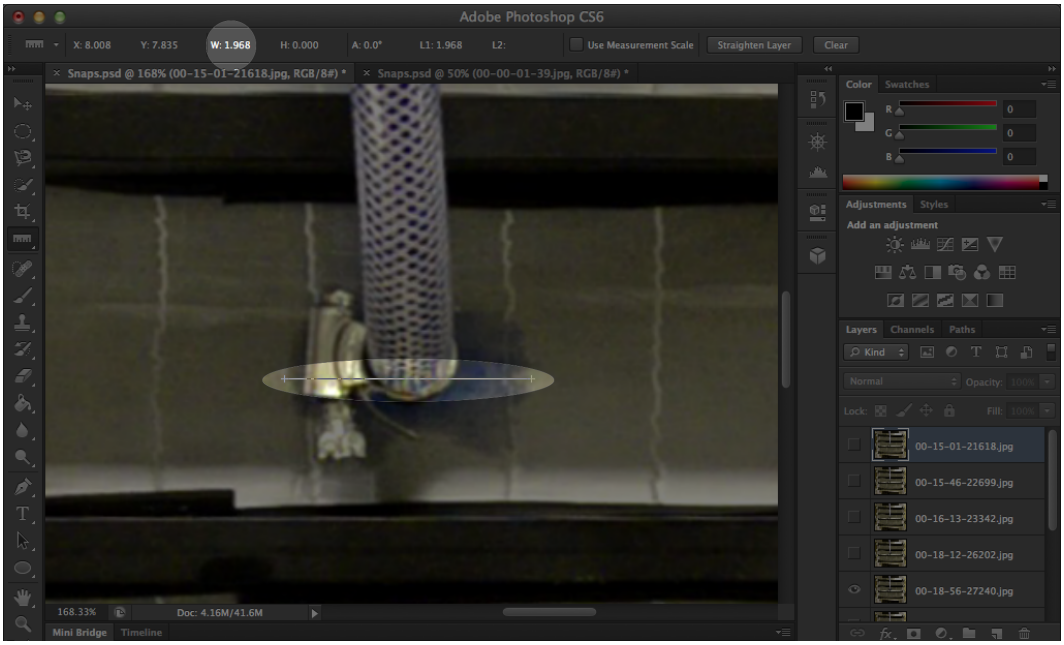

(a) Diameter measurement highlighted

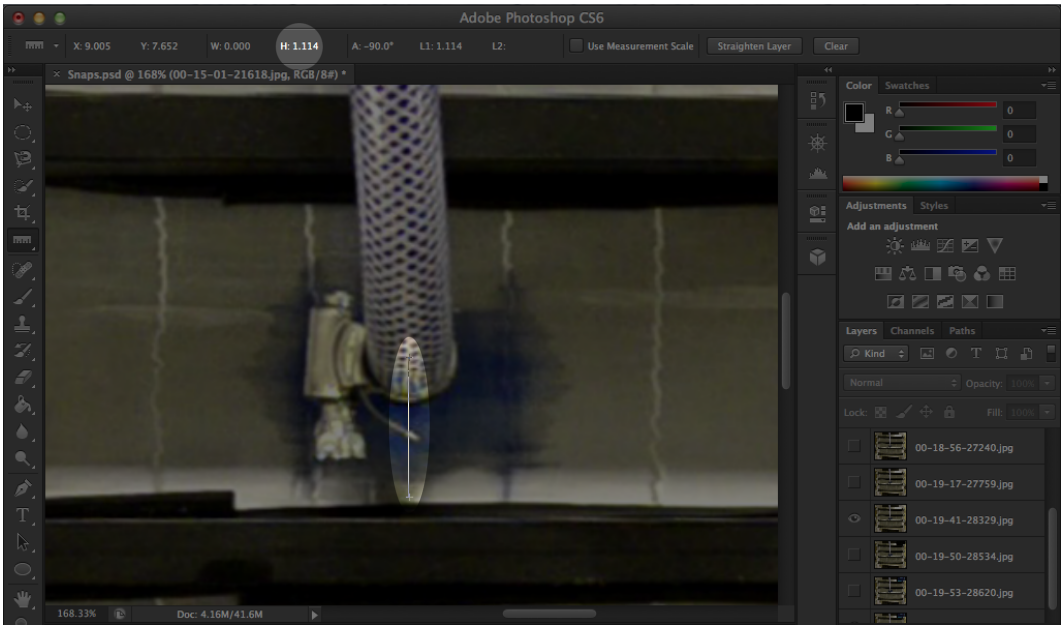

(b) Radial measurement highlighted

Figure 3.17: Measurement of the maximum flow front distance along major axes, Trial 08

3.2.2.4 Isotropic case

When the flow front progression closely matched the scenario displayed in Figure 2.2a, then the isotropic equations could be applied for determining a single value of permeability. The isotropic permeability can be calculated explicitly from Equation 3.11 which is obtained by substituting mass conservation, Equation A.1, into the isotropic Darcy's law, Equation A.2. The only variables to the permeability equation are inlet gauge pressure and time, both of which are provided by the DAQ. No quantitative data was required from the video camera(s).

$$r_f = \sqrt{\frac{q \cdot t}{\pi \cdot h \cdot \epsilon} + r_o^2} \tag{3.10}$$

$$K\left(P_o, t\right) = \frac{q \cdot \mu}{2\pi \cdot h \cdot P_o} \cdot \ln\left(\frac{\sqrt{\frac{q \cdot t}{\pi \cdot h \cdot \epsilon} + r_o^2}}{r_o}\right) \tag{3.11}$$

The permeability values were averaged hence a standard error of the mean calculation was performed using Equation 3.13.

$$s = \sqrt{\frac{1}{N-1}\sum_{i=1}^{N}\left(K_i - \overline{K}\right)^2} \tag{3.12}$$

$$SE_{\overline{K}} = \frac{s}{\sqrt{N}} \tag{3.13}$$

where s is the sample standard deviation, N is the number of data points over which the permeability values are averaged, K_i is the instantaneous permeability, and $\overline{K}$ is the averaged permeability.

3.2.2.5 Orthotropic case

When the flow front progression closely matched the scenario displayed in Figure 2.2b, then the orthotropic equations were applied to determine the components of the in-plane permeability tensor. The method is as follows.

This example is for a sample data set taken from Trial 08. The data set is displayed in Table 3.1:

Table 3.1: Sample data set with radii determined from injection side camera, Trial 08

Time [s]	Flow front radius, r_x [m]	Flow front radius, r_y [m]	Inlet gauge pressure [kPa]
000.0	0.00555	0.00555	000.0
236.4	0.02136	0.02502	351.9
281.8	0.02847	0.03376	556.8
300.0	0.03000	0.04473	624.2
307.5	0.03790	0.05027	639.2
338.2	0.05354	0.07357	658.1
349.5	0.05428	0.08232	653.4
384.7	0.05738	0.10235	651.3
421.4	0.06083	0.11364	645.8
428.8	0.06229	0.11929	644.7
434.0	0.06284	0.12056	644.3
439.7	0.06339	0.12294	644.0

First, the slope from the flow front position r_y as a function of r_x is calculated. An example of this plot and corresponding trend line is shown in Figure 3.18. The line defined by the slope m_1 is forced to pass through the origin.

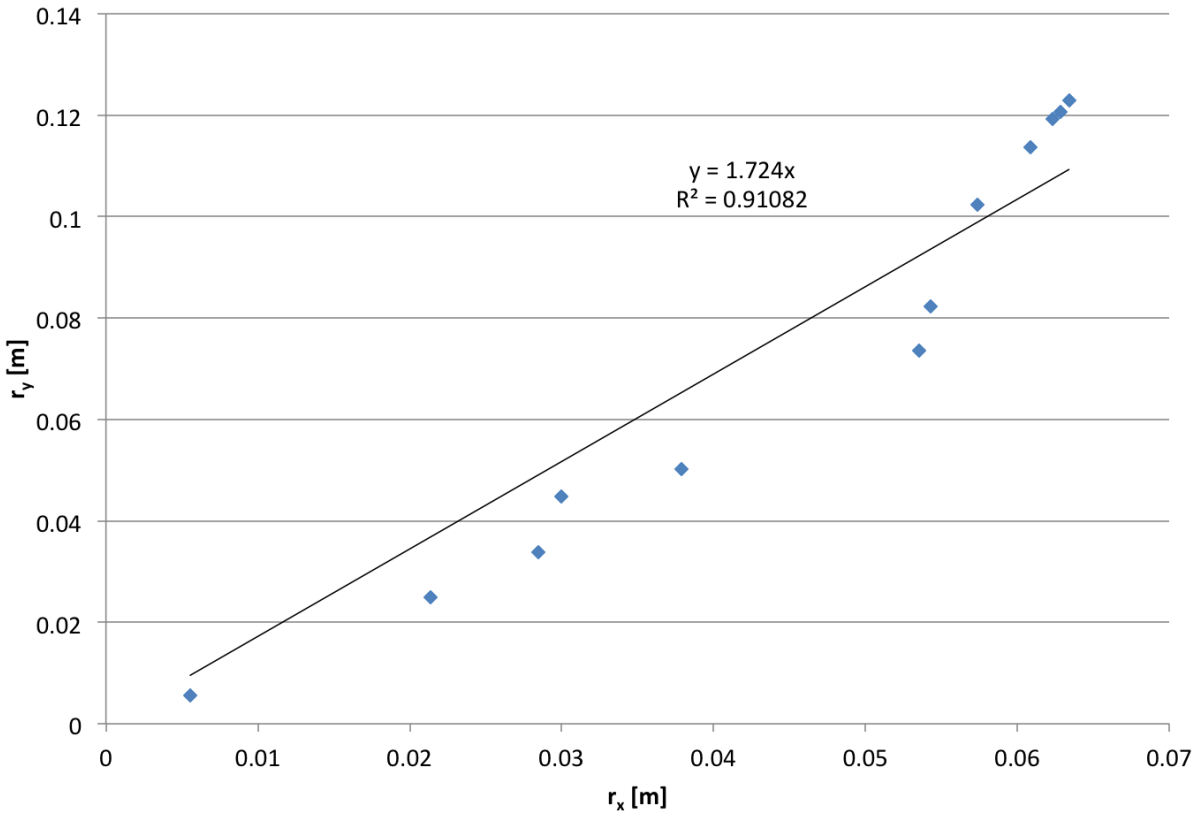

Figure 3.18: Flow front position along the principal axes, Trial 08

With $m_1 = 1.724$, Equation 3.14 can be applied for determining the radius in an equivalent isotropic system (EIS) r_{xe}, as follows:

$$r_{xe} = \sqrt{m_1} \cdot r_x \tag{3.14}$$

$$r_{xe} = \sqrt{1.724} \cdot 0.0634\ m \tag{3.15}$$

$$r_{xe} = 0.08324\ m \tag{3.16}$$

The natural logarithm of these r_{xe} values is then plotted as a function of corresponding inlet gauge pressures. Discrete values for this example are tabulated in Table 3.3 and plotted in Figure 3.3.

Table 3.2: Flow front radius and corresponding EIS radius

Flow front radius, r_x [m]	Radius in EIS, r_{xe} [m]
0.00555	0.00729
0.02136	0.02805
0.02847	0.03739
0.03000	0.03939
0.03790	0.04976
0.05354	0.07030
0.05428	0.07127
0.05738	0.07534
0.06083	0.07987
0.06229	0.08179
0.06284	0.08251
0.06339	0.08323

Table 3.3: Natural logarithm of the EIS radius and corresponding inlet gauge pressure

Natural logarithm of radius in EIS, $\ln(r_{xe})$	Inlet gauge pressure, P_o [kPa]
-4.9216	000.0
-3.5739	351.9
-3.2865	556.8
-3.2343	624.2
-3.0006	639.2
-2.6550	658.1
-2.6413	653.4
-2.5858	651.3
-2.5273	645.8
-2.5036	644.7
-2.4949	644.3
-2.4862	644.0

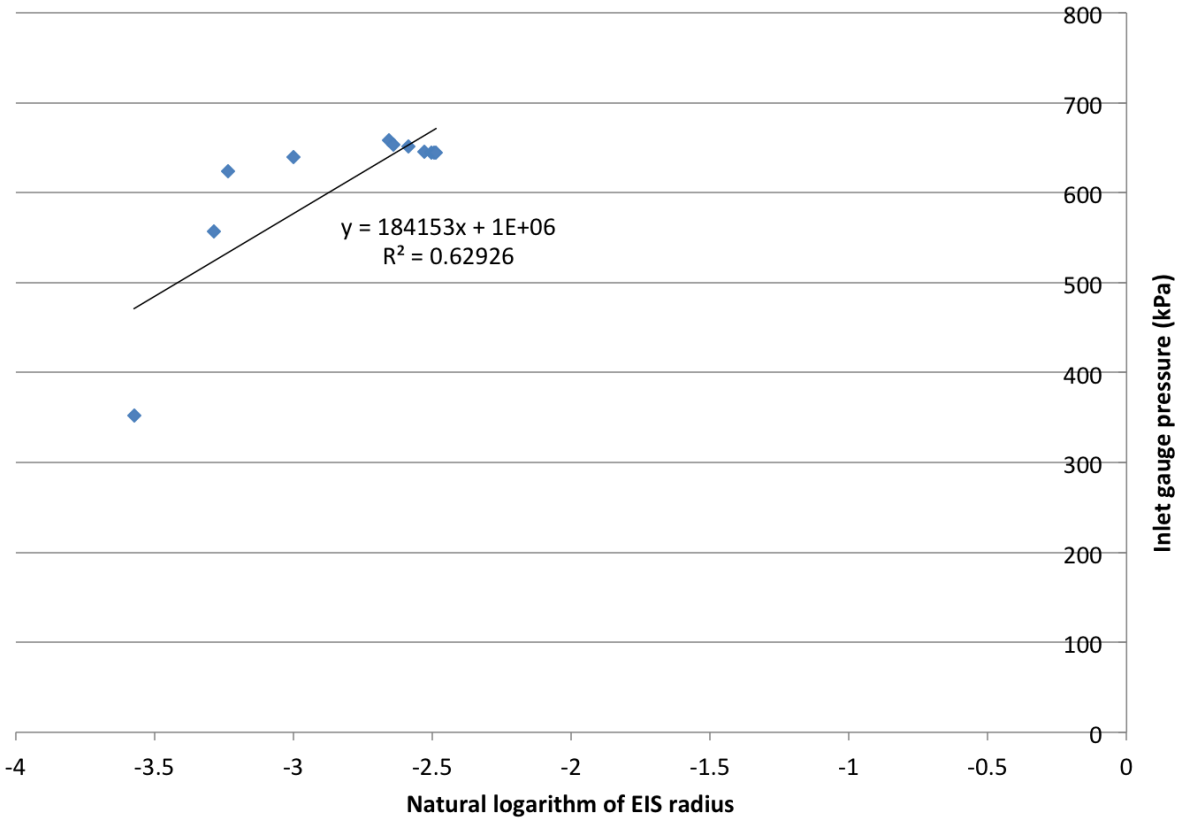

Figure 3.19: Inlet gauge pressure as a function of the natural logarithm of EIS radius, Trial 08

Permeability in an isotropic system is linearly correlated to constant values divided by the inlet gauge pressure divided by the natural logarithm of the radial flow front divided by the inlet radius [26]; hence, the slope of the linear curve fitted to the data set from Table 3.3 is m_2. This slope is used in Equation 3.17 for determining the permeability in the EIS, shown here:

$$K_e = \frac{q \cdot \mu}{2\pi \cdot h \cdot m_2} \tag{3.17}$$

For this example the equivalent permeability becomes:

$$K_e = \frac{1.00 \cdot 10^{-7} \cdot 0.4855}{2\pi \cdot 4.00 \cdot 10^{-3} \cdot 184153} \tag{3.18}$$

$$K_e = 1.0490 \cdot 10^{-11}\ m^2 \tag{3.19}$$

Finally the orthotropic permeability values K_x and K_y can be calculated from Equation 3.20:

$$K_x = \frac{K_e}{m_1} \qquad K_y = K_e \cdot m_1 \tag{3.20}$$

In this example:

$$K_x = \frac{1.0490 \cdot 10^{-11}\ m^2}{1.724} \qquad K_y = 1.0490 \cdot 10^{-11}\ m^2 \cdot 1.724 \tag{3.21}$$

$$K_x = 6.0847 \cdot 10^{-12}\ m^2 \qquad K_y = 1.8084 \cdot 10^{-11}\ m^2 \tag{3.22}$$

$$K_x = 6.08 \cdot 10^{-12}\ m^2 \qquad K_y = 1.81 \cdot 10^{-11}\ m^2 \tag{3.23}$$

Substituting these values into the orthotropic permeability tensor results in:

$$[\mathbf{K}] = \begin{pmatrix} 6.08 & 0 \\ 0 & 18.1 \end{pmatrix} \cdot 10^{-12}\ m^2 \tag{3.24}$$

Chapter 4

Results

Ten different trials were conducted; seven trials were performed using Rig 1 and three were performed using Rig 2.

Important parameters which were held essentially constant between all trials were the yarn spacing, stitch density, spacing between subsequent stitch lines, stitch fibre type, and stitch tension. Attempts were made to keep the spacing between yarns as small as possible; hence, the spacing between the centre of subsequent yarns was equal to the yarns width, 4 mm. Similarly, attempts were made to keep the spacing between individual stitch points to 4 mm; this was done to reinforce each yarn and prohibit them from slipping with respect to each other. The spacing between subsequent stitch lines was approximately 38.1 mm, this distance was chosen as it appeared to offer acceptable amounts of handle without introducing an excess amount of through-thickness stitches. These were all controlled during the manual manufacturing of the preforms and as a result some variability was unavoidable. Standard 100% polyester thread was used because of its ubiquity. The stitch tension was not directly measured nor was it kept strictly constant. The tension was manually adjusted after every stitch due to alterations made to the standard sewing machine used to stitch the preforms. The parameters which were changed between trials were the preform, fluid, and rig properties. The preform properties changed between trials were fibre materials, carbon or glass; target fibre volume fraction, ranging between 44.2% and 73.3%; number of layers, ranging between 4 to 16; stacking sequence, and whether or not the preform was compacted

in the compaction testing apparatus. The fibre volume fractions tested represented the upper range of values which would be applicable for manufacturing of primary and secondary load-bearing composite parts. The number of layers were a direct function of desired fibre volume fraction and preform thickness. Compaction of the preforms was done on approximately half of the trials in order to have a sample size where differences between compacted and not compacted preforms could be observed. The fluid properties changed between trials were the different dyeing agents. The rig properties changed between trials were the target cavity thickness, ranging between 2.43 mm and 4.00 mm, and the inlet flow rate, ranging between 0.100 $\frac{cm^3}{s}$ and 1.57 $\frac{cm^3}{s}$. The target cavity thickness was set to 4.00 mm, deviations from this will be discussed in the respective following sections. This thickness was an accurate representation of common part thicknesses. Chosen flow rates kept the cavity fill time within the gelation time of the Tri-Tex L-1911 epoxy and the flow rates were reduced to decrease the pressure differential. All of these parameters are tabulated for Rig 1 and Rig 2 in Tables 4.1 and 4.3 respectively.

Results generated from the data collected in the trials are tabulated in Tables 4.2 and 4.4, again for Rig 1 and Rig 2 respectively. The quantitative results which were tabulated were the isotropic permeability value, orthotropic permeability values, maximum pressure, elapsed time, and the amount of time over which the isotropic permeability was averaged. Averaging of the orthotropic permeability values was not performed due to the nature of the calculation, hence no amount of time over which the permeability was averaged is tabulated. Trials which have recorded values of isotropic permeability do not have orthotropic permeability values, and vice versa. The maximum pressure reached for each trial is also recorded. Furthermore, permeability values and maximum pressures are tabulated for both pressure transducers.

Discussion and documentation of individual results are discussed in their respective sections, which appear after the tabulated values.

Table 4.1: Parameters of trials conducted with Rig 1

Trial	01	02	03	04	05	06	07
Fibre material	Carbon	Glass	Glass	Glass	Glass	Glass	Glass
Fluid & dye	Silicone oil & Epodye	Silicone oil & Pylam LX 6258	Silicone oil & Pylam LX 6258	Silicone oil & Pylam LX 6258	Silicone oil & Pylam LX 6258	Silicone oil & Pylam LX 6258	Silicone oil & Pylam LX 6258
Target fibre volume fraction v_f	46.2%	52.4%	44.2%	44.2%	69.0%	62.9%	62.9%
Number of layers N_L	16	5	4	4	4	6	6
Target cavity thickness (mm) h	4.00	4.00	4.00	4.00	2.43	4.00	4.00
Stacking sequence	$[0, 90, 0, 90, 0, 90, 0, 90]_s$	[0,90,0,90,0]	$[0, 90]_s$	$[0, 90]_s$	$[0, 90]_s$	$[0, 90, 0]_s$	$[0, 90, 0]_s$
Yarn spacing (mm) s_y	4	4	4	4	4	4	4
Flow rate ($\frac{cm^3}{s}$) q	1.57	1.00	1.00	1.00	0.500	0.250	0.100
Number of repeated compactions	N/A	N/A	N/A	N/A	35	35	35

Table 4.2: Raw results obtained with Rig 1

Elapsed time (s)	17	44	400	51	110	210	714
Time over which isotropic permeability was averaged (s)	7		200		55	160	314
Maximum Pressure (PSI) [Wika Tronic]	120	97	69	51	66	78	62
Maximum Pressure (PSI) [Setra Systems]		100	70	51	67	80	64
K_y ($\times 10^{-11}$ m^2) [Wika Tronic]		7.92		26.4			
K_y ($\times 10^{-11}$ m^2) [Setra Systems]		7.05		26.0			
K_x ($\times 10^{-11}$ m^2) [Wika Tronic]		2.25		6.81			
K_x ($\times 10^{-11}$ m^2) [Setra Systems]		2.00		6.70			
Isotropic Permeability ($\times 10^{-11}$ m^2) [Wika Tronic]	18.1		24.6		9.58	2.12	1.34
Isotropic Permeability ($\times 10^{-11}$ m^2) [Setra Systems]			24.4		9.49	2.07	1.31
Trial	01	02	03	04	05	06	07

Table 4.3: Parameters of trials conducted with Rig 2

Trial	08	09	10
Fibre material	Glass	Glass	Carbon
Fluid & dye	Silicone oil & Pylam LX 6258	Silicone oil & Pylam LX 6258	Silicone oil & Epodye
Target fibre volume fraction v_f	73.3%	62.9%	57.0%
Number of layers N_L	7	6	12
Target cavity thickness (mm) h	4.00	4.00	2.43
Stacking sequence	[0,90,0,90,0,90,0]	$[0, 90, 0]_s$	$[0, 90, 0, 90, 0, 90]_s$
Yarn spacing (mm) s_y	4	4	4
Flow rate ($\frac{cm^3}{s}$) q	0.100	0.100	0.100
Number of repeated compactions	35	35	N/A

Table 4.4: Raw results obtained with Rig 2

Elapsed time (s)	440	440	1504	1504	892
Time over which isotropic permeability was averaged (s)					
Maximum Pressure (PSI) [Wika Tronic]	95	95	103	103	75
Maximum Pressure (PSI) [Setra Systems]	96	96			76
K_y ($\times 10^{-11}$ m^2) [Wika Tronic]	1.84	2.38	1.29	0.709	5.94
K_y ($\times 10^{-11}$ m^2) [Setra Systems]	1.81	2.35			5.87
K_x ($\times 10^{-11}$ m^2) [Wika Tronic]	0.620	1.22	0.435	0.572	4.39
K_x ($\times 10^{-11}$ m^2) [Setra Systems]	0.608	1.20			4.33
Isotropic Permeability ($\times 10^{-11}$ m^2) [Wika Tronic]					
Isotropic Permeability ($\times 10^{-11}$ m^2) [Setra Systems]					
Trial	08′	08	09′	09	10′

Prime denotes that values were calculated from the camera directed towards the polycarbonate plate with injection port

4.1 Trial 01: Carbon fibre, 16 layers, 4.00 mm preform thickness, volumetric flow rate of 1.57 $\frac{cm^3}{s}$

Trial 01 was conducted using Rig 1 with 4.00 mm spacers. Infusion elapsed approximately 17 seconds. The trial exceeded the maximum pressure capable of being produced by the pump; the specifics of the pump are described below. The trial was considered complete after the maximum pressure had been reached.

The fluid used was silicone oil mixed with Epodye.

The preform featured 16 layers of carbon. The layers were stacked according to the sequence [0/90/0/90/0/90/0/90/90/0/90/0/90/0/90/0], which can also be written as $[0/90/0/90/0/90/0/90]_s$. The preform was symmetric in thickness and balanced. Individual layers of carbon were made of 80 yarns spaced approximately 4 mm apart. The preform was stitched with approximately one stitch point per yarn with successive stitching lines approximately 38.1 mm apart. The stitch lines were perpendicular to the top and bottom carbon layers. As a note, preforms in all trials, regardless of fibre material, had a similar number of yarns per layer, stitch point spacing, and spacing between subsequent stitch lines. Slight variations of these parameters were caused by manual preform manufacturing. The preform was not compacted in the compaction testing apparatus prior to injection. The target v_f was calculated as approximately 46.2%.

This trial was the only trial which did not use the hydraulic cylinder and Instron testing apparatus, rather this trial used a positive displacement diaphragm metering pump, specifically the Pulsafeeder RK-74142-10 which could generate a maximum pressure of 689 kPa (100 psi). The pump was set for an inlet flow rate of 1.57 $\frac{cm^3}{s}$. This style of pump uses a reciprocating mechanism to move fluid and does not provide a perfectly constant flow rate. The pump was chosen initially because of its ease of use. The hydraulic cylinder setup was used for future trials to decrease the inconsistencies in the flow rate.

The inlet gauge pressure exceeded the maximum gauge pressure of the Setra Systems transducer so only the gauge pressure recordings from the Wika Tronic transducer will be presented. The Wika Tronic pressure transducer recorded a maximum inlet gauge pressure

of 814 kPa (118 psi). The curves showing inlet gauge pressure as a function of elapsed time appear in Appendix 5.

The flow field most closely matched the isotropic flow pattern, thus the isotropic set of equations were used for calculating the permeability. The permeability, standard error of the mean, and population sample were:

$$K_{WT} = 18.1 \cdot 10^{-11}\ m^2$$
$$SE_{K_{WT}} = 1.21 \cdot 10^{-11}\ m^2$$
$$N_{K_{WT}} = 66$$

where K_{WT} is the permeability value, $SE_{K_{WT}}$ is the standard error of the mean, and $N_{K_{WT}}$ is the number of data points over which the permeability was averaged. All of these parameters were determined from pressure data of the Wika Tronic Industrial Pressure Transducer, accurate from 0 kPag (0 psig) to 2.07 MPa (300 psig).

While the experimental flow field and front most closely matched the isotropic flow pattern, discrepancies were observed. The largest issue was the non-uniform filling of the preform within the constructed circle. Large oil-rich-zones can be easily identified by the fluorescent dye in Figure 4.1:

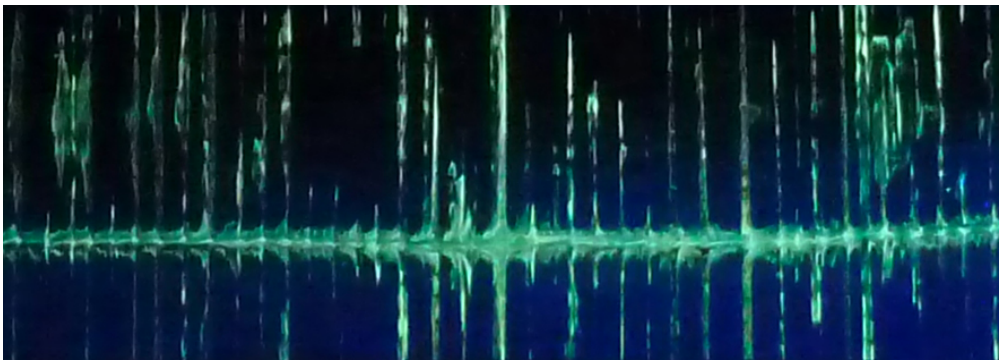

Figure 4.1: Magnified zone close to the injection port, Trial 01

4.2 Trial 02: Glass fibre, 5 layers, 4.00 mm preform thickness, volumetric flow rate of 1.00 $\frac{cm^3}{s}$

Trial 02 was conducted using Rig 1 with 4.00 mm spacers. Infusion elapsed approximately 44 seconds. Timing of the trials started as soon as any fluid was visible and concluded upon fluid reaching the closest edge of the outlet groove.

The fluid used was silicone oil mixed with Pylakrome Blue Dye.

The preform featured 5 layers of glass. The layers of glass were stacked according to the sequence [0/90/0/90/0]; the preform was symmetric in thickness and was not balanced. The preform was not compacted in the compaction testing apparatus prior to injection. The target v_f was calculated as approximately 52.4%.

A compressive displacement rate of 13.2 $\frac{mm}{min}$ was programmed into the Instron testing apparatus corresponding to an inlet flow rate of 1.00 $\frac{cm^3}{s}$.

Pressure transducers read maximum inlet gauge pressures of 674 kPa (97.7 psi) and 671 kPa (97.2 psi) for the Setra Systems and Wika Tronic transducer, respectively. The inlet gauge pressure as a function of elapsed time curves appear in Appendix 5 as well as in Figure 4.2. No error bars were included in the figure because the errors were small and the error bars obscured the presented information; as previously stated, the pressure transducer errors were ±0.896 kPa (±0.13 psi) and ±10.3 kPa (±1.5 psi) for the Setra Systems and Wika Tronic transducer, respectively.

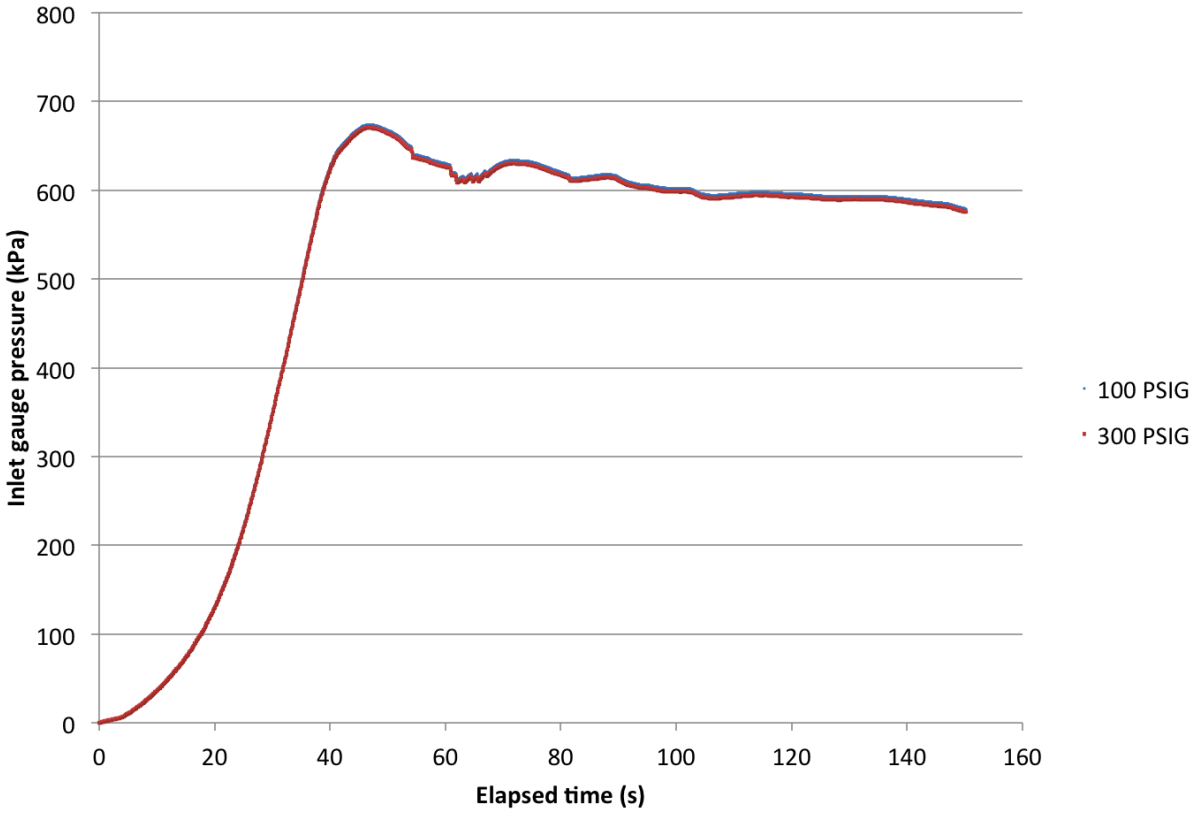

Figure 4.2: Inlet gauge pressure as a function of elapsed time, Trial 02

Rig 1 required only one camera and still images of the infusion are displayed in Appendix 5.

The flow field most closely matched the orthotropic flow pattern, thus the orthotropic set of equations were used for calculating the permeability. The permeability was:

$$[\mathbf{K}]_{SS} = \begin{pmatrix} 2.10 & 0 \\ 0 & 7.38 \end{pmatrix} \cdot 10^{-11}\ m^2 \qquad [\mathbf{K}]_{WT} = \begin{pmatrix} 2.25 & 0 \\ 0 & 7.92 \end{pmatrix} \cdot 10^{-11}\ m^2$$

where $[\mathbf{K}]_{SS}$ and $[\mathbf{K}]_{WT}$ are the permeability tensors determined from pressure data of the Setra Systems Model DPT 209 transducer, accurate from 0 kPag (0 psig) to 689 kPag

(100 psig), and from pressure data of the Wika Tronic Industrial Pressure Transducer, accurate from 0 kPag (0 psig) to 2.07 MPa (300 psig), respectively.

Differences between the two values were caused by the sensitivity of the pressure transducers. The Setra Systems transducer was the more accurate transducer used and since the trial never exceeded the maximum pressure of that transducer the permeability is likely closer to the $[\mathbf{K}]_{SS}$ tensor.

While the experimental flow field and front most closely matched the orthotropic flow pattern, discrepancies were observed. The largest issue was the non-uniform filling of the preform within the constructed ellipse. The fluid travelled preferentially along the stitches causing the fibres in-between stitch lines to be wetted much later than they would in a more homogeneous porous medium. Regions close to the injection port wetted more thoroughly; however, dry fibres and yarns were still visible, an example of this is displayed in Figure 4.3.



Figure 4.3: Dry spots present in the preform, Trial 02

As expected, the fluid travelled preferentially along the fibre directions. The preform was unbalanced and more yarns were laid at 0° than at 90°. Highest permeability was recorded for the 0° direction. Worth noting is the larger effect on orthotropy of parallel yarns compared to that of stitching; stitches were perpendicular to 0° direction, yet the majority of the fluid still travelled in the 0° direction.

The through-thickness permeability being significantly lower than the in-plane permeability of the preform resulted in the recorded flow front progression appearing to jump

between the stitch lines. The fluid travelled in-plane faster on the injection side until it began filling the highly porous regions near the stitch line, whereupon the fluid could be viewed on the camera.

4.3 Trial 03: Glass fibre, 4 layers, 4.00 mm preform thickness, volumetric flow rate of 1.00 $\frac{cm^3}{s}$

Trial 03 was conducted using Rig 1 with 4.00 mm spacers. This case is similar to Trial 02 but the preform fibre volume fraction was reduced to 44.2% by decreasing the amount of layers to 4 layers. This reduction changed the stacking sequence to $[0/90]_s$. This preform was symmetric in thickness and balanced. The yarn spacing, stitch spacing, and stitch density were not changed between this trial and Trial 02. Preform manufacturing was done manually so slight changes in these parameters between the two preforms were unavoidable.

The inlet flow rate for this trial was set to 1.00 $\frac{cm^3}{s}$ by setting the compressive displacement rate of the Instron testing apparatus to 13.2 $\frac{mm}{min}$. However, the hydraulic cylinder rotated within the fittings such that the axis of the compressive displacement did not match the axis of the piston. This reduced the flow rate corresponding to the rotated angle but at the time this data was not recorded. The approximate maximum angle formed was 20° which would have decreased the flow rate by less than 10%; isotropic permeability is linearly proportional to flow rate, hence the actual permeability is an overestimate. While the exact permeability values for this trial may not be entirely accurate, documentation of the filling process was still valid.

The Setra Systems and Wika Tronic pressure transducers read maximum inlet gauge pressures of 207 kPa (30.1 psi) and 204 kPa (29.7 psi) respectively. These pressures correspond to the maximum pressures recorded while the video of the trial was being recorded, but limitation in video length caused the observable trial to conclude prior to the fluid reaching the cavity edge. The pressure transducers continued recording until the end of the trial and the maximum pressures recorded then were 479 kPa (69.5 psi) and 475 kPa (69.0 psi) for the Setra Systems and Wika Tronic transducers respectively. Pressure data was collected for 400 seconds while the video data was only collected for 263 seconds. The inlet gauge pressure as a function of elapsed time curves are displayed in Appendix 5.

Appendix 5 also displays the flow progression which can be seen to be much more isotropic than the previous trial. Solving the relevant isotropic equations results in the permeability

values:

$$K_{SS} = 24.4 \cdot 10^{-11}\ m^2 \qquad K_{WT} = 24.6 \cdot 10^{-11}\ m^2$$
$$SE_{K_{SS}} = 2.45 \cdot 10^{-12}\ m^2 \qquad SE_{K_{WT}} = 2.49 \cdot 10^{-12}\ m^2$$
$$N_{K_{SS}} = 2001 \qquad N_{K_{WT}} = 2001$$

where K_{SS} is the permeability value, $SE_{K_{SS}}$ is the standard error of the mean, and $N_{K_{WT}}$ is the number of data points over which the permeability was averaged. All of these parameters were determined from pressure data of the Setra Systems Model DPT 209, accurate from 0 kPag (0 psig) to 689 kPag (100 psig).

These values are based on a volumetric flow rate of 1.00 $\frac{cm^3}{s}$ and the actual preform permeability would be lower than the values computed.

Similar to Trial 02, the pressure did not exceed the more sensitive pressure transducer's limit, thus K_{SS} is deemed closer to the true permeability of the preform.

Race tracking along the stitch lines was observed but the flow front progression remained consistent along both primary axes. The wetting of the preform was significantly better than with the previous glass trial; however, dry regions were still observed, even close to the injection port, displayed in Figure 4.4. The lower through-thickness permeability would result in the recorded side having more dry regions.

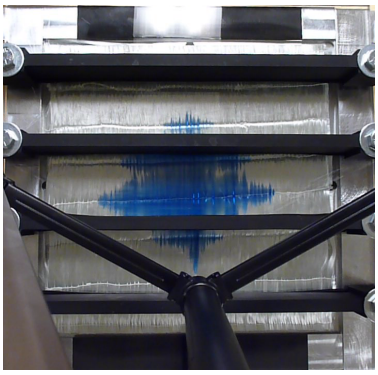

(a) Full view of the preform

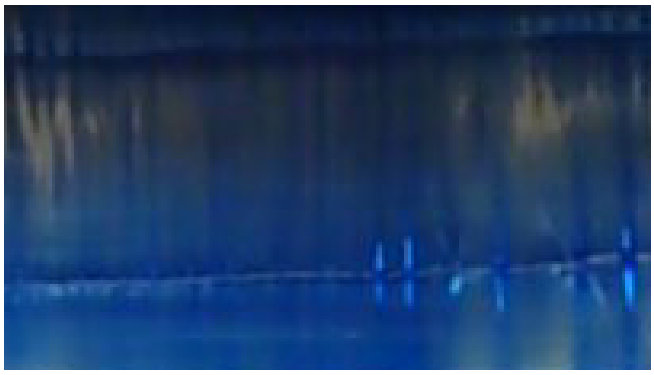

(b) Wetted region near injection port

Figure 4.4: End of test, Trial 03

4.4 Trial 04: Glass fibre, 4 layers, 4.00 mm preform thickness, volumetric flow rate of 1.00 $\frac{cm^3}{s}$

Trial 04 was conducted with the same parameters as Trial 03 except that corrections were made to ensure that the axis of the piston was aligned with the Instron testing apparatus.

The actual flow rate for this trial was 1.00 $\frac{cm^3}{s}$ and the infusion elapsed approximately 51 seconds.

The Setra Systems and Wika Tronic pressure transducer read maximum gauge pressures of 354 kPa (51.3 psi) and 351 kPa (50.9 psi), respectively. The inlet gauge pressure as a function of elapsed time curves are displayed in Appendix 5.

Appendix 5 also displays the flow front progression which can be seen to be orthotropic. Solving the relevant equations results in the permeability tensors:

$$[\mathbf{K}]_{SS} = \begin{pmatrix} 6.70 & 0 \\ 0 & 25.99 \end{pmatrix} \cdot 10^{-11}\ m^2 \qquad [\mathbf{K}]_{WT} = \begin{pmatrix} 6.81 & 0 \\ 0 & 26.44 \end{pmatrix} \cdot 10^{-11}\ m^2$$

Given that the pressure did not exceed the more sensitive pressure transducer's limit, the $[\mathbf{K}]_{SS}$ is deemed closer to the true permeability of the preform.

Race tracking along the stitch lines was observed and since this preform was balanced, this race tracking was the major contributing factor in the anisotropy of the preform; the stitch line direction was the direction of maximum permeability.

The preform appeared to have significantly better fibre wetting than the previous orthotropic trial. However, the degree of orthotropy was such that the fluid reached the outlet groove edge prior to a large proportion of the preform being wetted. Similarly to previous trials, discontinuities in flow front progression were recorded due to the lower through-thickness permeability.

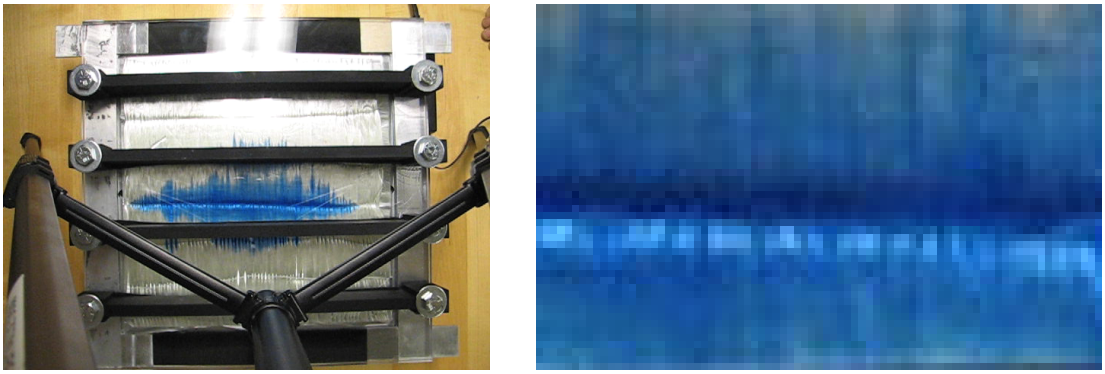

(a) Full view of the preform (b) Wetted region near injection port

Figure 4.5: End of test, Trial 04

4.5 Trial 05: Glass fibre, 4 layers, 2.43 mm preform thickness, 35 compaction cycles, volumetric flow rate of 0.500 $\frac{cm^3}{s}$

Trial 05 was the first trial to use a preform which was compacted repeatedly in the compaction testing apparatus. This was done in an attempt to improve the homogeneity of the preform, in turn improving the uniformity of the flow front. This also had the benefit of increasing the fibre volume fraction. Prior to repeated compaction, the preform used in this trial had the same parameters as the preforms used in Trial 03 and Trial 04. The thickness of the preform was reduced throughout the compaction cycle such that the 4.00 mm cavity used previously was reduced to 2.43 mm without a significant increase in pressure needed to compress and fit the preform into the cavity.

35 compaction cycles were performed with a maximum compressive force of 50 kN. Based on the preform area of 0.104 m^2 the maximum applied compaction pressure was 479 kPa (compressive). The decision to use an applied compaction pressure of approximately 0.5 MPa was made because no major damage in the rovings was likely to occur for pressures this low [51]. Selected cycles of preform compaction are displayed in Appendix 5. The curves were generated assuming that the displacement correction C_i was linearly correlated with the instantaneous pressure divided by the maximum pressure. However, without a preform the compaction testing apparatus was not linearly elastic. Hence, the curves display the trend and not the exact physical phenomena. The assumption of a linear elastic compaction testing apparatus was not made for subsequent trials and the full displacement correction profile was applied instead. The final value for the fibre volume fraction, 76%, was calculated using the final pressure value and is correct.

A compressive displacement rate of 6.58 $\frac{mm}{min}$ was programmed into the Instron testing apparatus corresponding to an inlet flow rate of 0.500 $\frac{cm^3}{s}$. Infusion elapsed approximately 94 seconds.

The Setra Systems and Wika Tronic pressure transducers read maximum inlet gauge pressures of 461 kPa (66.9 psi) and 457 kPa (66.3 psi), respectively. The inlet gauge pressure as a function of elapsed time curves are displayed in Appendix 5.

Appendix 5 also displays the flow progression which can be seen to be isotropic. Solving the relevant equations results in the permeability values:

$$K_{SS} = 9.26 \cdot 10^{-11}\ m^2 \qquad K_{WT} = 9.34 \cdot 10^{-11}\ m^2$$
$$SE_{K_{SS}} = 1.65 \cdot 10^{-13}\ m^2 \qquad SE_{K_{WT}} = 1.68 \cdot 10^{-13}\ m^2$$
$$N_{K_{SS}} = 401 \qquad N_{K_{WT}} = 401$$

Again, K_{SS} is deemed closer to the true permeability of the preform.

The preform infused well in comparison to previous trials. A similar extent of race tracking was also observed similar to previous trials.

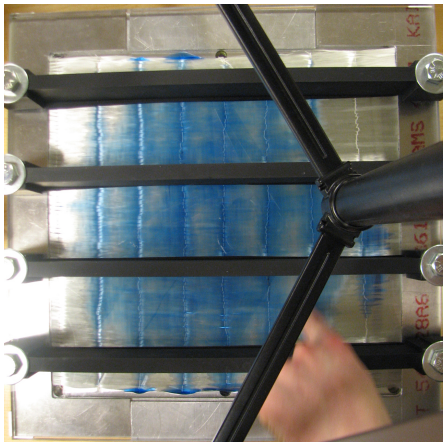

(a) Full view of the preform

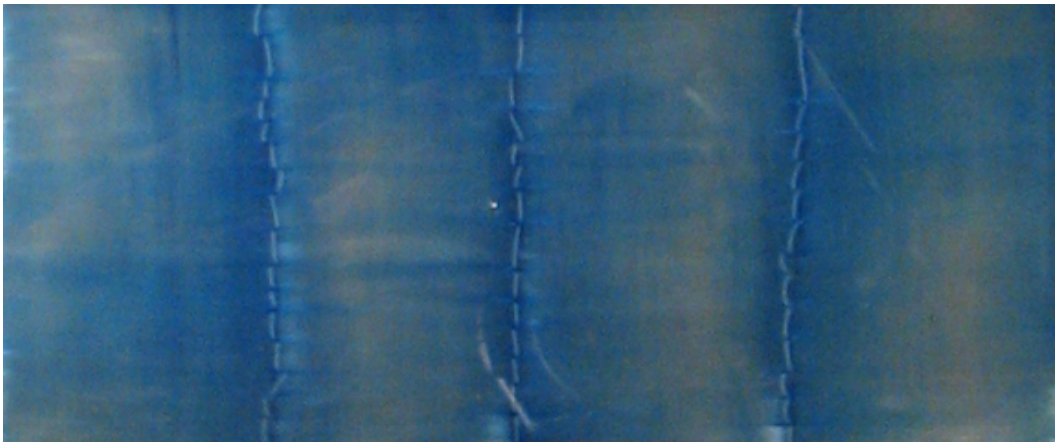

(b) Wetted region near injection port

Figure 4.6: End of test, Trial 05

4.6 Trial 06: Glass fibre, 6 layers, 4.00 mm preform thickness, 35 compaction cycles, volumetric flow rate of 0.250 $\frac{cm^3}{s}$

Trial 06 was conducted using Rig 1 with 4.00 mm spacers.

The preform featured 6 layers of glass. The layers of glass were stacked according to the sequence $[0/90/0]_s$, the preform was symmetric in thickness and was not balanced. The preform was compacted in the compaction testing apparatus prior to injection. The target v_f was calculated as approximately 62.9%.

The maximum applied compaction pressure for the 35 cycles of compaction was 508 kPa (compressive). This pressure was determined using a preform area of 0.0983 m^2. Selected cycles of preform compaction are displayed in Appendix 5. The increase in uniformity is visible in Figure 4.7 by a more uniform reflectance and in Figure 4.8 by a decrease in volume of the void zones surrounding the stitches.

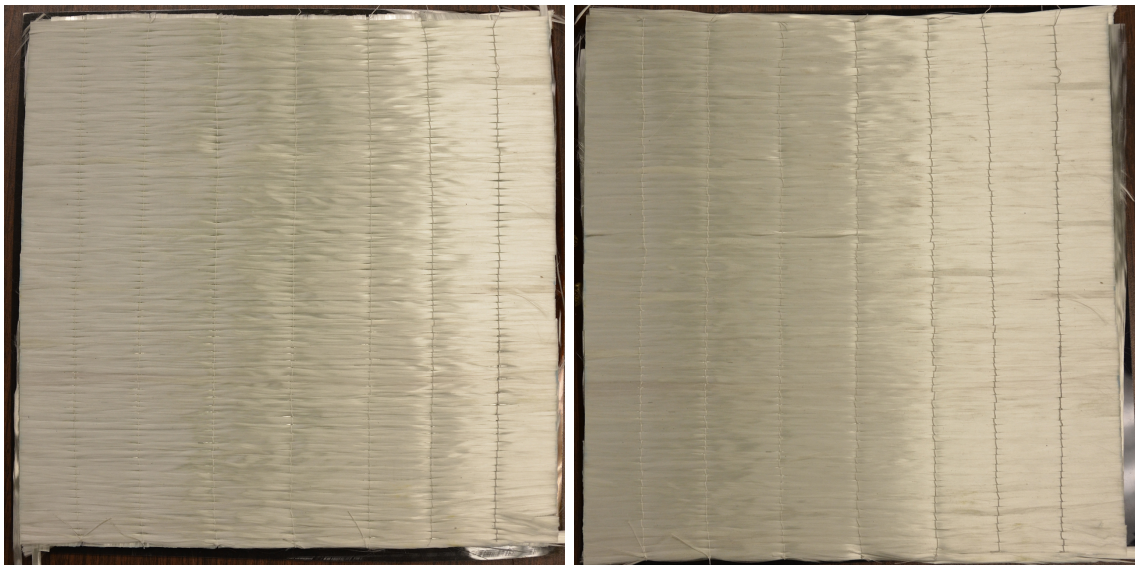

(a) Pre-compaction (b) Post-compaction

Figure 4.7: Glass preform, Trial 06

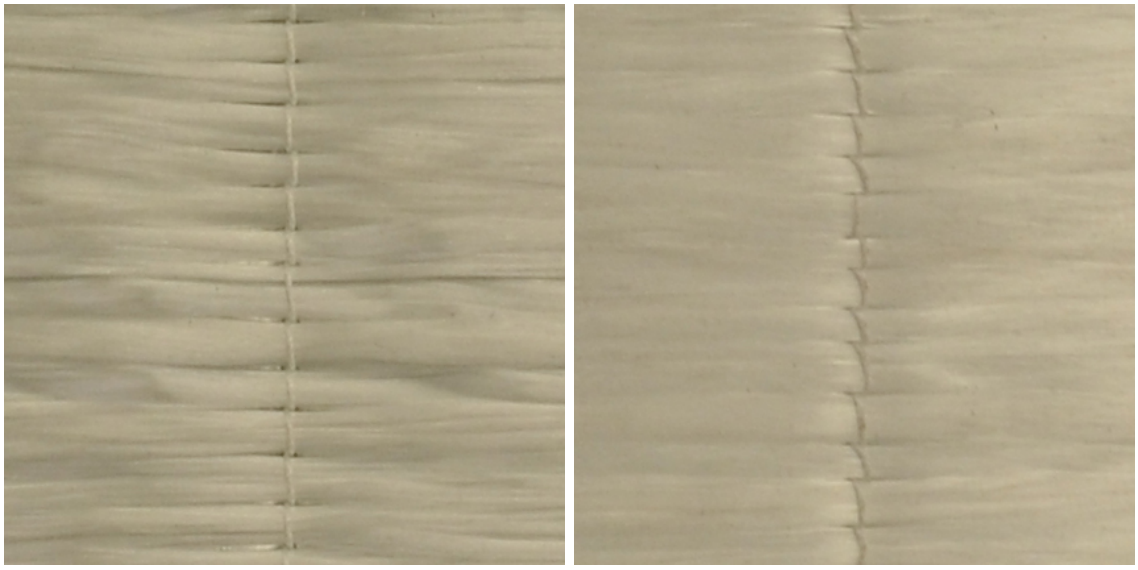

(a) Pre-compaction stitch line (b) Post-compaction stitch line

Figure 4.8: Magnification of the glass preform, Trial 06

A compressive displacement rate of 3.30 $\frac{mm}{min}$ was programmed into the Instron testing apparatus corresponding to an inlet flow rate of 0.250 $\frac{cm^3}{s}$.

Pressure transducers read maximum inlet gauge pressures of 553 kPa (80.3 psi) and 539 kPa (78.3 psi) for the Setra Systems and Wika Tronic transducers, respectively. The curves showing inlet gauge pressure as a function of elapsed time are displayed in Appendix 5.

Appendix 5 also displays the flow progression which can be seen to be isotropic. Solving the relevant equations results in the permeability values:

$$K_{SS} = 2.07 \cdot 10^{-11}\ m^2 \qquad K_{WT} = 2.12 \cdot 10^{-11}\ m^2$$
$$SE_{K_{SS}} = 4.69 \cdot 10^{-14}\ m^2 \qquad SE_{K_{WT}} = 4.82 \cdot 10^{-14}\ m^2$$
$$N_{K_{SS}} = 1639 \qquad N_{K_{WT}} = 1639$$

Again, K_{SS} is deemed closer to the true permeability of the preform.

The preform had less dry spots close to the injection port; however, significant race tracking along the stitch lines caused the fluid to reach the outlet groove prior to yarns and

fibres between stitch lines being fully wetted. Both of these phenomena are displayed in Figure 4.9:

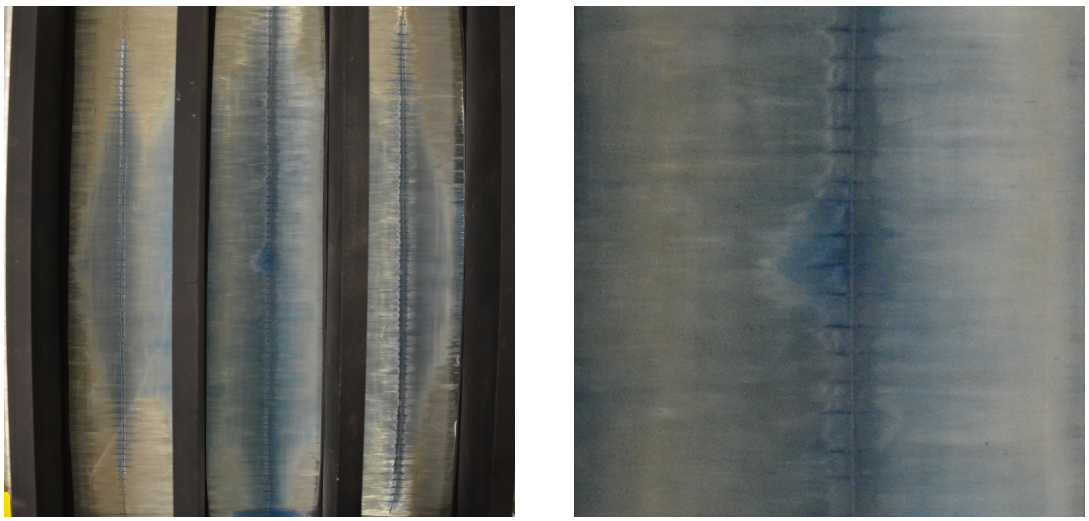

(a) Full view of the preform (b) Wetted region near injection port

Figure 4.9: End of test, Trial 06

4.7 Trial 07: Glass fibre, 6 layers, 4.00 mm preform thickness, 35 compaction cycles, volumetric flow rate of 0.100 $\frac{cm^3}{s}$

Trial 07 was conducted using Rig 1 with 4.00 mm spacers. The parameters of the preform were the same as for Trial 06.

The maximum applied compaction pressure for the 35 cycles of compaction was 474 kPa (compressive). This pressure was determined using a preform area of 0.106 m^2. Selected cycles of preform compaction are displayed in Appendix 5. Photographs of the preform were only taken after the compaction and are displayed in Figure 4.10:

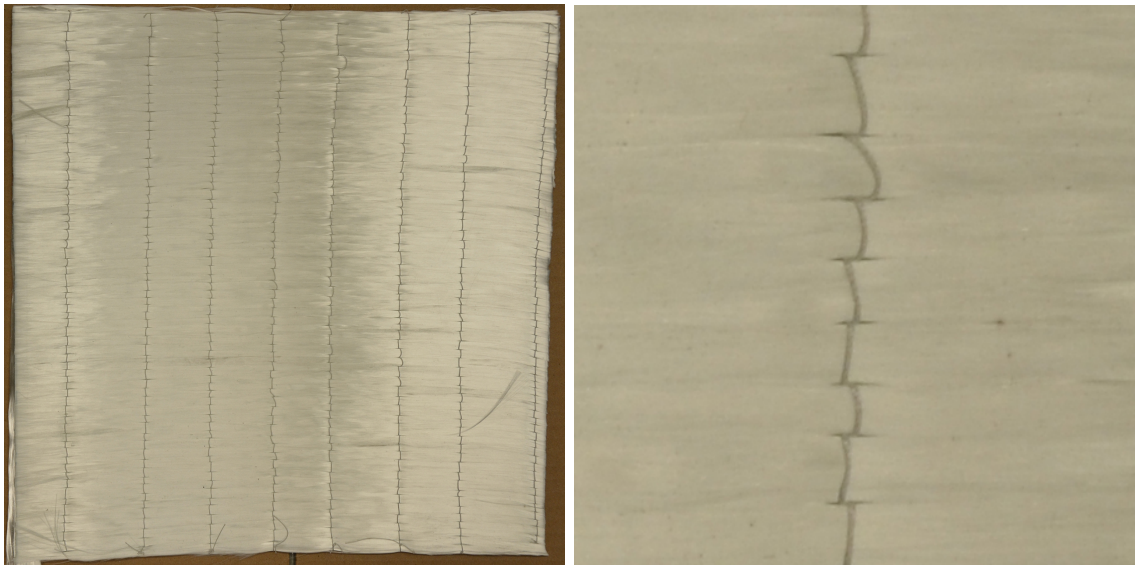

(a) Glass preform

(b) Magnification of the post-compaction stitch line

Figure 4.10: Post-compaction preform, Trial 07

A compressive displacement rate of 1.32 $\frac{mm}{min}$ was programmed into the Instron testing apparatus corresponding to an inlet flow rate of 0.100 $\frac{cm^3}{s}$.

Pressure transducers read maximum inlet gauge pressures of 439 kPa (63.7 psi) and 430 kPa (62.3 psi) for the Setra Systems and Wika Tronic transducers, respectively. The curves of inlet gauge pressure as a function of elapsed time are displayed in Appendix 5.

Appendix 5 also displays the flow progression which can be seen to be isotropic. Solving the relevant equations results in the permeability values:

$$K_{SS} = 1.31 \cdot 10^{-11}\ m^2 \qquad K_{WT} = 1.34 \cdot 10^{-11}\ m^2$$
$$SE_{K_{SS}} = 3.47 \cdot 10^{-15}\ m^2 \qquad SE_{K_{WT}} = 3.52 \cdot 10^{-15}\ m^2$$
$$N_{K_{SS}} = 3141 \qquad N_{K_{WT}} = 3141$$

Again, K_{SS} is deemed closer to the true permeability of the preform.

Dry regions were observed for this trial. Race-tracking along the stitch lines was still observed. Both of these phenomena are displayed in Figure 4.11:

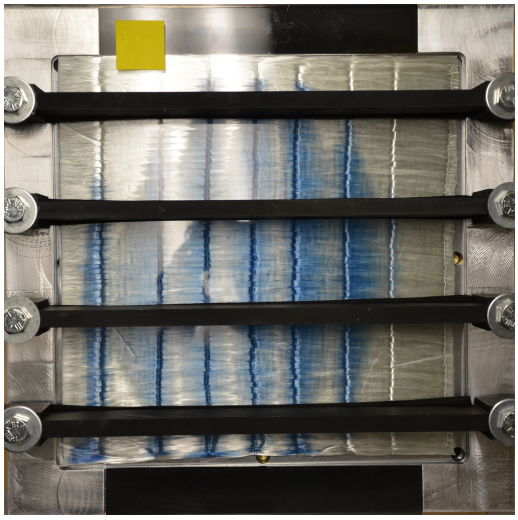

(a) Full view of the preform

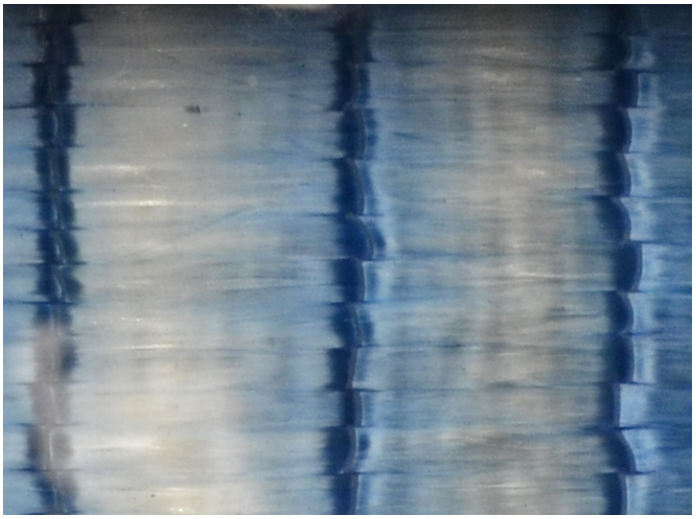

(b) Wetted region near injection port

Figure 4.11: End of test, Trial 07

4.8 Trial 08: Glass fibre, 7 layers, 4.00 mm preform thickness, 35 compaction cycles, volumetric flow rate of 0.100 $\frac{cm^3}{s}$

Trial 08 was conducted using Rig 2 with 4.00 mm spacers.

The glass preform featured 7 layers of glass. The layers of glass were stacked according to the sequence [0/90/0/90/0/90/0], the preform was symmetric in thickness and was not balanced. The target v_f was calculated as approximately 73.3%. The preform was subjected to 35 cycles of compaction with a constant maximum compressive force of 50 kN. Based on the preform area of 0.1057 m^2 the applied compaction pressure was 473 kPa (compressive). Selected cycles of preform compaction are displayed in Appendix 5 as well as in Figure 4.12:

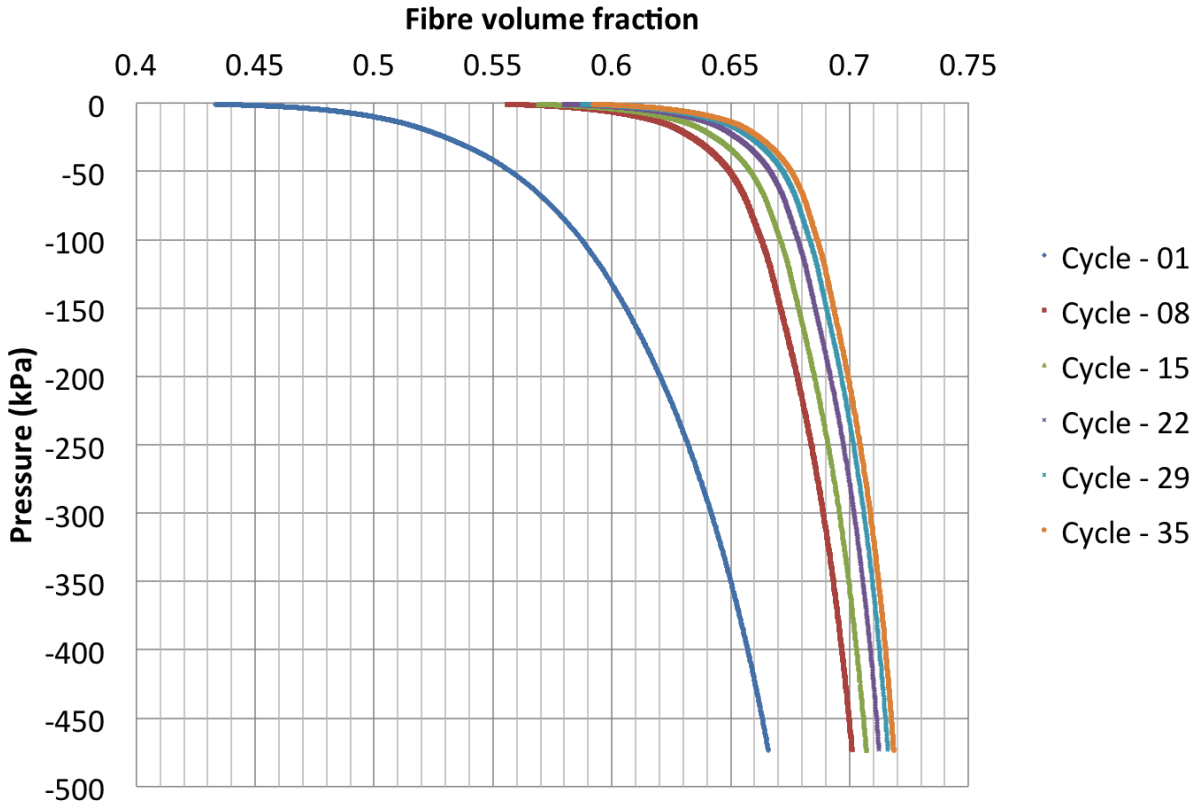

Figure 4.12: Selected cycles of preform compaction, Trial 08

Applying Equation 3.6, the relative difference between the pre-compaction area, 0.1072 m^2 (166.5 in^2), and post-compaction area, 0.1057 m^2 (163.9 in^2), was approximately 1.5%.

Qualitatively the increased uniformity of the preform is quite visible in Figures 4.13 and 4.14.

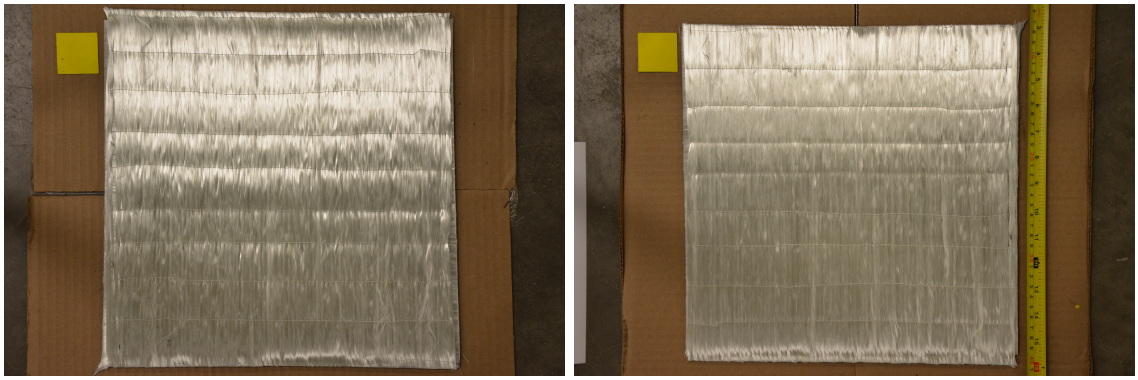

(a) Pre-compaction (b) Post-compaction

Figure 4.13: Glass preform, Trial 08

This increased uniformity of the preform is a result of fibres reorganizing into a more collimated structure. This reorganization reduced the inconsistent defects in gap spacing, and is also expected to increase the final component properties by increasing the amount of in-plane fibres per unit length; however, this was not tested.



(a) Pre-compaction stitch line (b) Post-compaction stitch line

Figure 4.14: Magnification of the glass preform, Trial 08

As a note, the photographs shown in Figure 4.14 have a yellow pin laid on the preform; the pin has a diameter of approximately 4.0 mm. The pin was only added to give a reference scale and the pin was removed after the photographs were taken.

A compressive displacement of 1.32 $\frac{mm}{min}$ was programmed into the Instron testing apparatus corresponding to an inlet flow rate of 0.100 $\frac{cm^3}{s}$. Infusion elapsed approximately 440 seconds.

The pressure transducers read maximum inlet gauge pressures of 661 kPa (95.9 psi) and 652 kPa (94.5 psi), for the Setra Systems and Wika Tronic pressure transducers, respectively. The curves showing inlet gauge pressure as a function of elapsed time are displayed in Appendix 5.

This trial was conducted using one camera on either side of the flow plane. Two different flow fronts were observed. One flow front was recorded using the Canon Powershot camera directed towards the polycarbonate plate without the injection port, while the other flow front was recorded using the Nikon D7000 camera directed towards the polycarbonate plate with the injection port. Selected still images of the recorded videos from both cameras are displayed in Appendix 5. These two flow fronts result in two different permeability tensors. The permeability tensor determined using data from Nikon D7000 was:

$$[\mathbf{K}]_{SS} = \begin{pmatrix} 1.20 & 0 \\ 0 & 2.35 \end{pmatrix} \cdot 10^{-11}\ m^2 \qquad [\mathbf{K}]_{WT} = \begin{pmatrix} 1.22 & 0 \\ 0 & 2.38 \end{pmatrix} \cdot 10^{-11}\ m^2$$

While the permeability tensor determined using data from the Canon Powershot was:

$$[\mathbf{K}]_{SS} = \begin{pmatrix} 0.608 & 0 \\ 0 & 1.81 \end{pmatrix} \cdot 10^{-11}\ m^2 \qquad [\mathbf{K}]_{WT} = \begin{pmatrix} 0.620 & 0 \\ 0 & 1.84 \end{pmatrix} \cdot 10^{-11}\ m^2$$

As expected, the preform wetted much more in the plane closest to the injection port. The degree of orthotropy left a large portion of the preform dry.

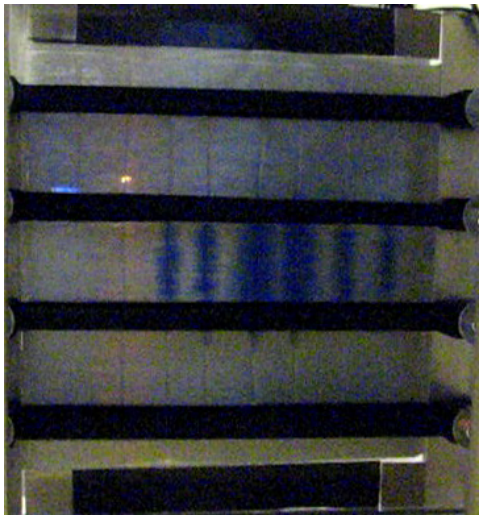

(a) Still image from the Canon Powershot camera

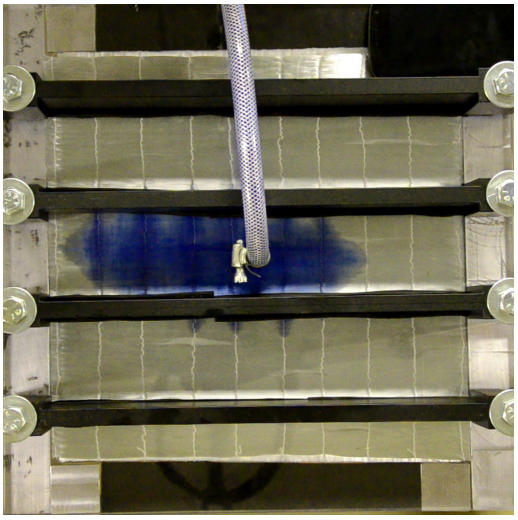

(b) Still image from the Nikon D7000 camera

Figure 4.15: End of test, Trial 08

4.9 Trial 09: Glass fibre, 6 layers, 4.00 mm preform thickness, 35 compaction cycles, volumetric flow rate of 0.100 $\frac{cm^3}{s}$

Trial 09 was conducted using Rig 2 with 4.00 mm spacers. The parameters of the preform were the same as for Trial 06 and Trial 07.

The maximum applied compaction pressure for the 35 cycles of compaction was 475 kPa (compressive). This pressure was determined using a preform area of 0.1053 m^2. Selected cycles of preform compaction are displayed in Appendix 5.

The relative difference between the pre-compaction area, 0.1040 m^2 (161.2 in^2), and post-compaction area, 0.1053 m^2 (163.2 in^2), was approximately 1.2%.

Qualitatively the increased uniformity of the preform is visible in Figures 4.16 and 4.17.

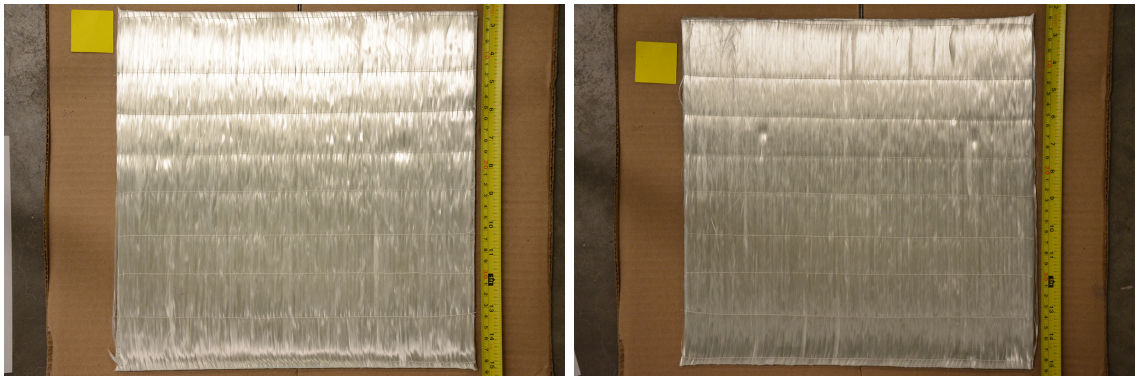

(a) Pre-compaction (b) Post-compaction

Figure 4.16: Glass preform, Trial 09



(a) Pre-compaction stitch line (b) Post-compaction stitch line

Figure 4.17: Magnification of the glass preform, Trial 09

The same pin as previously described was used for giving the magnified photographs scale.

A compressive displacement of 1.32 $\frac{mm}{min}$ was programmed into the Instron testing apparatus corresponding to an inlet flow rate of 0.100 $\frac{cm^3}{s}$. Infusion elapsed approximately 1504 seconds.

The inlet gauge pressure exceeded the maximum gauge pressure of the Setra Systems transducer so only the gauge pressure recordings of the Wika Tronic transducer will be presented. The Wika Tronic pressure transducer recorded a maximum inlet gauge pressure of 710 kPa (103 psi). The curves showing inlet gauge pressure as a function of elapsed time appear in Appendix 5.

The permeability tensor determined using data from the Nikon D7000 camera was:

$$[\mathbf{K}]_{WT} = \begin{pmatrix} 0.765 & 0 \\ 0 & 1.81 \end{pmatrix} \cdot 10^{-11}\ m^2$$

While the permeability tensor determined using data from the Canon Powershot was:

$$[\mathbf{K}]_{WT} = \begin{pmatrix} 0.572 & 0 \\ 0 & 0.709 \end{pmatrix} \cdot 10^{-11}\ m^2$$

This trial had significantly better wetting than the previous trial. Again, the preform wetted better in the plane closest to the injection port.

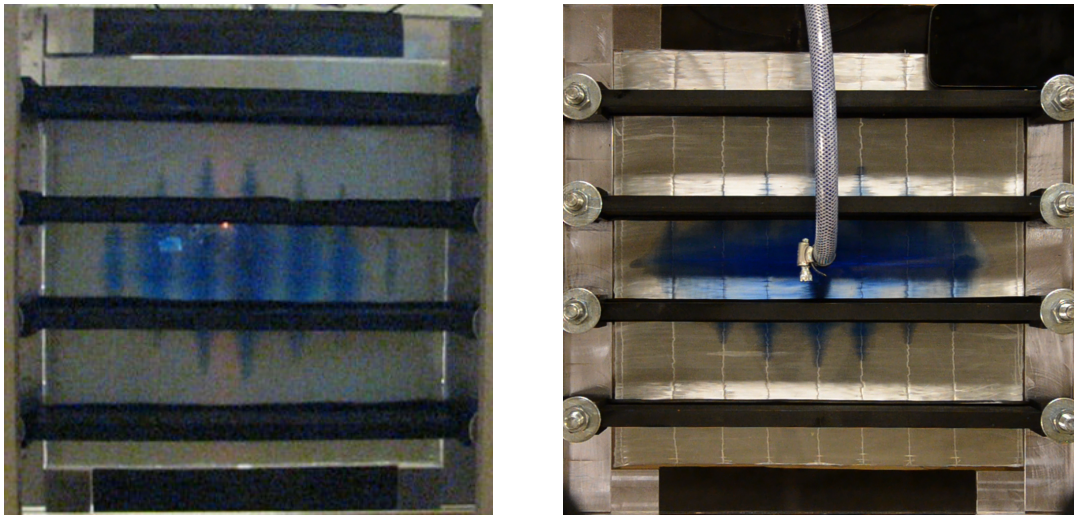

(a) Still image from the Canon Powershot camera

(b) Still image from the Nikon D7000 camera

Figure 4.18: End of test, Trial 09

4.10 Trial 10: Carbon fibre, 12 layers, 2.43 mm preform thickness, volumetric flow rate of 0.100 $\frac{cm^3}{s}$

Trial 10 was conducted using Rig 2 with 2.43 mm spacers. Infusion elapsed approximately 892 seconds. The fluid was silicone oil mixed with Epodye.

The preform featured 12 layers of carbon. The layers of carbon were stacked according to the sequence $[0/90/0/90/0/90]_s$, the preform was symmetric in thickness and was balanced. The preform was not compacted in the compaction testing apparatus prior to injection. The target v_f was calculated as approximately 57.0%.

A compressive displacement rate of 1.32 $\frac{mm}{min}$ was programmed into the Instron testing apparatus corresponding to an inlet flow rate of 0.100 $\frac{cm^3}{s}$.

The pressure transducers read maximum inlet gauge pressures of 523 kPa (75.9 psi) and 516 kPa (74.9 psi), for the Setra Systems and Wika Tronic pressure transducers, respectively. The curves showing inlet gauge pressure as a function of elapsed time are displayed in Appendix 5.

This trial was conducted with only one camera; it was directed towards the polycarbonate plate with the injection port. The experimental flow front was orthotropic and the permeability tensor was:

$$[\mathbf{K}]_{SS} = \begin{pmatrix} 4.33 & 0 \\ 0 & 5.87 \end{pmatrix} \cdot 10^{-11}\ m^2 \qquad [\mathbf{K}]_{WT} = \begin{pmatrix} 4.39 & 0 \\ 0 & 5.94 \end{pmatrix} \cdot 10^{-11}\ m^2$$

The fluid in the injection line was highly fluorescent but the impregnated fluid in the preform did not accumulate in high enough quantities for the fluorescence to be viewable by the naked eye nor by the camera. The fluid can still be seen to racetrack along the stitch lines in the recorded video. An example of this is displayed in Figures 4.19 and 4.20. These figures display only one quarter of the preform, this was done for magnifying the remaining portion of the preform.

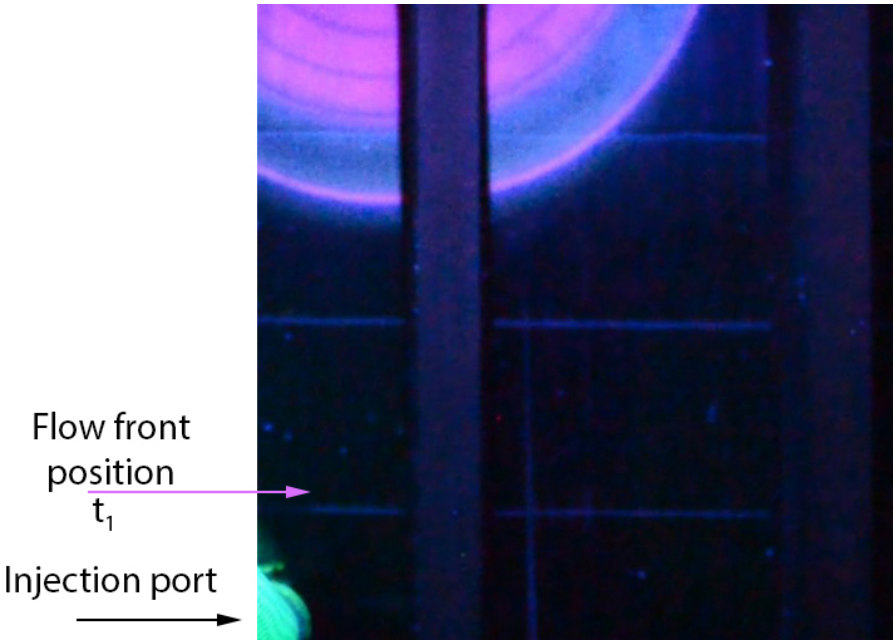

(a) Fluid at time t_1

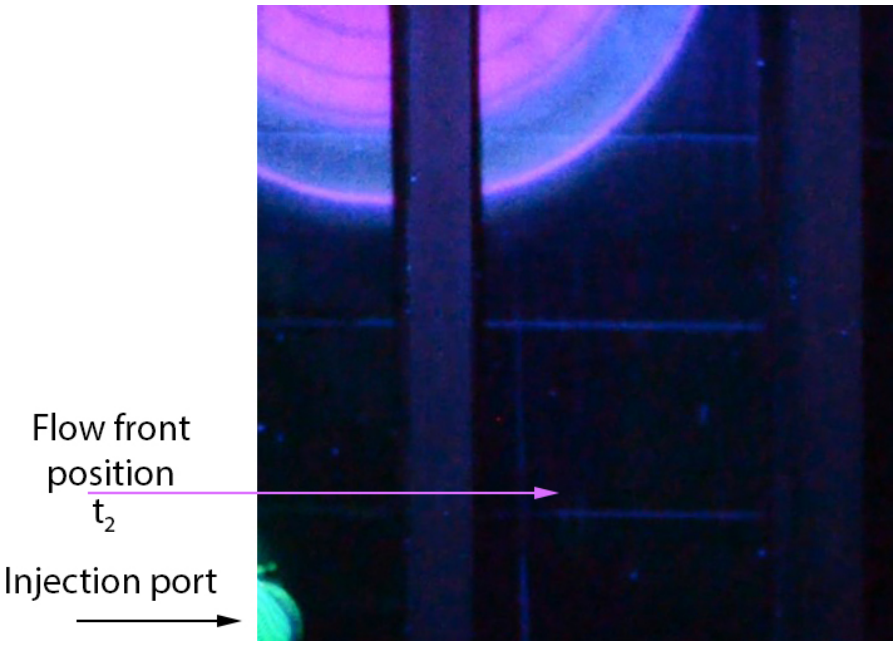

(b) Fluid at time $t_2 > t_1$

Figure 4.19: Fluid travelling along stitch line, Trial 10

Furthermore, Figure 4.20 displays the same quadrant except the apparatus is viewed under regular fluorescent light.

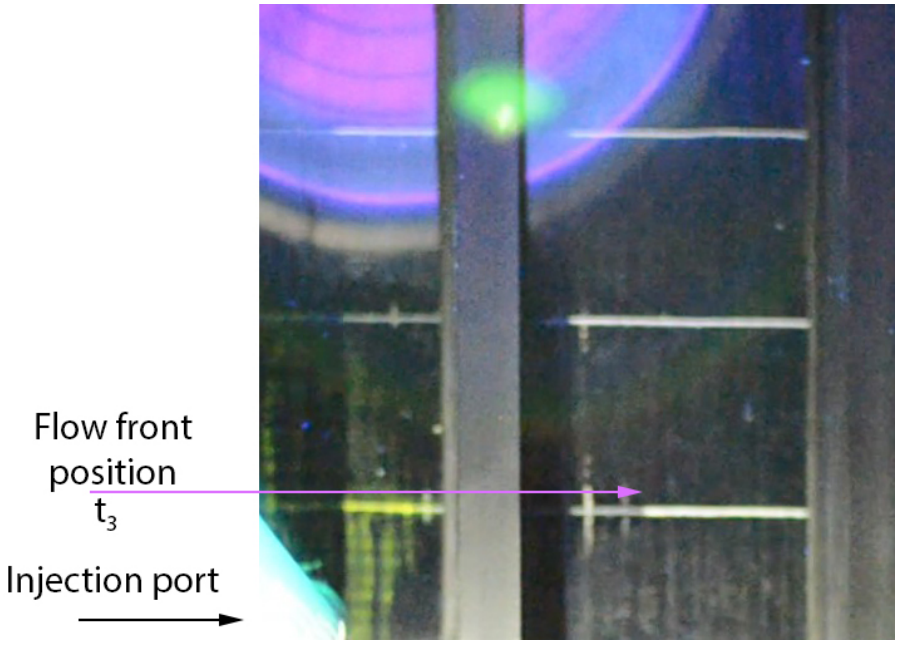

Figure 4.20: Fluid at time $t_3 > t_2$, Trial 10

While these figures outline the process of determining flow front position along one principal axis, the same procedure was done for the other principal axis.

4.11 Comparison of trials

To compare the permeability of different trials, maximum permeability values determined using Wika Tronic pressure transducer data were used along with video information from cameras when required. The decision to use data from the Wika Tronic pressure transducer was made as some trials exceeded the maximum pressure of the Setra Systems pressure transducer, hence no permeability value could be determined from the latter. The decision to use video data from cameras viewing the same side of the respective rig was done to compare permeabilities in the same plane. Trial 10 did not have data from this plane, hence no permeability value could be compared with all other trials. The comparable data is displayed in Figure 4.21:

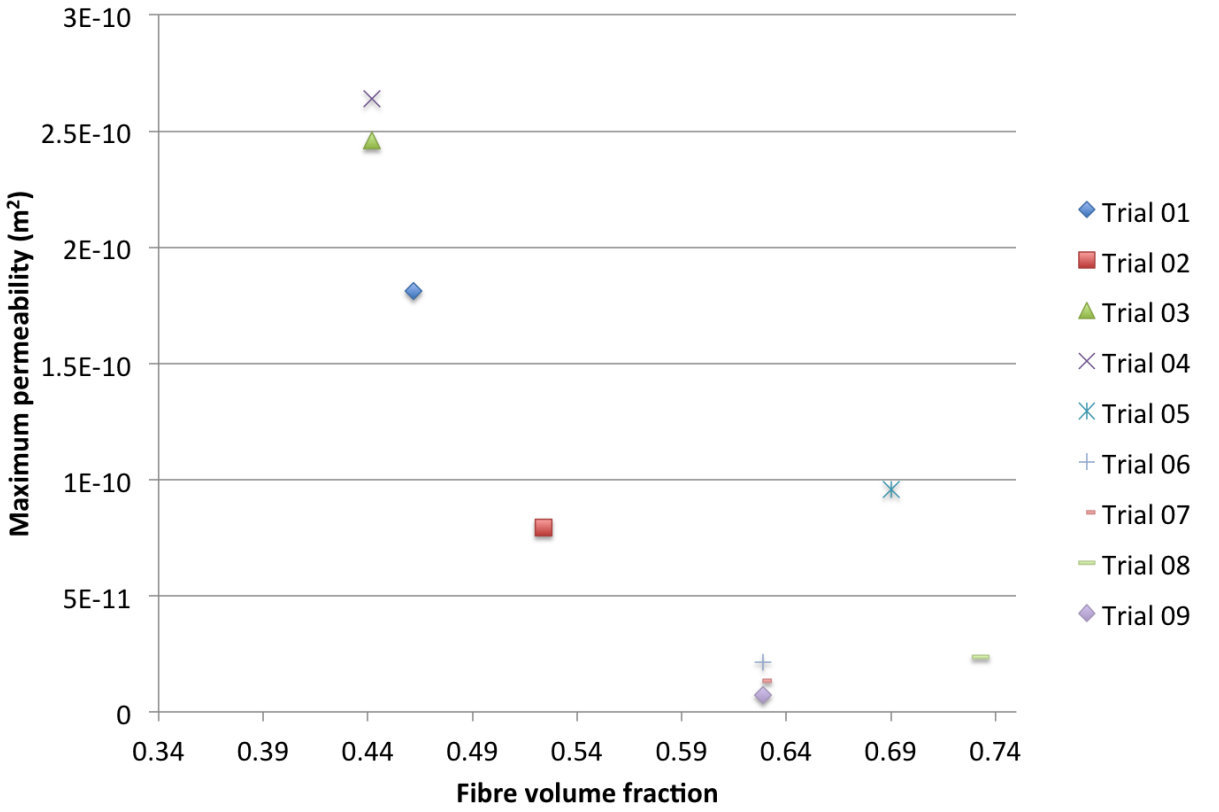

Figure 4.21: Maximum permeability as a function of fibre volume fraction for selected trials

As shown in Figure 4.21, the maximum permeability decreases non-linearly as a function of fibre volume fraction. Trial 05 was conducted using 2.43 mm spacers and is the only trial displayed in Figure 4.21 that used these spacers. Preform thickness would have an impact on the permeability due to extra travel distance of the fluid in the through-thickness direction required for the fluid to register on the camera.

While Figure 4.22 displays two issues with analysis of the results, the trends between experimental data and theoretical models are still quite similar and the precision of the data is quite comparable with the precision obtained by other authors who studied the permeability of non-stitched crimp fabrics [30].

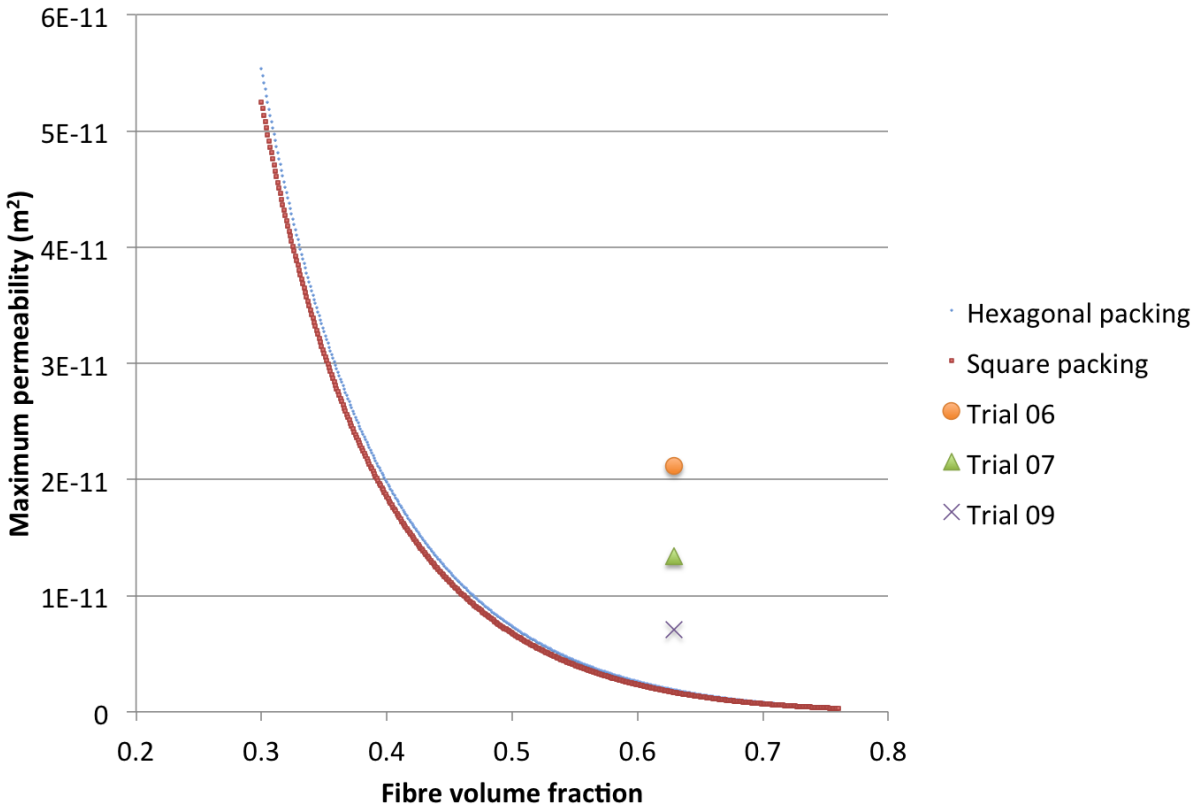

Figure 4.22: Maximum permeability as a function of fibre volume fraction for preforms featuring 6 layers of glass

One issue is the difficulty in predicting the permeability accurately from physical data. The series plotted as 'Hexagonal packing' and 'Square packing' are weighted arithmetic averages, derived from the equations described in Section 2.1. The weighting was done using the model predicting permeability of flow parallel to fibres proposed by Gutowski *et al.*, Equation 2.10, and the model for predicting permeability of flow perpendicular to fibres proposed by Gebart, Equation 2.13. These models were then averaged using Equation 2.14 which based the weighting factor for averaging on the number of layers in a preform. Since the number of layers and orientation of fibres in the layers are variables, directly comparing trials with different numbers of layers becomes inappropriate but the non-linear, negative trends are very similar. The variables chosen were $k_{\|} = 1.66$ and $k_{\|} = 1.78$ for the 'Hexagonal

packing' and 'Square packing' series, respectively. Also, the maximum fibre volume fraction were chosen as $v_{f,max} = \frac{\sqrt{3}\cdot\pi}{6}$ and $v_{f,max} = \frac{\pi}{4}$ for the 'Hexagonal packing' and 'Square packing' series, respectively. Both of these curves show very similar results for maximum permeability as a function of fibre volume fraction. In a process similar to the method proposed by Gebart, the curves are fitted to the experimental data with a change in effective fibre radius. Increasing the effective fibre radius by a multiple of approximately 3 results in a more accurate prediction, displayed in Figure 4.23. A similar alteration of $r_{f,\text{effective}} \approx 4 \cdot r_f$ was justified by Gebart due to the irregularities present in the cross-sectional area of the fibres [38].

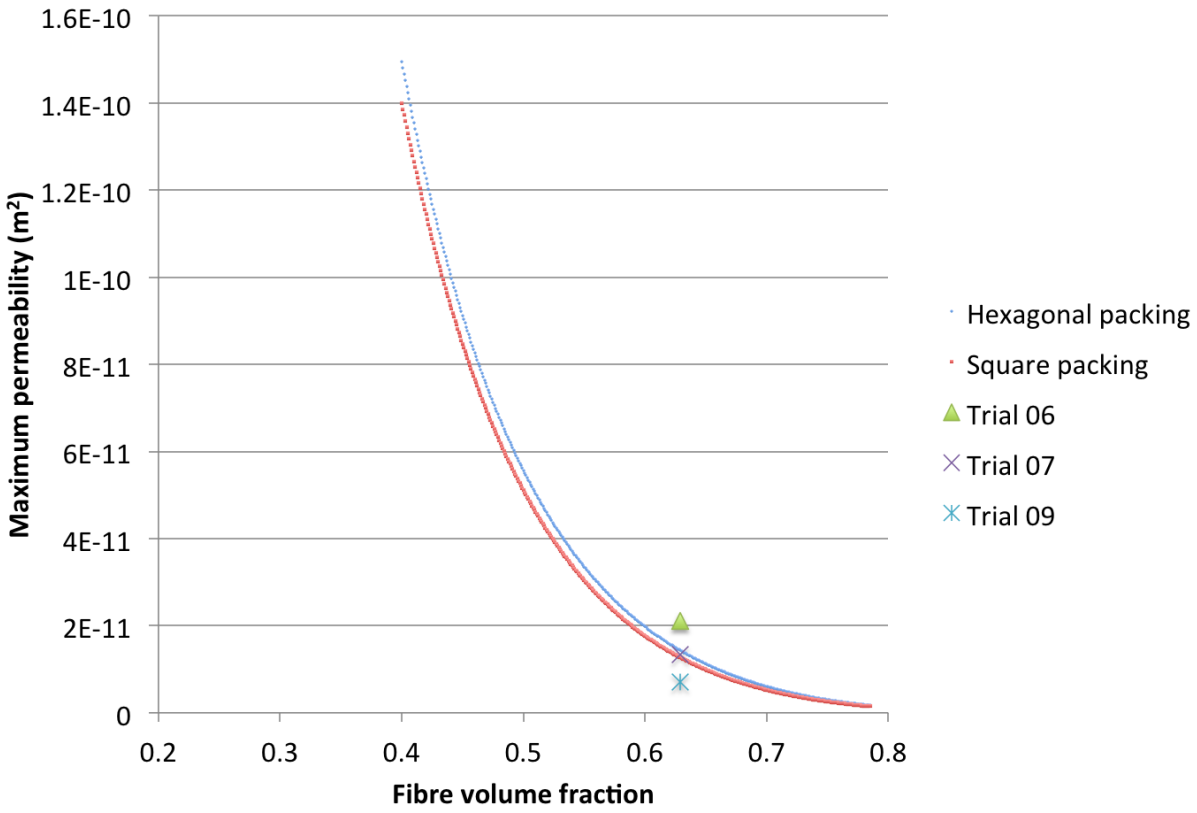

Figure 4.23: Maximum permeability as a function of fibre volume fraction for preforms featuring 6 layers of glass with $r_{f,\text{effective}} \approx 3 \cdot r_f$

Applying a fitting factor, i.e. increasing the fibre radius, the data presented in Figure 4.21 trends rather well with models which only account for basic heterogeneities present in the preforms. The basic model applied here does not account for stitch lines, inter-bundle channels, or transverse flow between successive layers yet still offers reasonable prediction capabilities.

Another issue is the difficulty caused by variability in permeability at a single fibre volume fraction. Trials 07 and 09 were performed with the same parameters, while Trial 06 was performed at a higher flow rate. The relative difference between the highest and lowest experimental permeability was 100%, while the relative difference between trials conducted with the same parameters was 61.6%. The large discrepancy between Trials 06 and 09 could be caused, in part, by the difference in inlet flow rates which has been shown to cause differences in measured permeability for unsaturated flow experiments [11]. The discrepancy between Trials 07 and 09 could be caused by the different proximity of the stitch line to the injection port. Trial 09 had the injection port centred over a stitch line, while Trial 07 had the injection port slightly off the line. Near the injection port the yarns were seen to displace locally on occasions, hence the stitching could reinforce the yarns, decreasing the recorded permeability for Trial 09. An example of the stitches close to the injection port is displayed in Figure 4.24a while Figure 4.24b displays the bowing of the fibres, also known as fibre wash. This fibre wash is a defect arising from the high pressure required to fill the high fibre volume fraction preform [55].



(a) Stitch centred over injection port (b) Injection port between two stitch lines

Figure 4.24: Yarn rearrangement near injection port

Even with these issues the reproducibility of these trials is very comparable to the reproducibility obtained by many other authors, when trying to determine permeability values experimentally. A recent study has documented the spread of permeability values for the same fabric and showed discrepancies in excess of 76% [30]. Hence, the spread of the experimental data presented here is reasonable.

By measure of thoroughness of filling, Trials 03, 07, and 09, appear to be most thoroughly wetted. Trial 03 was conducted with a preform which was not repeatedly compacted and the preform had the lowest fibre volume fraction tested, at 44.2%. The lower fibre volume fraction makes it reasonable for this trial to have better filling than other trials of non-compacted preforms. Trial 04 was conducted with similar parameters as Trial 03 and appeared to have wetted equally well in regions close to the injection port; however, Trial 04 had a significantly higher degree of orthotropy resulting in fluid reaching the boundary prior to large volumes of the preform being filled.

An interesting phenomenon occurred between Trials 03 and 04, the lower flow rate of Trial 03 resulted in a more isotropic flow front while the higher flow rate of Trial 04 resulted in a more orthotropic flow field. The higher flow rate likely did not permit the fluid to wick

along the fibres to the same degree as in the lower flow rate trial. This resulted in the fluid travelling preferentially in the inter-bundle channels, as well as in the voids created by the stitch lines. The stitch lines were major contributors to flow front orthotropy. Trials 07 and 09 were conducted with a similar set of parameters. One important parameter which has likely contributed to the higher thoroughness of filling was that these two trials had the lowest fibre volume fraction (62.9%) out of the preforms which were compacted in the compaction testing apparatus prior to injection. The other important parameter shared between these two trials was the lower flow rate, allowing more capillary action of the fibres to wick the fluid into the yarns rather than through the inter-bundle channels. The repeated compaction appears to have increased the uniformity of the fluid field but there were still significant issues related to the stitch lines causing volumes open for the fluid to flow through preferentially. A direct comparison of non-repeatedly compacted and repeatedly compacted preforms proved impossible due to the change in fibre volume fraction which arose from the compaction. The initial fibre volume fraction of a preform with the same number of layers as the non-repeatedly compacted preforms was too low for the preform to fill the mould cavity completely. Had trials been conducted in this manner the fluid would likely have caused flow induced mat-compression, and the fluid would have travelled underneath or above the preform rather than through it, hence no useful data would have been collected.

The compaction data also fits trends presented by other authors who studied different types of NCFs [52, 15, 51]. Specifically as the number of layers of fabric in a preform increases the amount of compaction pressure required to obtain the same fibre volume fraction increases. This phenomenon is displayed in Figure 4.25 which shows the 35th compaction cycle for preforms containing 4, 6, and 7 layers of glass. The compaction data for Trial 05 does not display the exact physical response as discussed in Section 4.5; however, the final value is accurate and follows the increasing trend.

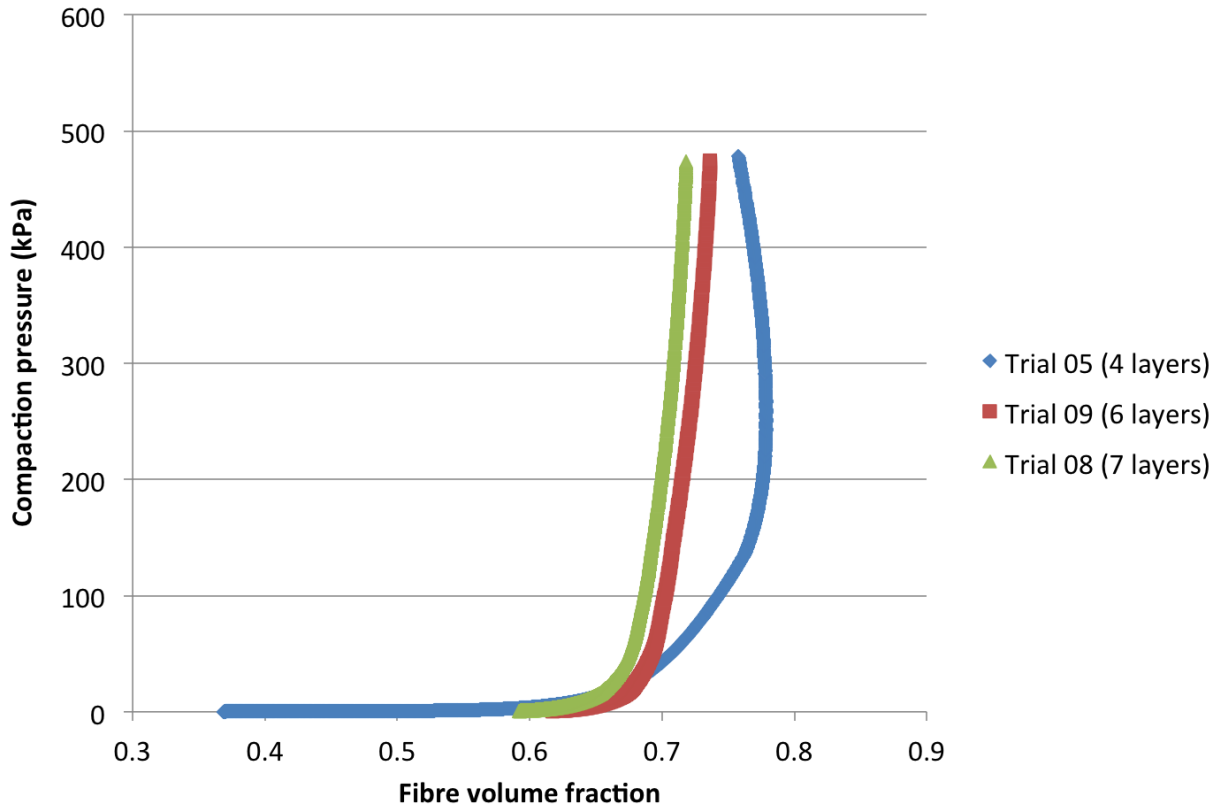

Figure 4.25: Compaction data for preforms manufactured using different numbers of layers

Figure 4.26 displays the spread of compaction data for preforms manufactured using the same number of fabric layers, $N_L = 6$. Some of the variation can be attributed to the slightly different areas of the preforms which arose during manufacturing. Again, these values show very similar trends to compaction data from the literature.

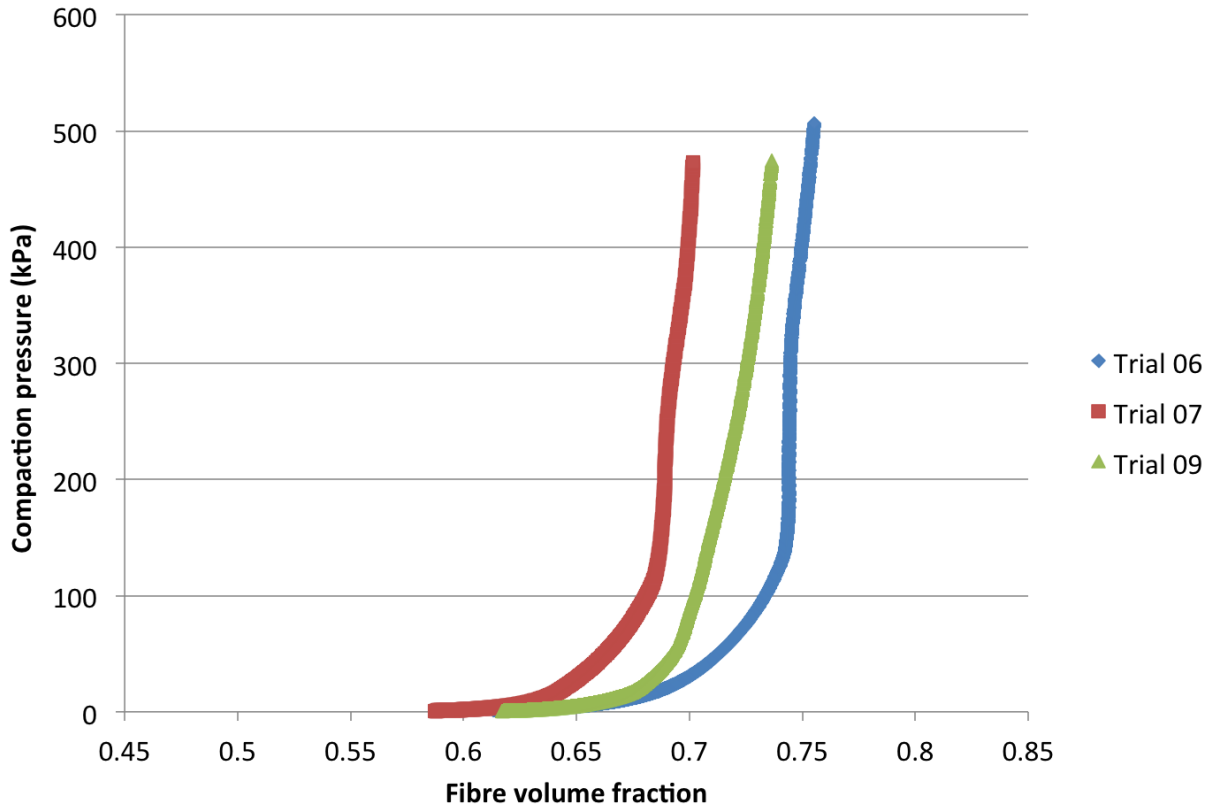

Figure 4.26: Compaction data for preforms manufactured using 6 layers

Chapter 5

Conclusion and Recommendations

The objective of this research was to determine the effect of through-thickness stitches on the LTM injection process, this was done by documenting and studying the flow of fluids through 3D NCF preforms during RTM manufacturing. The type of 3D NFC preform studied here requires through-thickness stitches to increase the handleability of the non-crimp yarns which compose the preform. The flow was studied experimentally using two apparatuses which simulated RTM moulds. Flow patterns were studied for preforms made from different fibres, different fibre volume fractions, and different degrees of preform consolidation. Through-thickness stitches were shown to create open channels in the preforms where fluid was able to flow preferentially. This effect altered the uniformity of the flow front dramatically; instead of a uniform 'elliptical' or circular flow front, the flow front featured regions of unsaturated fibres within the constructed shape. Consolidation of the fibres was shown to increase the uniformity of the surface yarns and decrease the local effects of stitching on the yarn spacing and void creation. Specifically, there was a large reduction in the volume of deformed yarns in the stitched zones. However, the significantly increased permeability in the stitched region of the consolidated fibres still caused issues with regard to the uniformity of the flow front. Fluorescent dye was effective in highlighting resin rich zones but not effective at documenting the flow front for high fibre volume fraction fabrics. This could, in part, be due to the ultraviolet lights used for activating the fluorescent properties of the dye, or other aspects of the experimental setup.

The experimental results were calculated to high precision and were in good agreement with simple models which didn't account for the heterogeneities present in this type of fabric. The experimental results showed a non-linear negative trend as a function of fibre volume fraction. The variability for trials conducted with the same parameters was approximately 60% which is very comparable to experimental work done on determining permeability of woven textiles a subset of crimp fabrics [30]. In that recent paper by Arbter, *et al.*, 16 different experimental procedures were applied to determine the permeability of a woven textile [30]. The physical properties of the woven textile were kept as constant as reasonably possible in an effort to minimize the effect of fabric variation. The results of that paper showed a maximum variability of 126% in the permeability value from trials conducted with the same experimental procedure and variability of an order of magnitude among all 16 different experimental procedures.

Future work is required towards determining if an optimal stitch density exists such that the fluid is able to wet the fibres fully while simultaneously minimizing the added mass of stitches. Experiments using 1D moulds should be performed for determining the effects of stitching on flow characteristics and permeability of saturated flows. Vacuum sealing the rigs and purging the entire system of air may also be considered. Investigation into different stitch densities and stitch types should also be done, aiming at improving epoxy saturation within yarns. Automated preform manufacturing will likely increase the repeatability of results significantly by decreasing the minor variations in stitch and preform geometries. This will also reduce the time required for preparing and performing experiments significantly. Also, stand-alone constant flow rate pumps would expedite the experimentation process.

Bibliography

[1] "AISI 1018 steel, cold drawn." http://matweb.com/search/DataSheet.aspx?MatGUID=3a9cc570fbb24d119f08db22a53e2421.

[2] "Aluminum 6061–T6; 6061–T651." http://matweb.com/search/DataSheet.aspx?MatGUID=1b8c06d0ca7c456694c7777d9e10be5b.

[3] "Titanium Ti–6Al–4V (Grade 5), annealed." http://matweb.com/search/DataSheet.aspx?MatGUID=a0655d261898456b958e5f825ae85390.

[4] Owens Corning, One Owens Corning Parkway, Toledo (Ohio), USA, 43659, *Product Information SE 1200 Type 30 Roving*, Mar. 2004.

[5] Toho Tenax America, Inc., 121 Cardiff Valley Road, Rockwood (Tennessee), USA, 37854-4134, *Tenax-J HTS40*, Dec. 2010.

[6] Tri-Tex, 1001 boul. Industriel, Saint-Eustache (Québec), Canada, J7R 6C3, *Marine System L–1911 (Temporary) Clear Laminating/Infusion System*, Nov. 2006.

[7] "Boeing: Commercial airplanes – 787 dreamliner – program fact sheet." http://www.boeing.com/commercial/787family/programfacts.html.

[8] "Boeing sets pace for composite usage in large civil aircraft." https://www.plasticstechnology.com/articles/boeing-sets-pace-for-composite-usage-in-large-civil-aircraft.

[9] "Airbus to start manufacturing parts for new a350 XWB in late 2009." http://www.engineeringnews.co.za/article/airbus-to-start-manufacturing-parts-for-new-a350-xwb-in-late-09-2009-05-11.

[10] R. Pan, Z. Liang, C. Zhang, and B. Wang, "Statistical characterization of fiber permeability for composite manufacturing," *Polymer Composites*, vol. 21, no. 6, pp. 996–1006, 2000.

[11] T. M. Kruckenberg and R. Paton, *Resin Transfer Moulding for Aerospace Structures*. Kluwer Academic, 1998.

[12] A. P. Mouritz, M. K. Bannister, P. J. Falzon, and K. H. Leong, "Review of applications for advanced three-dimensional fibre textile composites," *Composites Part A: Applied Science and Manufacturing*, vol. 30, no. 12, pp. 1445–1461, 1999.

[13] M. Yildiz, N. G. Ozdemir, G. Bektas, C. J. Keulen, T. Boz, E. F. Sengun, C. Ozturk, Y. Z. Menceloglu, and A. Suleman, "An experimental study on the process monitoring of resin transfer molded composite structures using fiber optic sensors," *Journal of Manufacturing Science and Engineering*, vol. 134, no. 4, 2012.

[14] P. Šimáček and S. G. Advani, "Desirable features in mold filling simulations for liquid composite molding processes," *Polymer Composites*, vol. 25, no. 4, pp. 355–367, 2004.

[15] F. Robitaille and R. Gauvin, "Compaction of textile reinforcements for composites manufacturing. II: Compaction and relaxation of dry and H_2O-saturated woven reinforcements," *Polymer Composites*, vol. 19, no. 5, pp. 543–557, 1998.

[16] M. Matsudaira, Y. Tan, and Y. Kondo, "The effect of fibre cross-sectional shape on fabric mechanical properties and handle," *Journal of the Textile Institute*, vol. 84, no. 3, pp. 376–386, 1993.

[17] K. Dransfield, C. Baillie, and Y. Mai, "Improving the delamination resistance of CFRP by stitching – a review," *Composites Science and Technology*, vol. 50, no. 3, pp. 305–317, 1994.

[18] H. Talvensaari, E. Ladstätter, and W. Billinger, "Permeability of stitched preform packages," *Composite Structures*, vol. 71, no. 3–4, pp. 371–377, 2005.

[19] H. Darcy, *Les Fontaines Publiques de la Ville de Dijon*. Paris, France: Dalmont, 1856.

[20] P. M. Adler, *Porous Media: Geometry and transports*. Boston, Massachusetts: Butterworth/Heinemann, 1992.

[21] R. S. Parnas, K. M. Flynn, and M. E. Dal-Favero, "A permeability database for composites manufacturing," *Polymer Composites*, vol. 18, no. 5, pp. 623–633, 1997.

[22] R. Parnas, J. Howard, T. Luce, and S. Advani, "Permeability characterization. part 1: A proposed standard reference fabric for permeability," *Polymer Composites*, vol. 16, no. 6, pp. 429–445, 1995.

[23] R. Gauvin, A. Kerachni, and B. Fisa, "Variation of Mat Surface Density and Its Effect on Permeability Evaluation for RTM Modelling," *Journal of Reinforced Plastics and Composites*, vol. 13, pp. 371–383, Apr. 1994.

[24] T. A. K. Sadiq, S. G. Advani, and R. S. Parnas, "Experimental Investigation of Transverse Flow Through Aligned Cylinders," *International Journal of Multiphase Flow*, vol. 21, no. 5, pp. 755–774, 1995.

[25] L. Trevino, K. Rupel, W. B. Young, M. J. Liou, and L. J. Lee, "Analysis of resin injection molding in molds with preplaced fiber mats. i: Permeability and compressibility measurements," *Polymer Composites*, vol. 12, no. 1, pp. 20–29, 1991.

[26] A. W. Chan, D. E. Larive, and R. J. Morgan, "Anisotropic permeability of fiber preforms: Constant flow rate measurement," *Journal of Composite Materials*, vol. 27, no. 10, pp. 996–1008, 1993.

[27] A. W. Chan and S.-T. Hwang, "Anisotropic in-plane permeability of fabric media," *Polymer Engineering & Science*, vol. 31, no. 16, pp. 1233–1239, 1991.

[28] K. L. Adams, W. B. Russel, and L. Rebenfeld, "Radial penetration of a viscous liquid into a planar anisotropic porous medium," *International Journal of Multiphase Flow*, vol. 14, no. 2, pp. 203–215, 1988.

[29] T. Lundström, "The permeability of non-crimp stitched fabrics," *Composites Part A: Applied Science and Manufacturing*, vol. 31, no. 12, pp. 1345–1353, 2000.

[30] R. Arbter, J. Beraud, C. Binetruy, L. Bizet, J. Bréard, S. Comas-Cardona, C. Demaria, a. Endruweit, P. Ermanni, F. Gommer, S. Hasanovic, P. Henrat, F. Klunker, B. Laine, S. Lavanchy, S. Lomov, a. Long, V. Michaud, G. Morren, E. Ruiz, H. Sol, F. Trochu, B. Verleye, M. Wietgrefe, W. Wu, and G. Ziegmann, "Experimental determination of the permeability of textiles: A benchmark exercise," *Composites Part A: Applied Science and Manufacturing*, vol. 42, pp. 1157–1168, Sept. 2011.

[31] N. US Department of Commerce, "SRD numbering system." SRD Numbering System.

[32] P. C. Carman, "Permeability of saturated sands, soils and clays," *The Journal of Agricultural Science*, vol. 29, pp. 262–273, 1939.

[33] T. G. Gutowski, Z. Cai, S. Bauer, D. Boucher, J. Kingery, and S. Wineman, "Consolidation experiments for laminate composites," *Journal of Composite Materials*, vol. 21, no. 7, pp. 650–669, 1987.

[34] T. G. Gutowski, T. Morigaki, and Z. Cai, "The consolidation of laminate composites," *Journal of Composite Materials*, vol. 21, no. 2, pp. 172–188, 1987.

[35] T. G. Gutowski, S. Wineman, and Z. Cai, "Applications of the resin flow/fibre deformation model," in *31st International SAMPE Symposium and Exhibition*, Apr. 1986.

[36] L. Skartsis, J. Kardos, and B. Khomami, "Resin flow through fiber beds during composite manufacturing processes. part i: Review of newtonian flow through fiber beds," *Polymer Engineering & Science*, vol. 32, no. 4, pp. 221–230, 1992.

[37] L. Skartsis, J. Kardos, and B. Khomami, "Resin flow through fiber beds during composite manufacturing processes. part ii: Numerical and experimental studies of newtonian

flow through ideal and actual fiber beds," *Polymer Engineering & Science*, vol. 32, no. 4, pp. 231–239, 1992.

[38] B. Gebart, "Permeability of unidirectional reinforcements for rtm," *Journal of Composite Materials*, vol. 26, no. 8, pp. 1100–1133, 1992.

[39] V. M. Calado and S. G. Advani, "Effective average permeability of multi-layer preforms in resin transfer molding," *Composites Science and Technology*, vol. 56, no. 5, pp. 519–531, 1996.

[40] K. Shin, Y. Song, and J. Youn, "Radial flow advancement in multi-layered preform for resin transfer molding," *Korea-Australia Rheology Journal*, vol. 18, no. 4, pp. 217–224, 2006.

[41] Y. Wei and J. Zhang, "Characterization of microstructure in stitched unidirectional composite laminates," *Composites Part A: Applied Science and Manufacturing*, vol. 39, no. 5, pp. 815–824, 2008.

[42] V. Yavari and M. Kadivar, "Fiber volume fraction around stitch in ncf composites," *Procedia Engineering*, vol. 14, pp. 3191–3198, 2011.

[43] V. Koissin, A. Ruopp, S. Lomov, I. Verpoest, V. Witzel, and K. Drechsler, "On-surface fibre-free zones and irregularity of piercing pattern in structurally stitched ncf preforms," *Advanced composites letters*, vol. 15, no. 3, pp. 81–88, 2006.

[44] S. Drapier, A. Pagot, A. Vautrin, and P. Henrat, "Influence of the stitching density on the transverse permeability of non-crimped new concept (nc2) multiaxial reinforcements: measurements and predictions," *Composites Science and Technology*, vol. 62, no. 15, pp. 1979–1991, 2002.

[45] F. Robitaille, A. Long, and C. Rudd, "Permeability prediction for industrial preforms," *Plastics, Rubber and Composites*, vol. 31, no. 6, pp. 238–248, 2002.

[46] C. M. van Wyk, "20–note on the compressibility of wool," *Journal of the Textile Institute Transactions*, vol. 37, no. 12, pp. T285–T292, 1946.

[47] T. G. Gutowski, "Resin flow/fiber deformation model for composites," *SAMPE Quarterly*, vol. 16, pp. 58–64, 1985.

[48] Z. Cai and T. Gutowski, "The 3-d deformation behavior of a lubricated fiber bundle," *Journal of Composite Materials*, vol. 26, no. 8, pp. 1207–1237, 1992.

[49] P. Šimáček and V. M. Karbhari, "Notes on the modeling of preform compaction: I -micromechanics at the fiber bundle level," *Journal of Reinforced Plastics and Composites*, vol. 15, no. 1, pp. 86–122, 1996.

[50] R. Gauvin, Y. Lemenn, P. Clerk, and F. Trochu, "Compaction and creep behavior of glass reinforcement for liquid composites molding," in *Proceedings of the 10th ASM Conference*, Nov. 1994.

[51] F. Robitaille and R. Gauvin, "Compaction of textile reinforcements for composites manufacturing. III: Reorganization of the fiber network," *Polymer Composites*, vol. 20, no. 1, pp. 48–61, 1999.

[52] F. Robitaille and R. Gauvin, "Compaction of textile reinforcements for composites manufacturing. I: Review of experimental results," *Polymer Composites*, vol. 19, no. 2, pp. 198–216, 1998.

[53] Hy-spec Hydraulik, *Hy-spec Hydraulik catalogue*, Jan. 2008.

[54] C. Products, "Pure silicone fluids–clearco products," Apr. 2012.

[55] K. D. Potter, B. Khan, M. Wisnom, T. Bell, and J. Stevens, "Variability, fibre waviness and misalignment in the determination of the properties of composite materials and structures," *Composites Part A: Applied Science and Manufacturing*, vol. 39, pp. 1343–1354, Sept. 2008.

Appendicies

Appendix A

Raw video data

When appropriate the elapsed time is represented by (minutes : seconds : milliseconds).

Trial 01

Camera directed toward polycarbonate plate without injection port

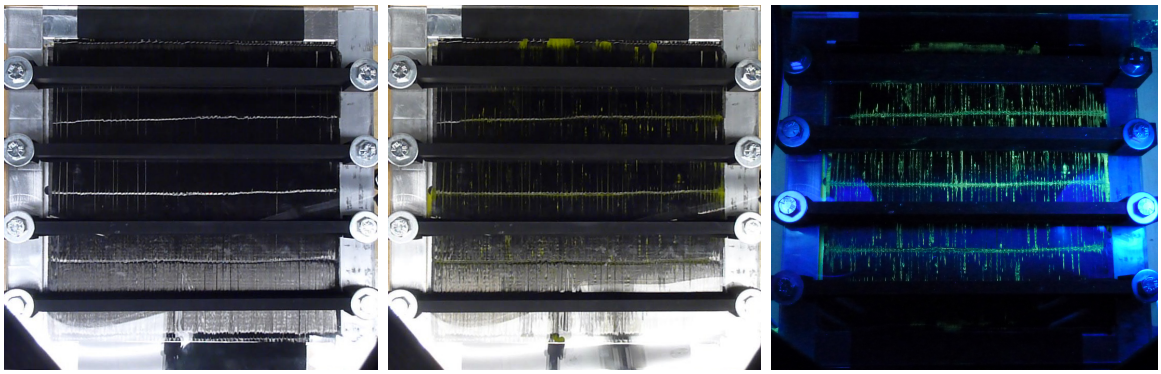

(a) Prior to test (b) End of test (c) End of test with UV lights

Figure 5.1: Filling pattern, Trial 01

Trial 02

Camera directed toward polycarbonate plate without injection port

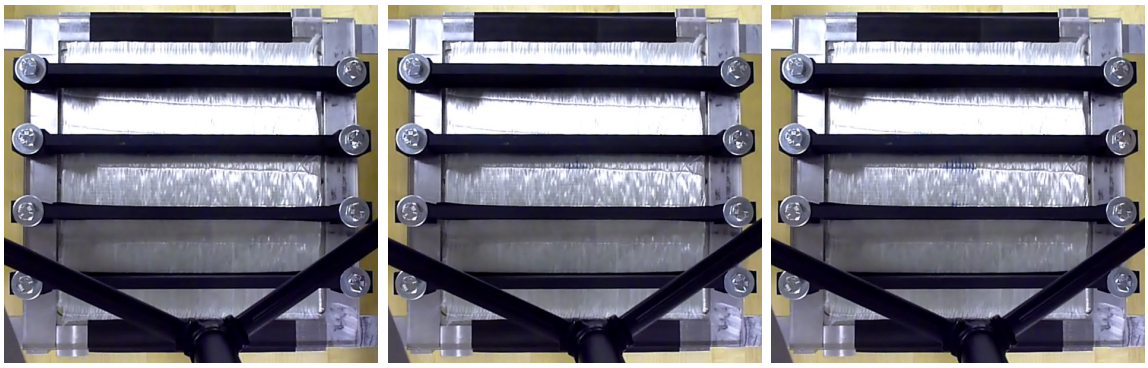

(a) 00:00:000 (b) 00:09:667 (c) 00:12:767

Figure 5.2: Filling pattern, Trial 02

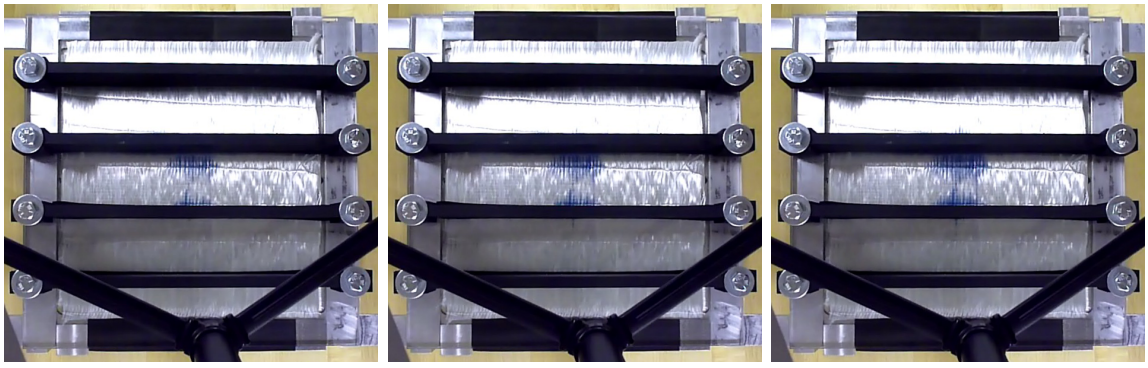

(a) 00:18:667 (b) 00:21:467 (c) 00:24:334

Figure 5.3: Filling pattern, Trial 02

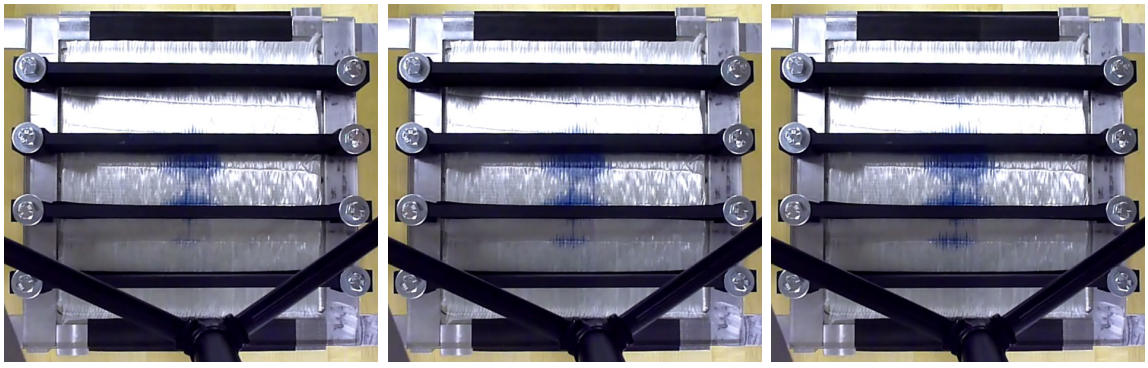

(a) 00:26:267 (b) 00:29:167 (c) 00:31:667

Figure 5.4: Filling pattern, Trial 02

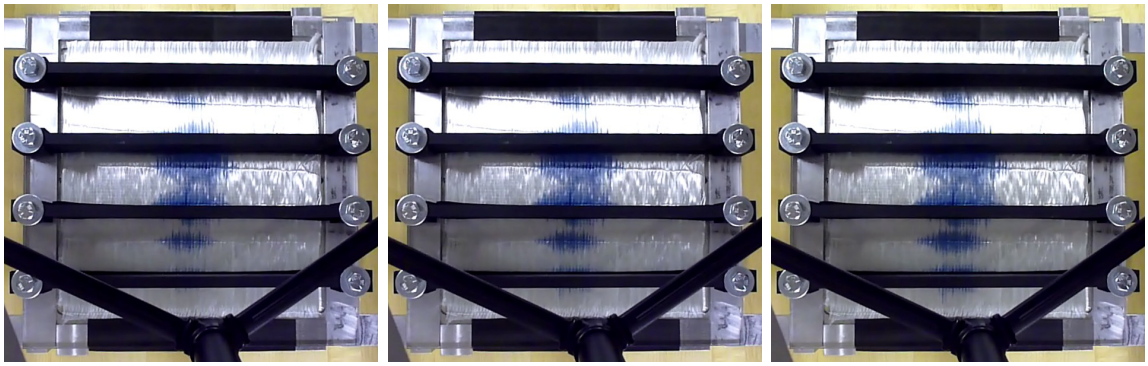

(a) 00:35:900 (b) 00:39:567 (c) 00:43:867

Figure 5.5: Filling pattern, Trial 02

Trial 03

Camera directed toward polycarbonate plate without injection port

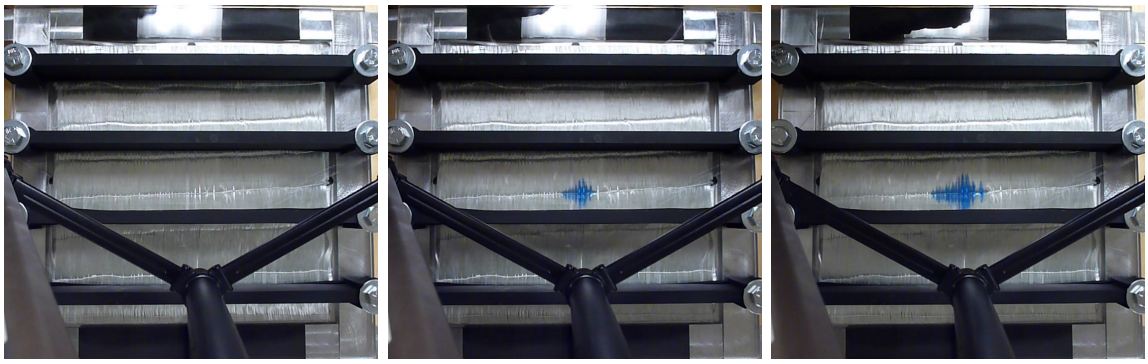

(a) 00:00:000 (b) 00:14:000 (c) 00:38:000

Figure 5.6: Filling pattern, Trial 03

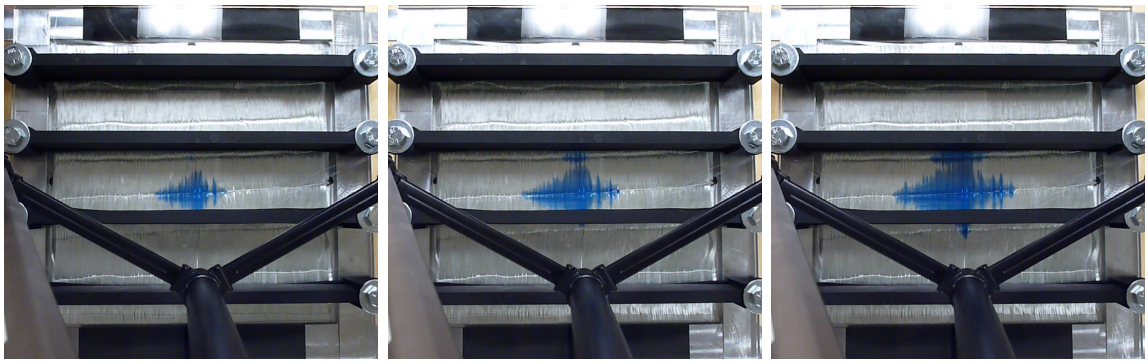

(a) 01:00:000 (b) 01:51:000 (c) 02:45:000

Figure 5.7: Filling pattern, Trial 03

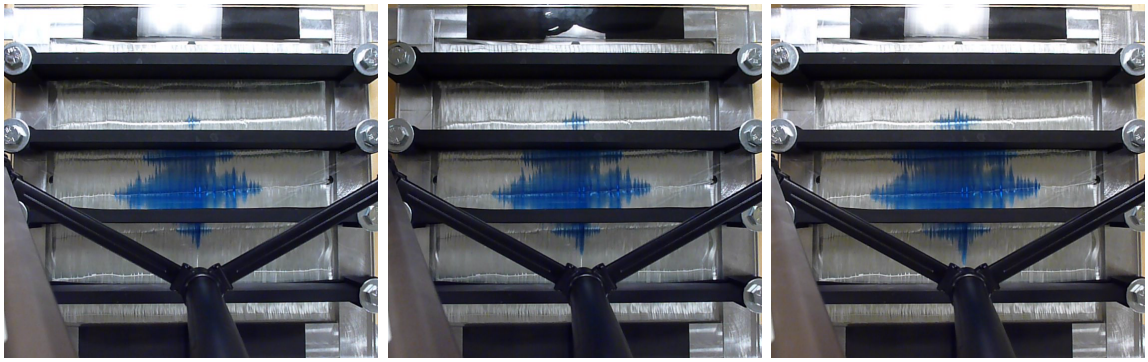

(a) 03:34:000 (b) 03:54:000 (c) 04:23:000

Figure 5.8: Filling pattern, Trial 03

Trial 04

Camera directed toward polycarbonate plate without injection port

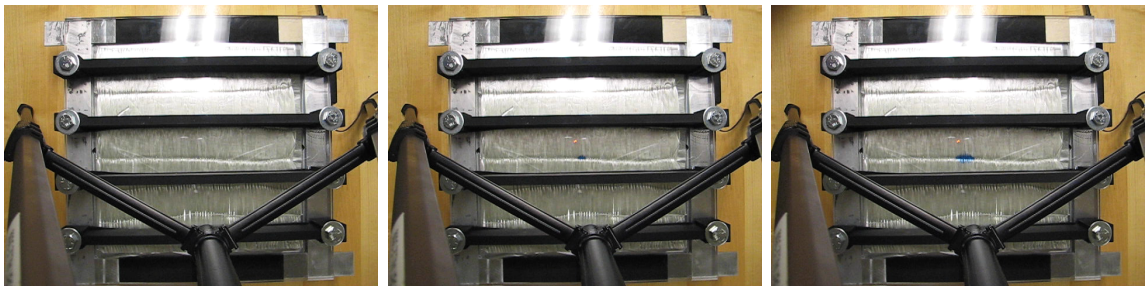

(a) 00:00:000 (b) 00:02:960 (c) 00:06:920

Figure 5.9: Filling pattern, Trial 04

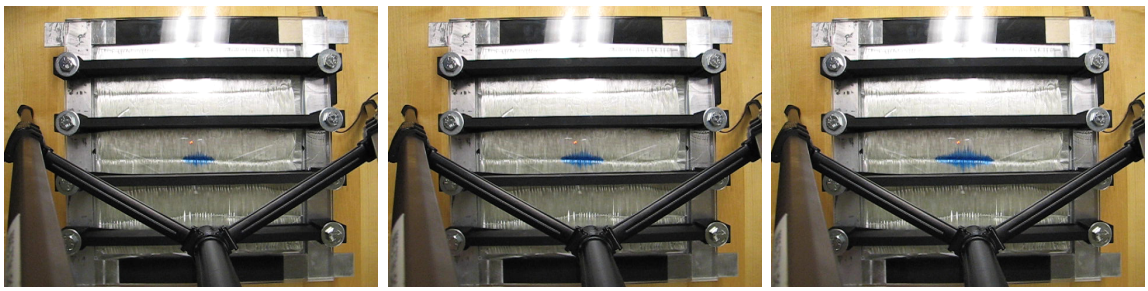

(a) 00:10:170 (b) 00:13:160 (c) 00:17:930

Figure 5.10: Filling pattern, Trial 04

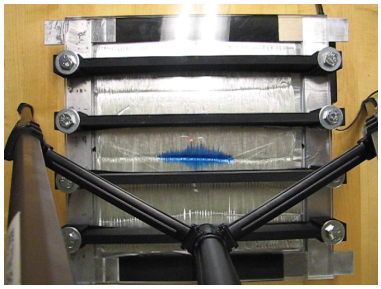
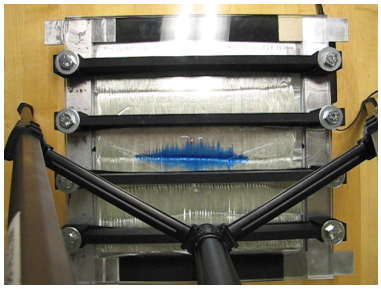
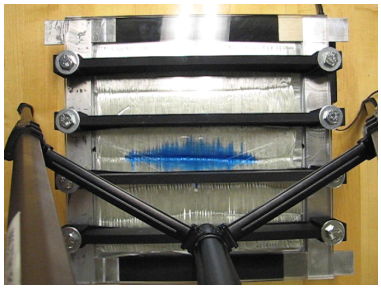

(a) 00:22:950 (b) 00:31:960 (c) 00:37:030

Figure 5.11: Filling pattern, Trial 04

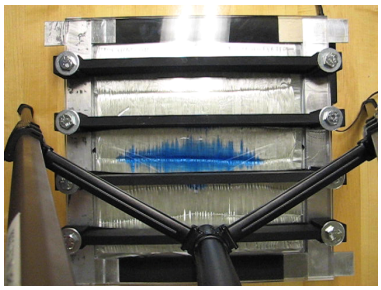
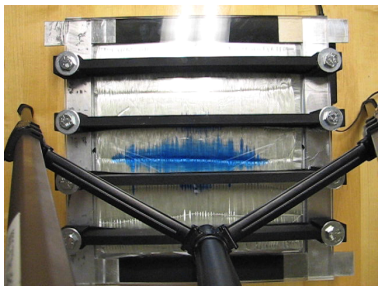
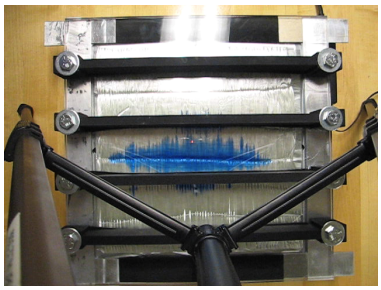

(a) 00:41:060 (b) 00:44:070 (c) 00:46:160

Figure 5.12: Filling pattern, Trial 04

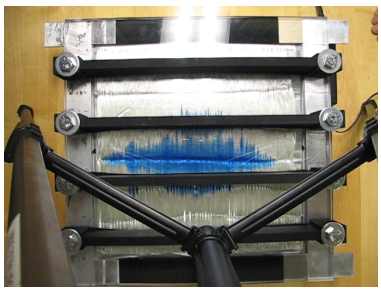

(a) 00:51:080

Figure 5.13: Filling pattern, Trial 04

Trial 05

Camera directed toward polycarbonate plate without injection port

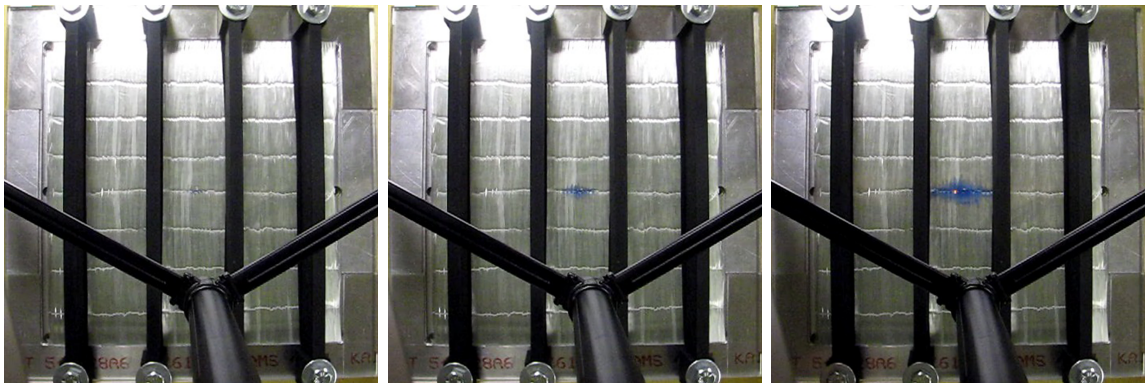

(a) 00:00:000 (b) 00:05:000 (c) 00:26:000

Figure 5.14: Filling pattern, Trial 05

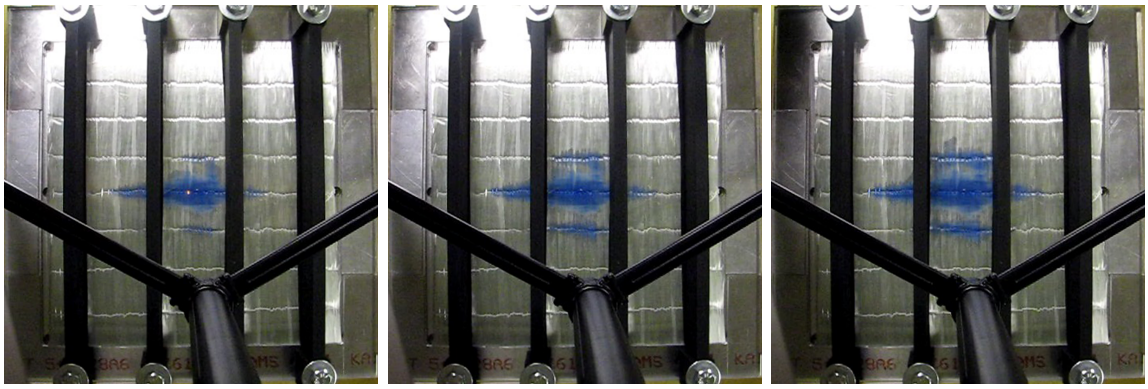

(a) 00:48:000 (b) 00:52:000 (c) 00:56:000

Figure 5.15: Filling pattern, Trial 05

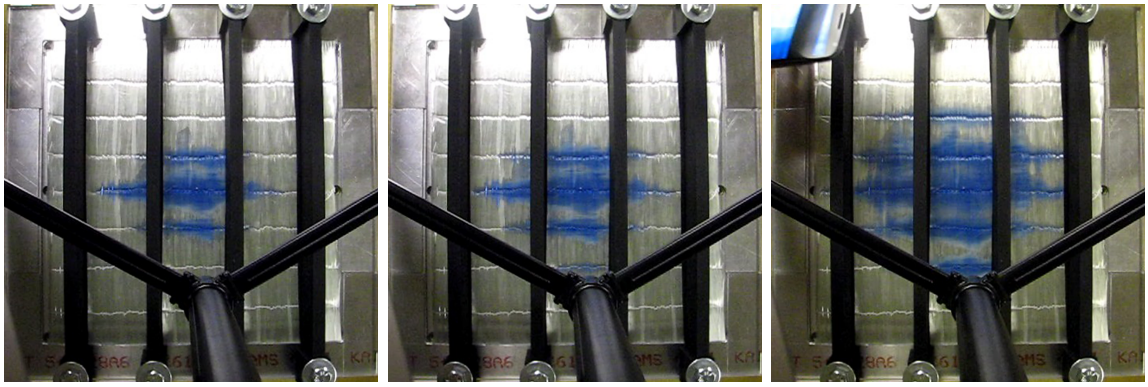

(a) 01:00:000 (b) 01:07:000 (c) 01:38:000

Figure 5.16: Filling pattern, Trial 05

Trial 06

Camera directed toward polycarbonate plate without injection port

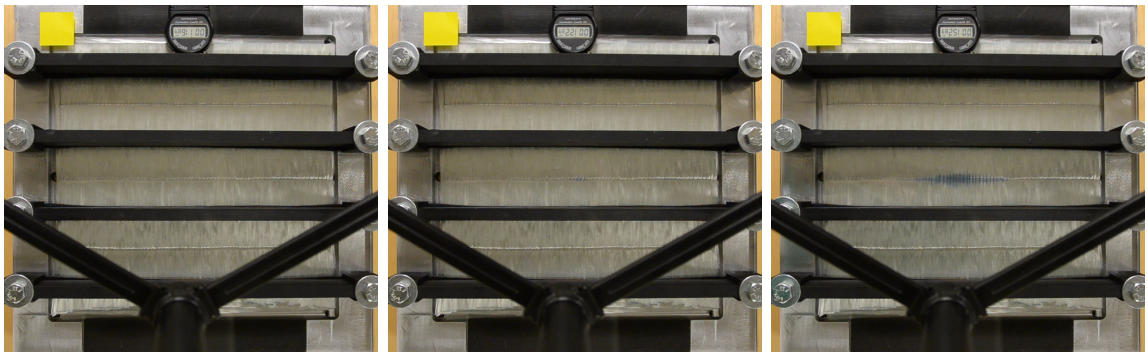

(a) 00:00:000 (b) 00:20:020 (c) 00:35:536

Figure 5.17: Filling pattern, Trial 06

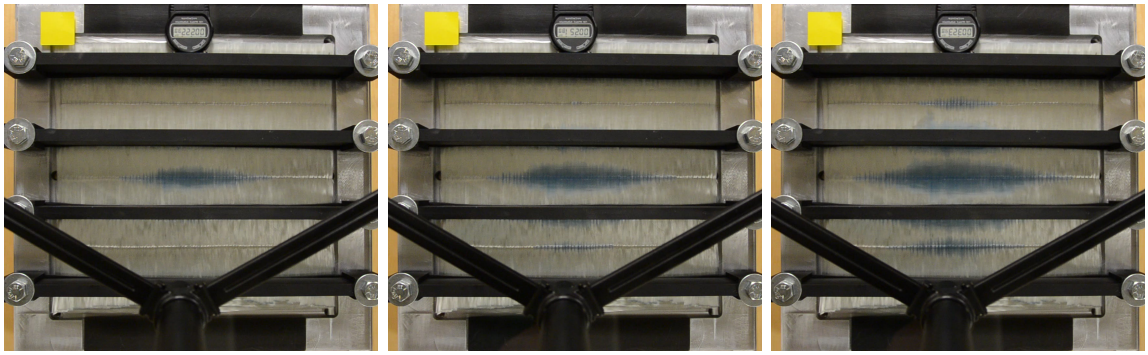

(a) 01:05:065 (b) 01:34:595 (c) 02:06:126

Figure 5.18: Filling pattern, Trial 06

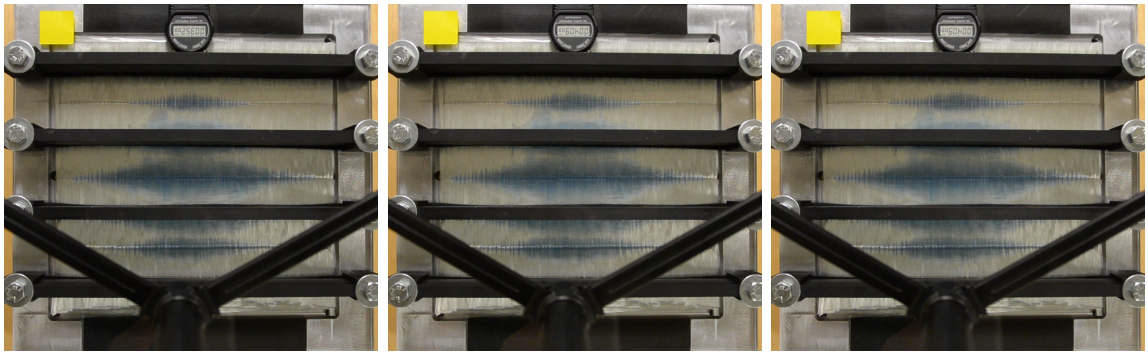

(a) 02:36:156 (b) 02:52:172 (c) 03:09:690

Figure 5.19: Filling pattern, Trial 06

Trial 07

Camera directed toward polycarbonate plate without injection port

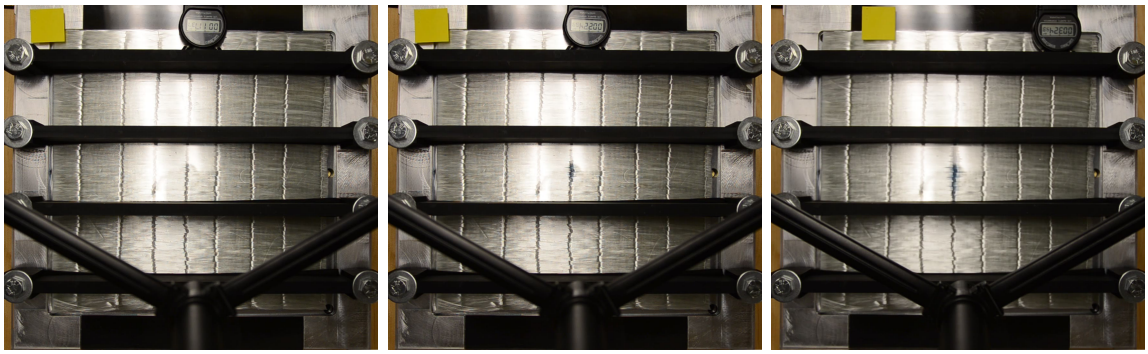

(a) 00:00:000 (b) 01:31:700 (c) 02:31:510

Figure 5.20: Filling pattern, Trial 07

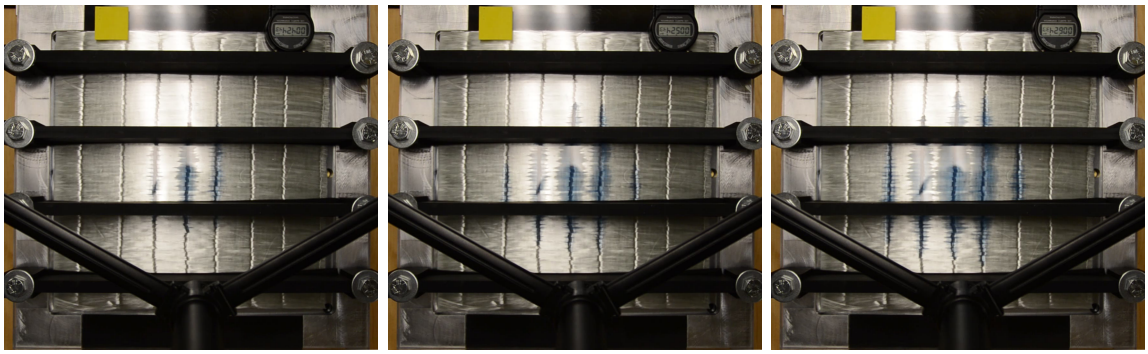

(a) 03:31:486 (b) 04:31:421 (c) 05:31:398

Figure 5.21: Filling pattern, Trial 07

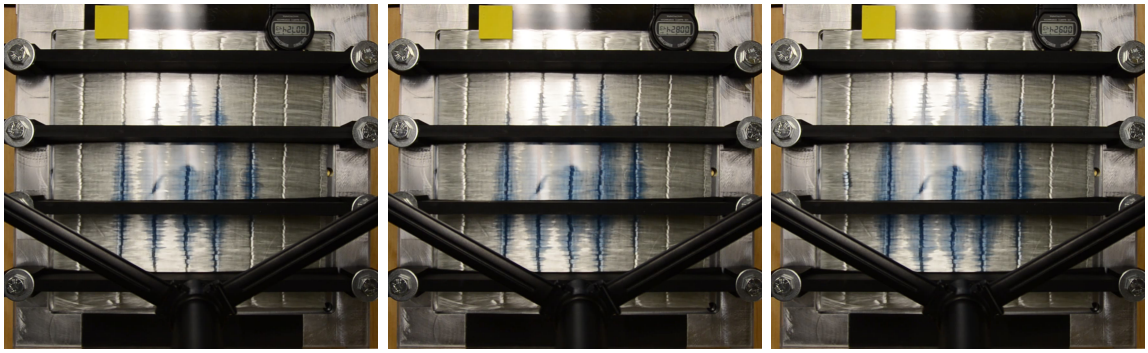

(a) 06:31:416 (b) 07:31:434 (c) 08:31:411

Figure 5.22: Filling pattern, Trial 07

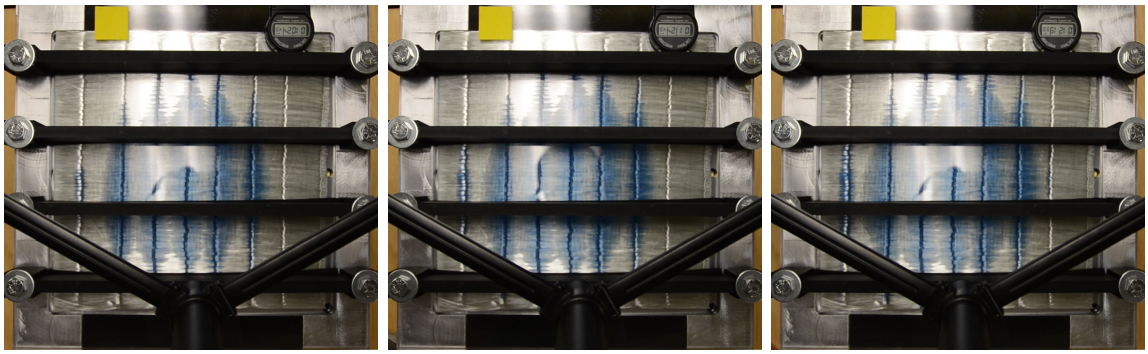

(a) 09:31:429 (b) 10:31:448 (c) 11:26:002

Figure 5.23: Filling pattern, Trial 07

Trial 08

Camera directed toward polycarbonate plate with injection port

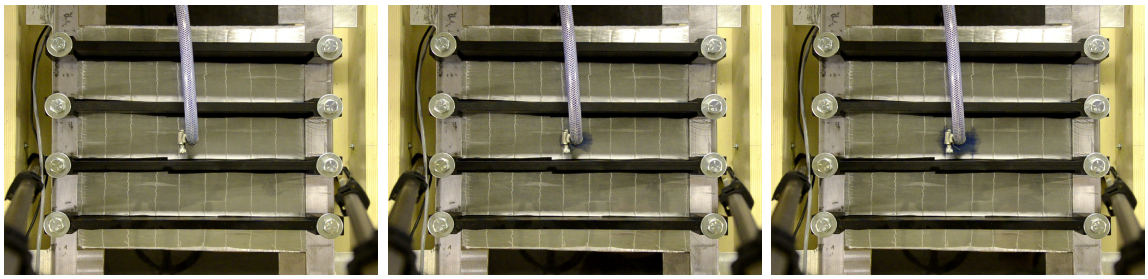

(a) 00:00:00 (b) 03:56:396 (c) 04:41:816

Figure 5.24: Filling pattern, Trial 08

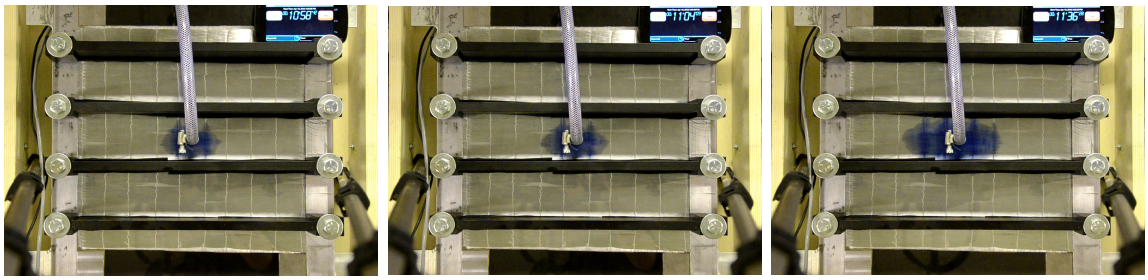

(a) 05:00:043 (b) 05:06:065 (c) 05:38:180

Figure 5.25: Filling pattern, Trial 08

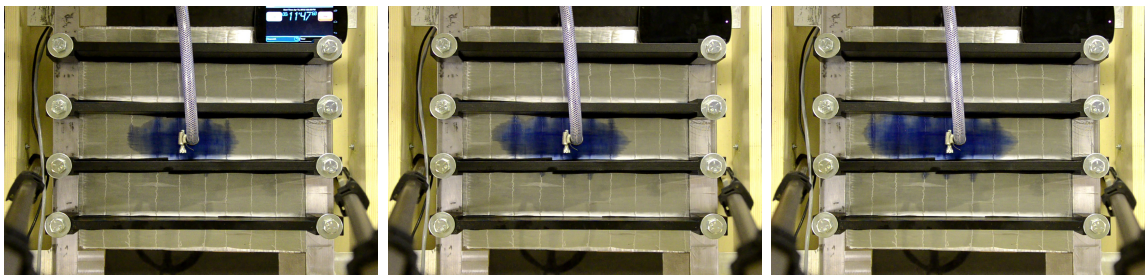

(a) 05:49:483 (b) 06:24:685 (c) 07:01:430

Figure 5.26: Filling pattern, Trial 08

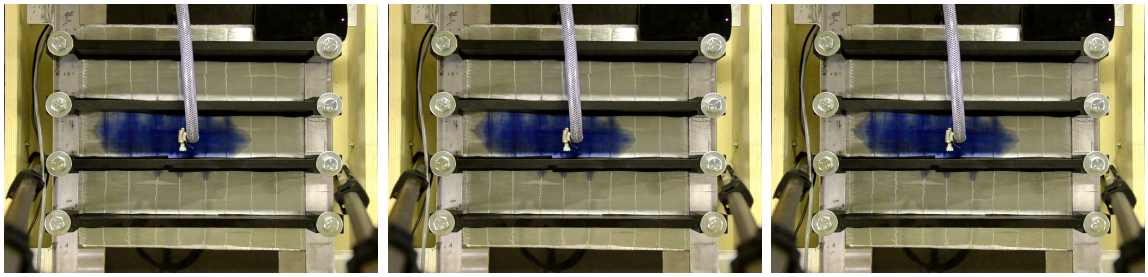

(a) 07:08:770 (b) 07:13:984 (c) 07:19:656

Figure 5.27: Filling pattern, Trial 08

Camera directed toward polycarbonate plate without injection port

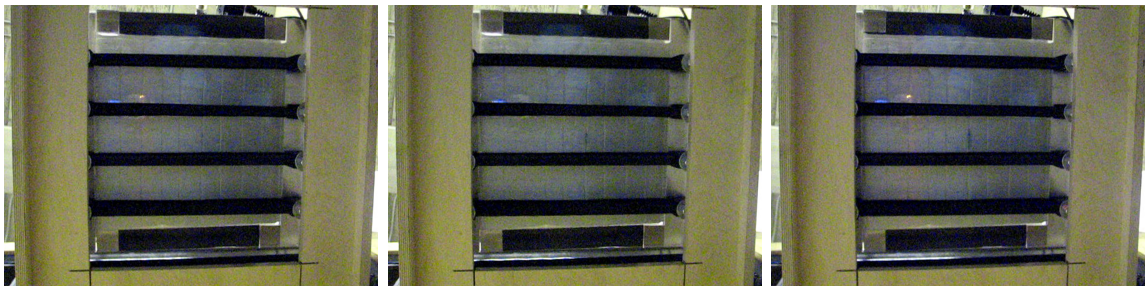

(a) 00:00:00 (b) 04:46:814 (c) 04:55:514

Figure 5.28: Filling pattern, Trial 08

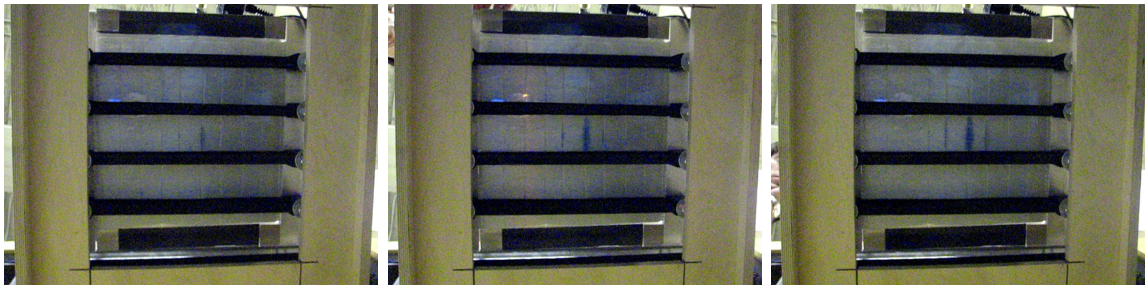

(a) 04:59:180 (b) 05:29:380 (c) 05:39:180

Figure 5.29: Filling pattern, Trial 08

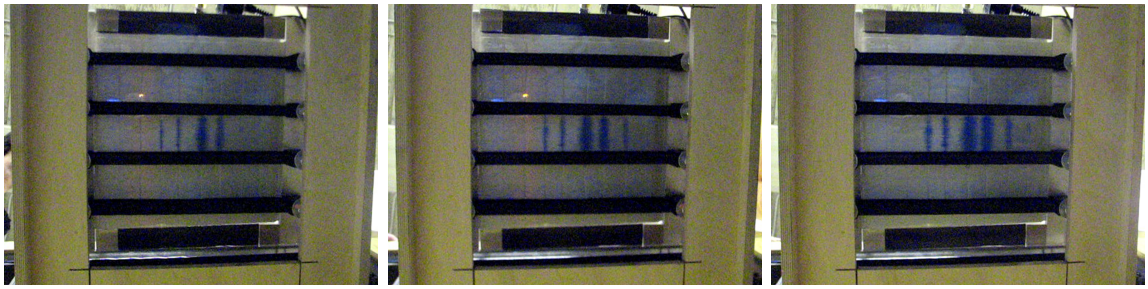

(a) 06:12:646 (b) 06:41:379 (c) 07:10:879

Figure 5.30: Filling pattern, Trial 08

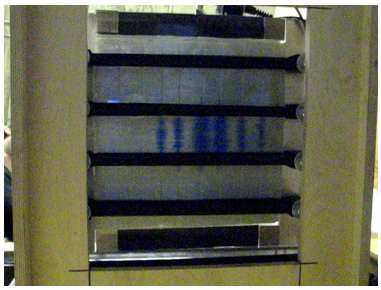

(a) 07:54:045

Figure 5.31: Filling pattern, Trial 08

Trial 09

Camera directed toward polycarbonate plate with injection port

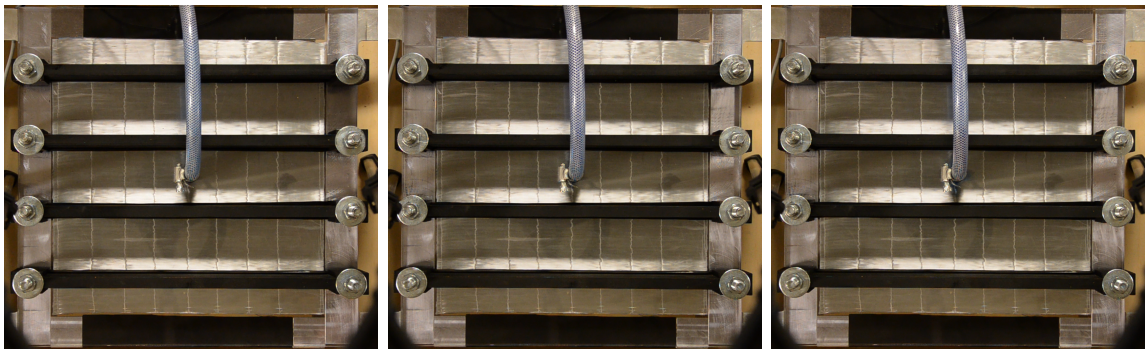

(a) 00:00:000 (b) 01:53:367 (c) 08:13:367

Figure 5.32: Filling pattern, Trial 09

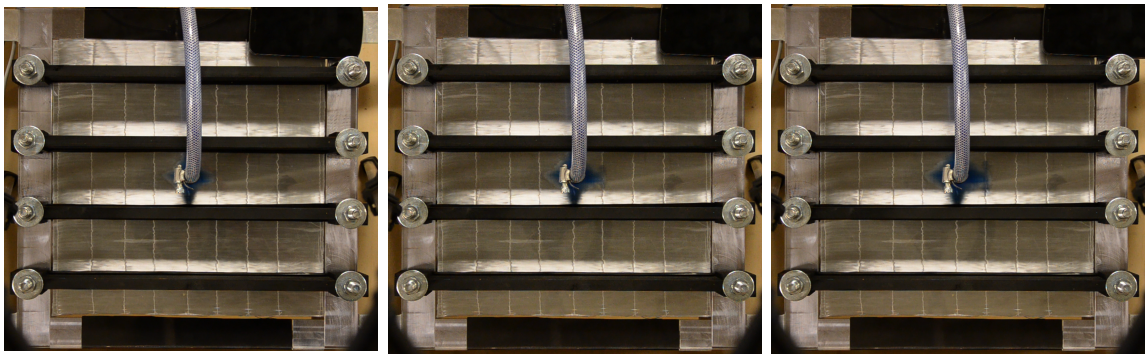

(a) 16:13:367 (b) 22:23:971 (c) 23:23:971

Figure 5.33: Filling pattern, Trial 09

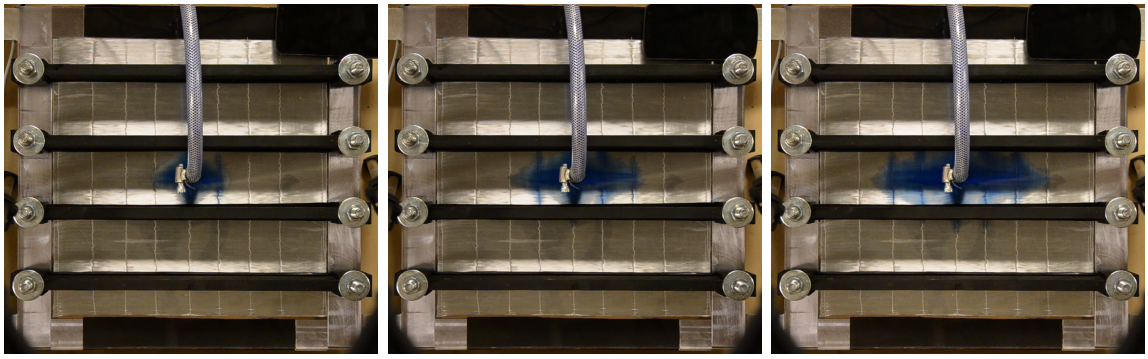

(a) 24:23:971 (b) 25:23:971 (c) 26:23:971

Figure 5.34: Filling pattern, Trial 09

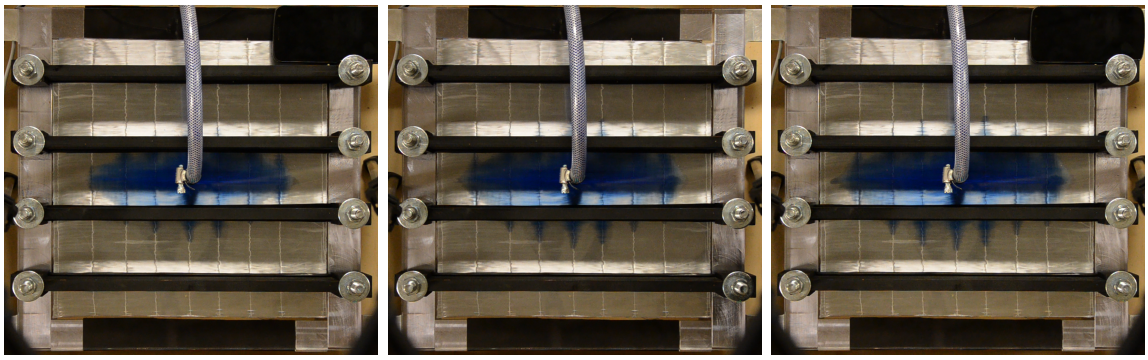

(a) 27:23:971 (b) 28:23:971 (c) 28:49:971

Figure 5.35: Filling pattern, Trial 09

Camera directed toward polycarbonate plate without injection port



(a) 00:00:000 (b) 02:42:934 (c) 03:42:934

Figure 5.36: Filling pattern, Trial 09

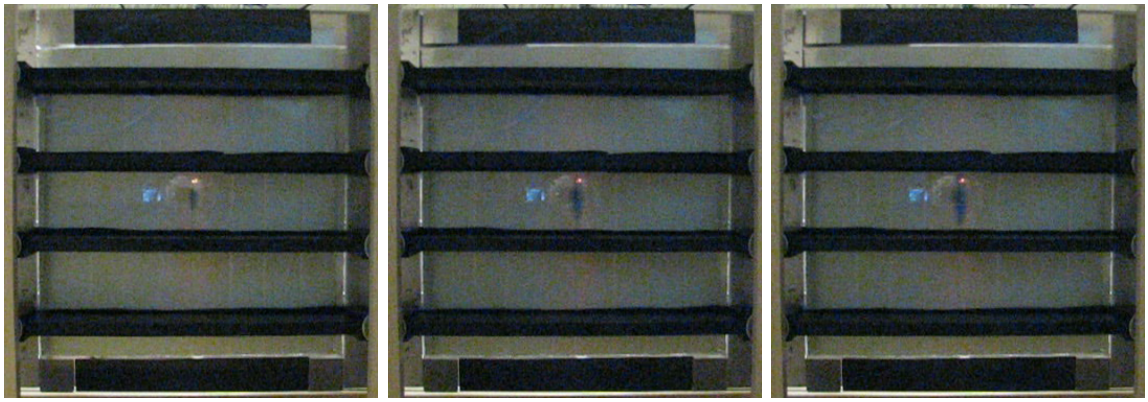

(a) 07:01:548 (b) 11:01:548 (c) 13:01:548

Figure 5.37: Filling pattern, Trial 09

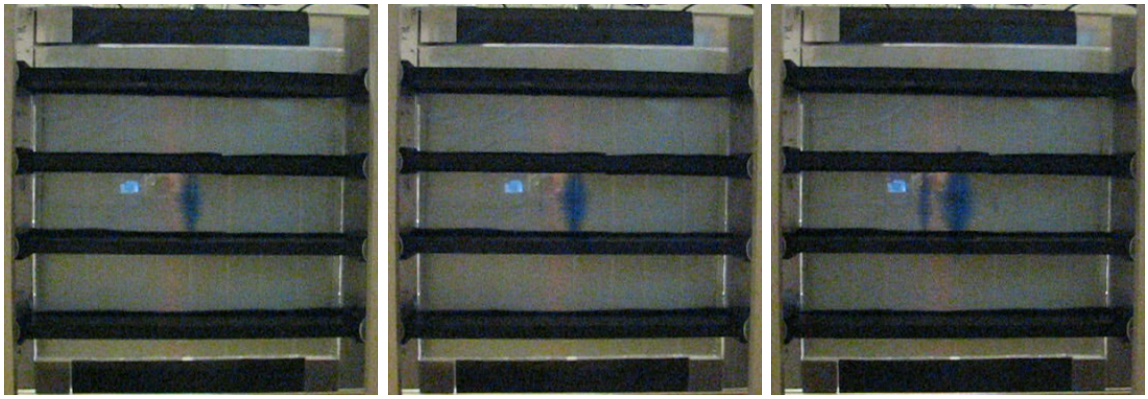

(a) 18:56:291 (b) 20:56:291 (c) 21:56:291

Figure 5.38: Filling pattern, Trial 09

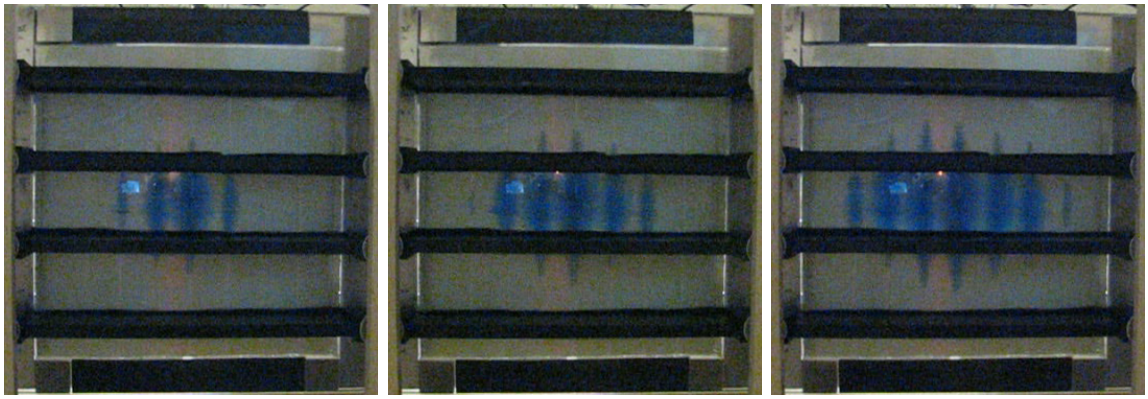

(a) 22:56:291 (b) 23:56:291 (c) 24:56:357

Figure 5.39: Filling pattern, Trial 09

Trial 10

Camera directed toward polycarbonate plate with injection port

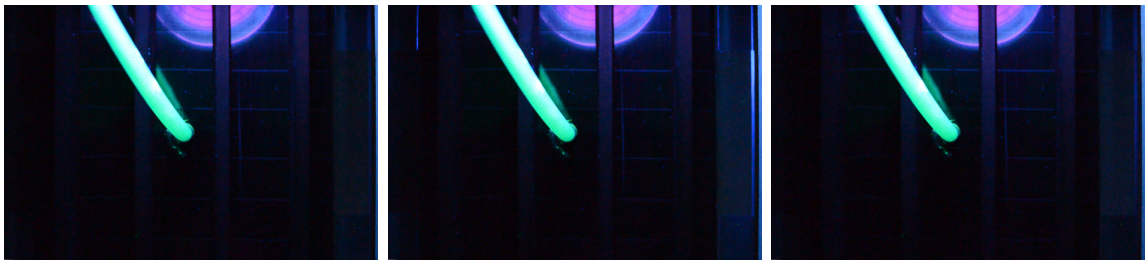

(a) 07:32:530 (b) 08:40:643 (c) 09:33:273

Figure 5.40: Filling pattern, Trial 10

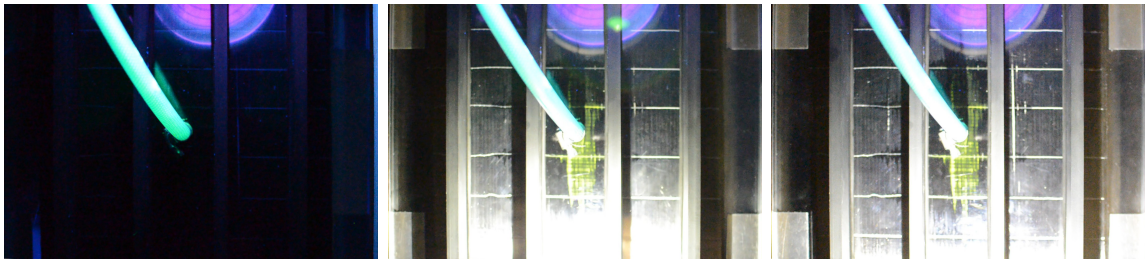

(a) 10:39:854 (b) 11:37:428 (c) 11:57:129

Figure 5.41: Filling pattern, Trial 10

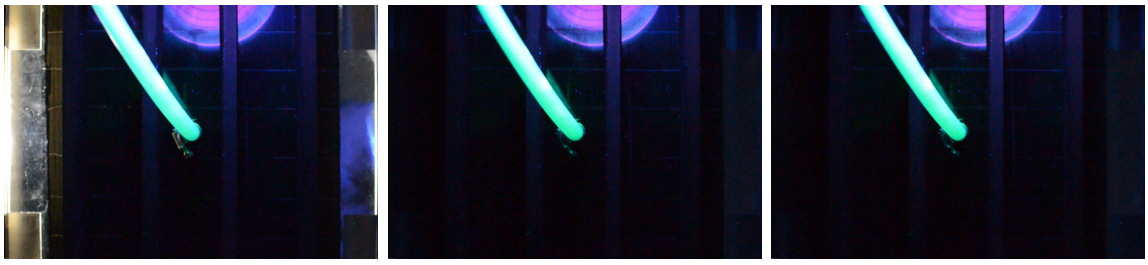

(a) 13:17:314 (b) 14:11:361 (c) 14:51:893

Figure 5.42: Filling pattern, Trial 10

Appendix B

Inlet gauge pressure

Trial 01

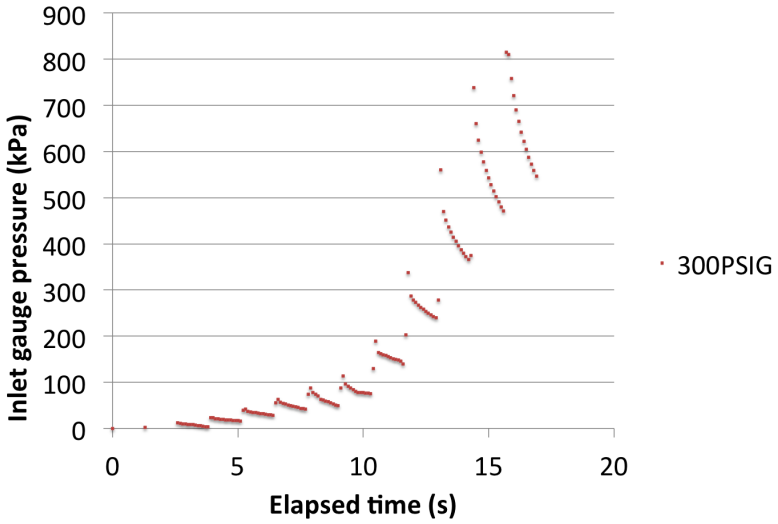

Figure 5.43: Inlet gauge pressure as a function of elapsed time, Trial 01

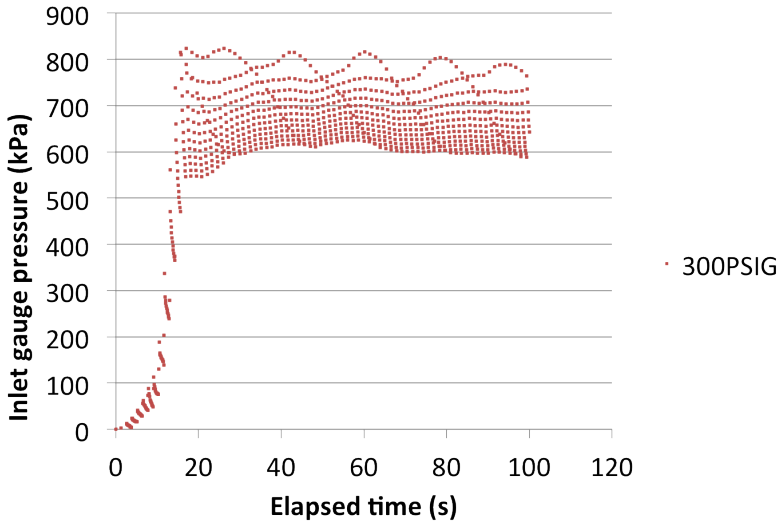

Figure 5.44: Inlet gauge pressure as a function of extended elapsed time, Trial 01

Trial 02

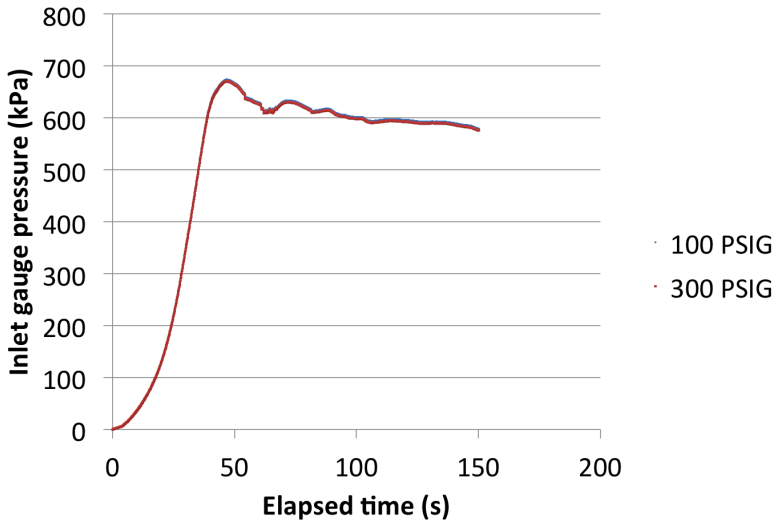

Figure 5.45: Inlet gauge pressure as a function of elapsed time, Trial 02

Trial 03

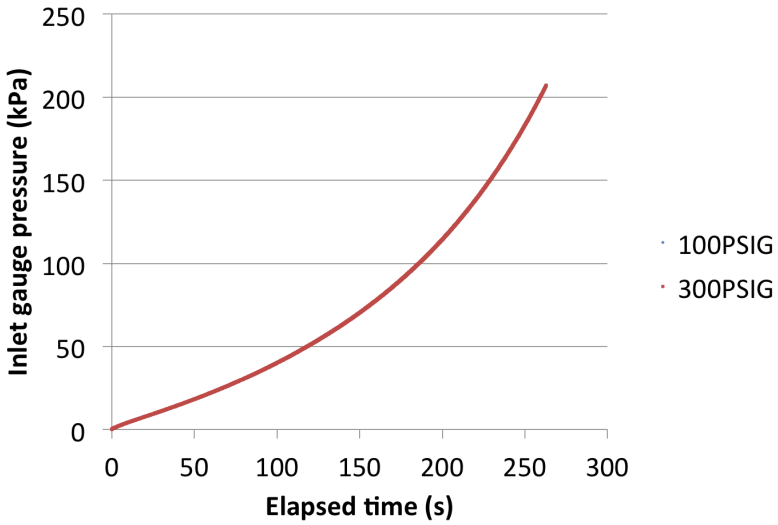

Figure 5.46: Inlet gauge pressure as a function of elapsed time, Trial 03

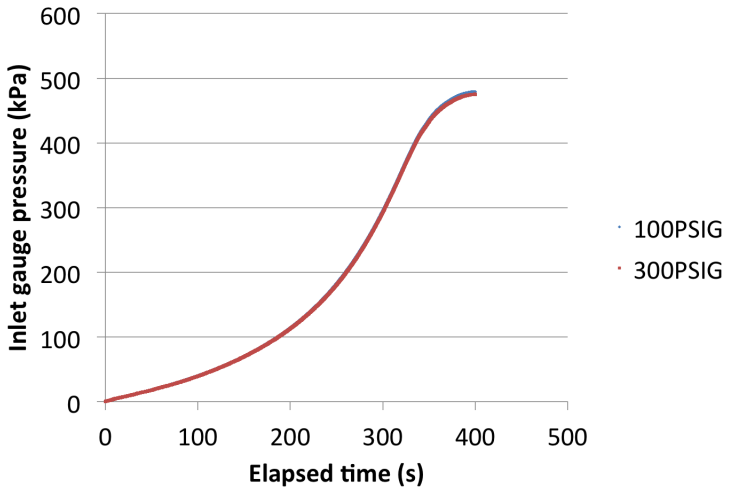

Figure 5.47: Inlet gauge pressure as a function of extended elapsed time, Trial 03

Trial 04

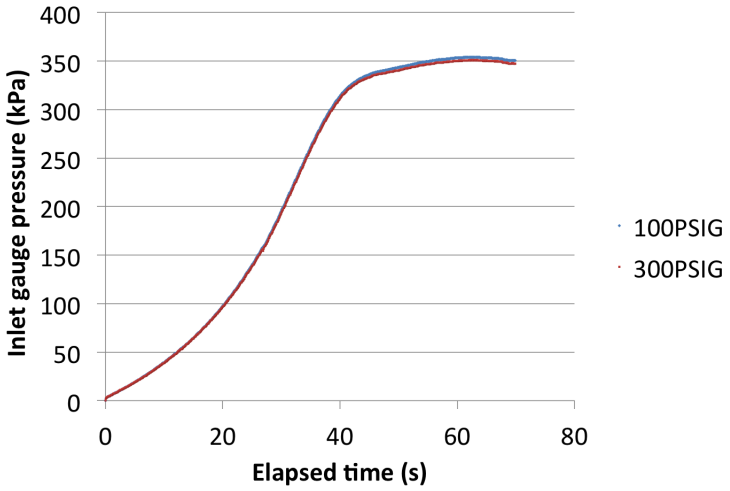

Figure 5.48: Inlet gauge pressure as a function of elapsed time, Trial 04

Trial 05

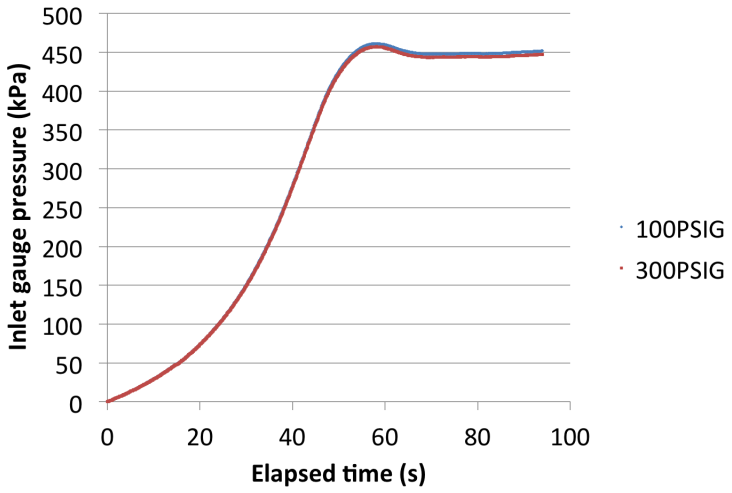

Figure 5.49: Inlet gauge pressure as a function of elapsed time, Trial 05

Trial 06

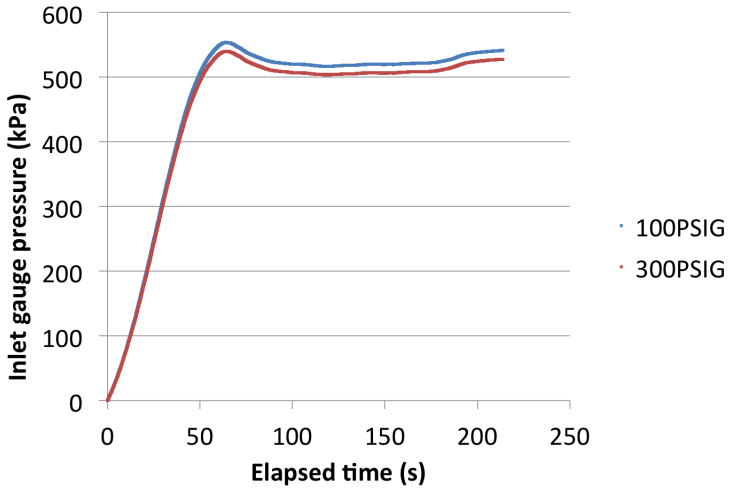

Figure 5.50: Inlet gauge pressure as a function of elapsed time, Trial 06

Trial 07

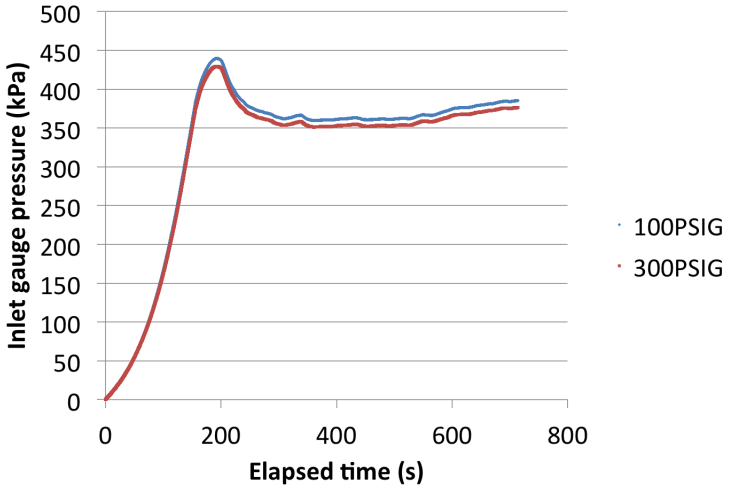

Figure 5.51: Inlet gauge pressure as a function of elapsed time, Trial 07

Trial 08

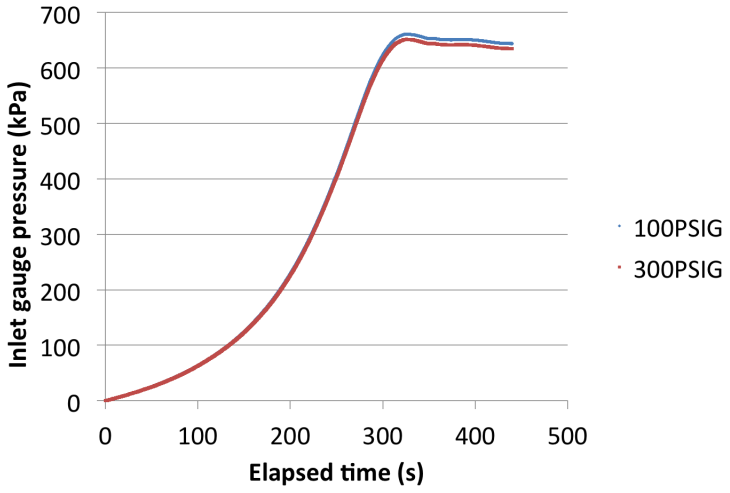

Figure 5.52: Inlet gauge pressure as a function of elapsed time, Trial 08

Trial 09

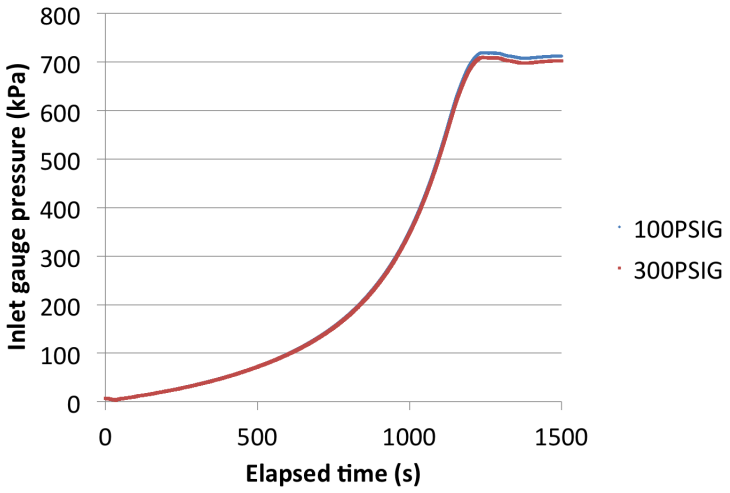

Figure 5.53: Inlet gauge pressure as a function of elapsed time, Trial 09

Trial 10

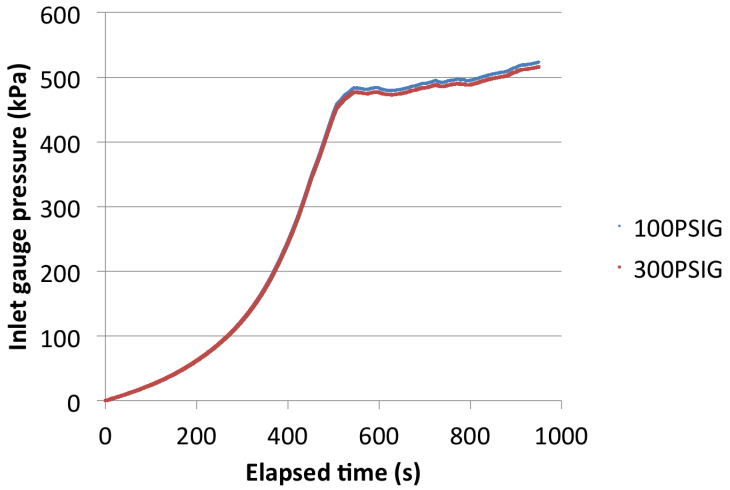

Figure 5.54: Inlet gauge pressure as a function of elapsed time, Trial 10

Appendix C

Compaction curves

Trial 05

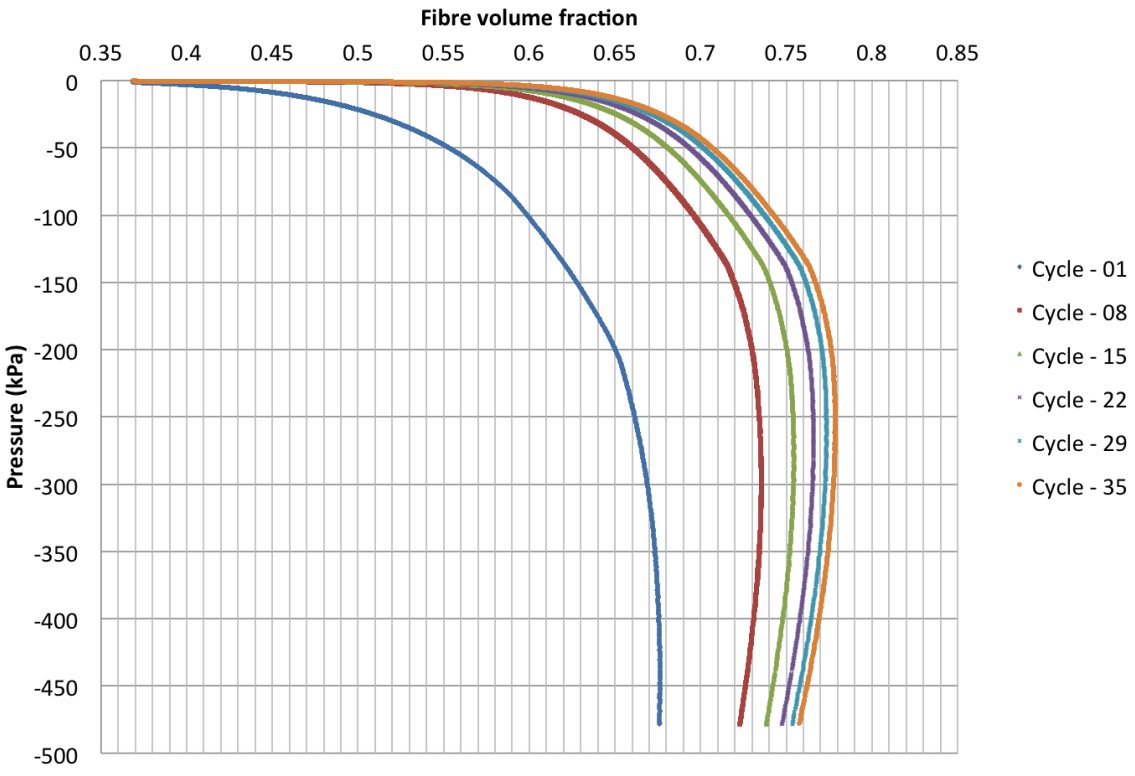

Figure 5.55: Fibre volume fraction as a function of pressure, Trial 05

Trial 06

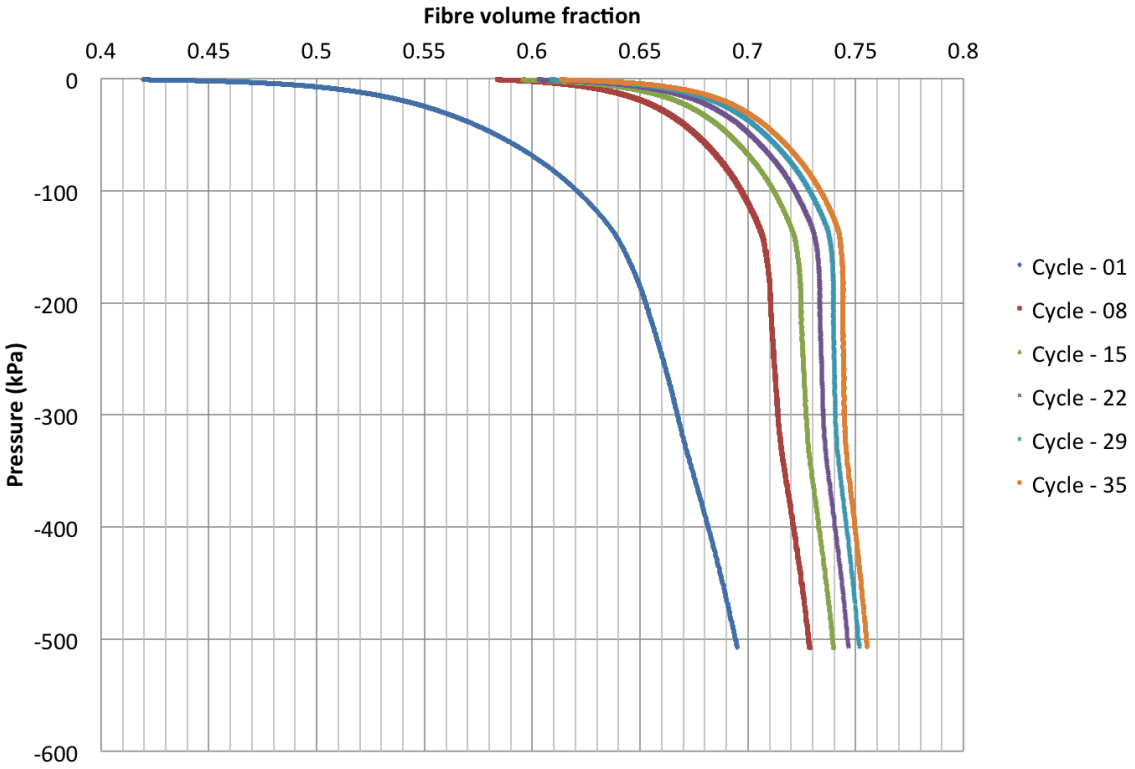

Figure 5.56: Fibre volume fraction as a function of pressure, Trial 06

Trial 07

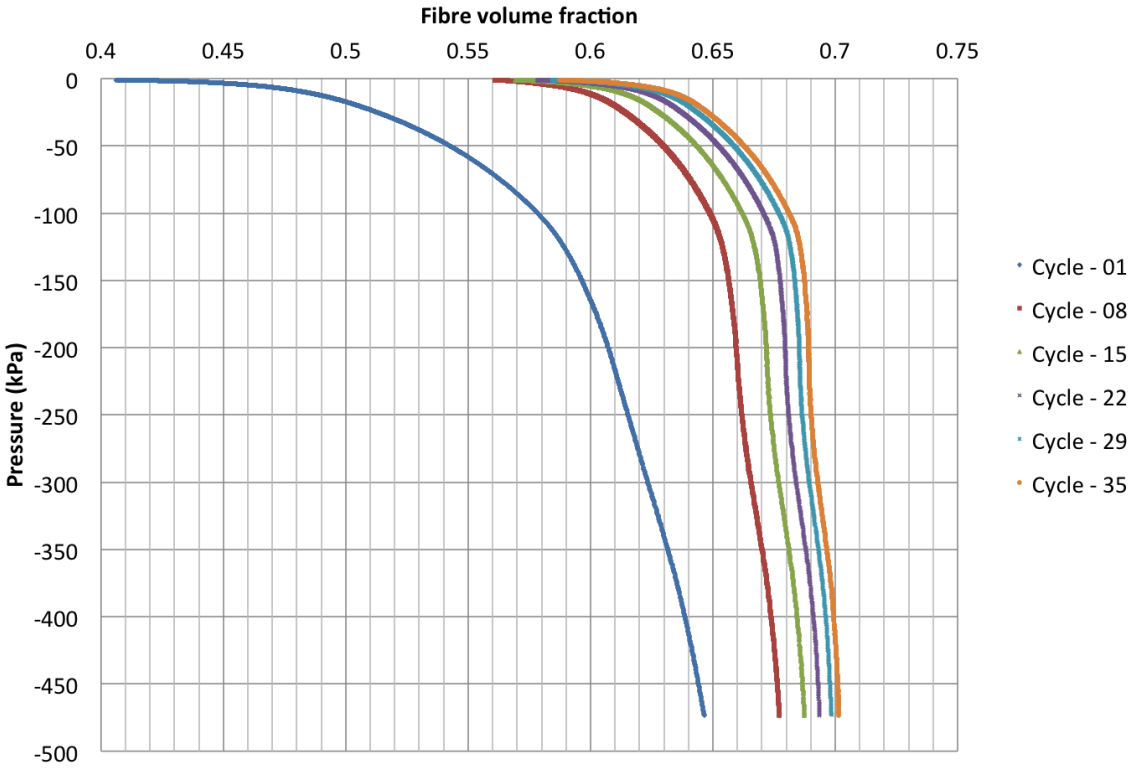

Figure 5.57: Fibre volume fraction as a function of pressure, Trial 07

Trial 08

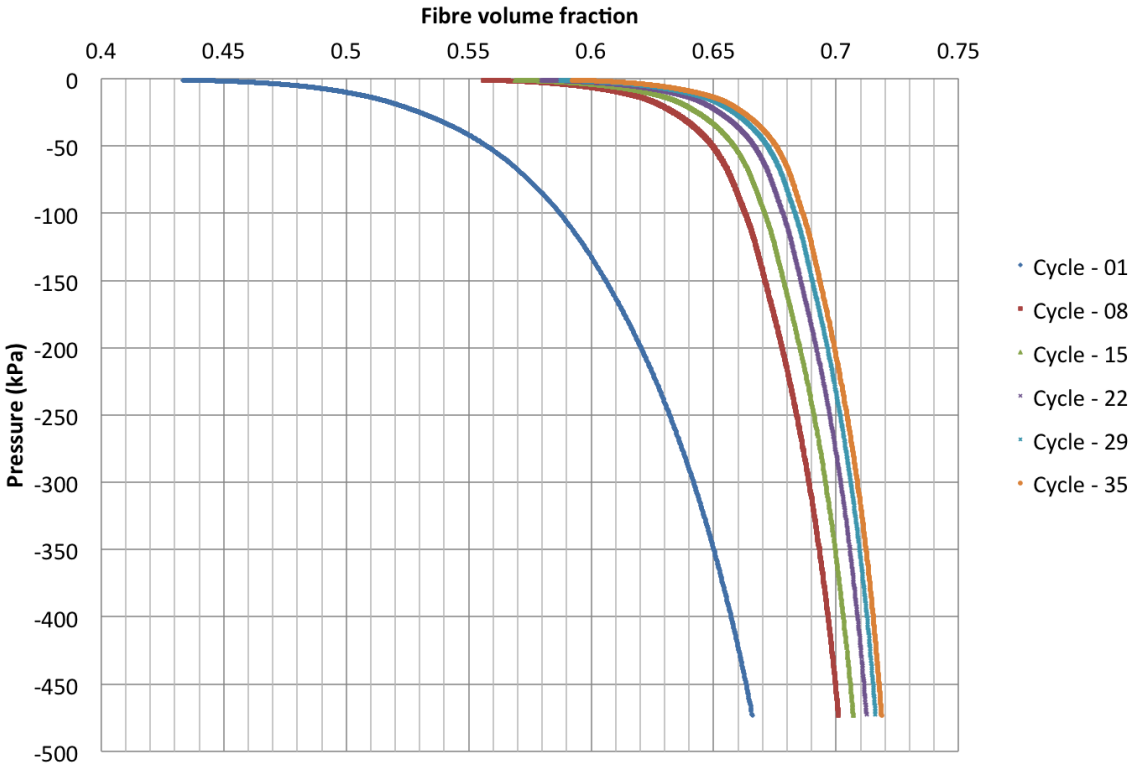

Figure 5.58: Fibre volume fraction as a function of pressure, Trial 08

Trial 09

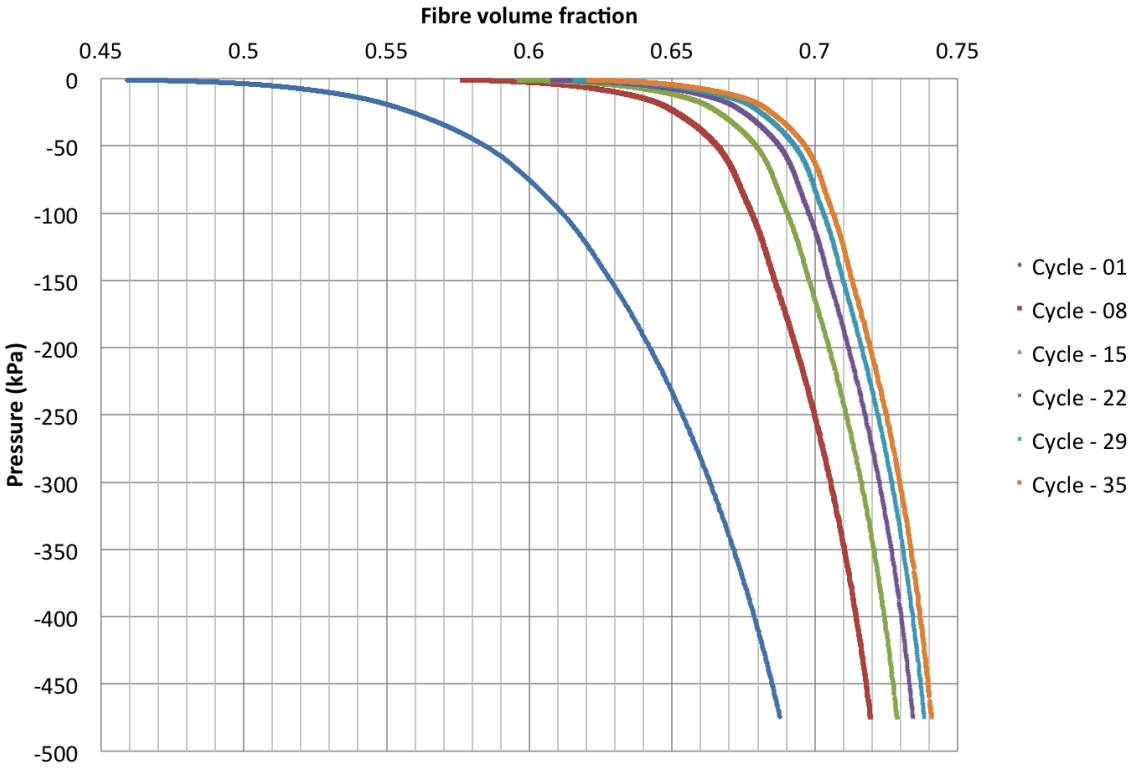

Figure 5.59: Fibre volume fraction as a function of pressure, Trial 09

Appendix D

Equations

Chan *et al.*

Equations developed and applied by Chan *et al.* for constant flow rate into porous media.

Conservation of mass:

$$t = \frac{\pi \left(r_f^2 - r_o^2\right) \cdot h \cdot \epsilon}{q} \tag{A.1}$$

Isotropic

Isotropic permeability:

$$K = \frac{q \cdot \mu}{2\pi \cdot h \cdot P_o} \cdot ln\left(\frac{r_f}{r_o}\right) \tag{A.2}$$

Orthotropic

Equation for an orthotropic fabric:

$$K_x \frac{\partial^2 P}{\partial x^2} + K_y \frac{\partial^2 P}{\partial y^2} = 0 \tag{A.3}$$

Laplace equation in an equivalent isotropic system:

$$\frac{\partial^2 P_e}{\partial x_e^2} + \frac{\partial^2 P_e}{\partial y_e^2} \tag{A.4}$$

Radius of the flow front in an equivalent isotropic system:

$$r_{xe} = \sqrt{m_1} \cdot r_x \tag{A.5}$$

where

$$m_1 = \frac{\partial r_y}{\partial r_x} \tag{A.6}$$

Permeability in an equivalent isotropic system:

$$K_e = \frac{q \cdot \mu}{2\pi \cdot h \cdot m_2} \tag{A.7}$$

where

$$m_2 = \frac{\partial P_o}{\partial \log\left(r_{xe}\right)} \tag{A.8}$$

Orthotropic permeability in the principle directions derived from an equivalent isotropic system:

$$K_x = \frac{K_e}{m_1} \tag{A.9}$$

$$K_y = K_e \cdot m_1 \tag{A.10}$$

General orthotropic

General orthotropic permeability based on known angle between principle axis and laboratory axis:

$$K_{xx} = \frac{(K_x + K_y)}{2} + \frac{(K_x - K_y)}{2}\cos\left(2\theta\right) \tag{A.11}$$

$$K_{xy} = K_{yx} = \frac{(K_x - K_y)}{2}\sin\left(2\theta\right) \tag{A.12}$$

$$K_{yy} = \frac{(K_x + K_y)}{2} - \frac{(K_x - K_y)}{2}\cos\left(2\theta\right) \tag{A.13}$$